

Centrifugal separation for cleaning well gas streams : from concept to prototype

Citation for published version (APA):

Wissen, van, R. J. E. (2006). *Centrifugal separation for cleaning well gas streams : from concept to prototype*. [Phd Thesis 1 (Research TU/e / Graduation TU/e), Mechanical Engineering]. Technische Universiteit Eindhoven. <https://doi.org/10.6100/IR614387>

DOI:

[10.6100/IR614387](https://doi.org/10.6100/IR614387)

Document status and date:

Published: 01/01/2006

Document Version:

Publisher's PDF, also known as Version of Record (includes final page, issue and volume numbers)

Please check the document version of this publication:

- A submitted manuscript is the version of the article upon submission and before peer-review. There can be important differences between the submitted version and the official published version of record. People interested in the research are advised to contact the author for the final version of the publication, or visit the DOI to the publisher's website.
- The final author version and the galley proof are versions of the publication after peer review.
- The final published version features the final layout of the paper including the volume, issue and page numbers.

[Link to publication](#)

General rights

Copyright and moral rights for the publications made accessible in the public portal are retained by the authors and/or other copyright owners and it is a condition of accessing publications that users recognise and abide by the legal requirements associated with these rights.

- Users may download and print one copy of any publication from the public portal for the purpose of private study or research.
- You may not further distribute the material or use it for any profit-making activity or commercial gain
- You may freely distribute the URL identifying the publication in the public portal.

If the publication is distributed under the terms of Article 25fa of the Dutch Copyright Act, indicated by the "Taverne" license above, please follow below link for the End User Agreement:

www.tue.nl/taverne

Take down policy

If you believe that this document breaches copyright please contact us at:

openaccess@tue.nl

providing details and we will investigate your claim.

Centrifugal separation for cleaning well gas streams:
from concept to prototype

PROEFSCHRIFT

ter verkrijging van de graad van doctor aan de
Technische Universiteit Eindhoven, op gezag van de
Rector Magnificus, prof.dr.ir. C.J. van Duijn, voor een
commissie aangewezen door het College voor
Promoties in het openbaar te verdedigen
op maandag 4 december 2006 om 16.00 uur

door

Ralph Joseph Elisabeth van Wissen

geboren te Heerlen

Dit proefschrift is goedgekeurd door de promotoren:

prof.dr.ir. J.J.H. Brouwers

en

prof.dr. M. Golombok

Copyright © 2006 by R.J.E. van Wissen

All rights reserved. No part of this publication may be reproduced, stored in a retrieval system, or transmitted, in any form, or by any means, electronic, mechanical, photocopying, recording, or otherwise, without the prior permission of the author.

Cover design: Oranje Vormgevers Eindhoven (www.oranjevormgevers.nl).

Printed by the Eindhoven University Press.

A catalogue record is available from the Library Eindhoven University of Technology

ISBN-10: 90-386-2958-3

ISBN-13: 978-90-386-2958-2

ACKNOWLEDGEMENTS

The following organisations are acknowledged for their contribution:

Shell International Exploration & Production for funding this research.

Romico Hold for providing know-how and information on the rotational particle separator and related processes.

Contents

Centrifugal separation for cleaning well gas streams: from concept to prototype	1
Nomenclature	3
1 Introduction	7
1.1 Background	7
1.2 Goal and outline	8
2 Concept development	9
2.1 Separation of carbon dioxide and methane in continuous countercurrent gas centrifuges	9
2.1.1 Introduction	9
2.1.2 Batch Centrifuge	10
2.1.3 Continuous Centrifuge	14
2.1.4 Results	22
2.1.5 Conclusions	25
2.2 Gas centrifugation with wall condensation	27
2.2.1 Introduction	27
2.2.2 Theory and Model	27
2.2.3 Results and Discussion	30
2.3 Condensed Contaminant Centrifugal Separation (C3-sep)	33
2.3.1 Introduction	33
2.3.2 Thermodynamics	33
2.3.3 Separation	36
2.3.4 Conclusion	38
3 Thermodynamic and phase change considerations	41
3.1 Introduction	41
3.2 Equilibrium separation for methane enrichment	42
3.3 Equilibrium separation for carbon dioxide enrichment	50
3.4 The influence of the presence of H ₂ S on equilibrium separation	53
3.5 Droplet formation and growth	56
3.5.1 Thermodynamic conditions	57

3.5.2	Homogeneous nucleation	58
3.5.3	Heterogeneous condensation	60
3.5.4	Monodisperse coagulation	64
4	In-line centrifugal separation of dispersed phases	69
4.1	Introduction	69
4.2	Centrifugal Separations	70
4.2.1	Particle kinematics	70
4.2.2	Swirl energy	72
4.3	Axial Cyclone	74
4.3.1	Geometry	74
4.3.2	Swirl Energy	75
4.3.3	Parameter re-expression	75
4.4	Rotational Particle Separator	76
4.4.1	Geometry	76
4.4.2	Swirl energy	78
4.4.3	Channel geometry	80
4.5	Discussion	81
4.6	Conclusions	84
5	The development of a 60 nm³/h C3-sep prototype	87
5.1	Loop design	87
5.1.1	Flow sheet	88
5.1.2	Compressor and sizing	89
5.1.3	Expansion	90
5.1.4	Heat exchangers	90
5.1.5	Induction loop	92
5.1.6	Liquid collection and storage vessel	92
5.2	Separator Design	95
5.2.1	Introduction	95
5.2.2	Design criteria	95
5.2.3	Filter design	98
5.2.4	Geometric design	102
5.2.5	Mechanical drive	104
5.2.6	Final design	108
6	Discussion	111
6.1	Concept development	111
6.2	Optimal operation	112
	Bibliography	115
A	Formulas for equipment dimensions	119
A.1	Cyclone	119
A.2	RPS	119

B Construction drawings of the 60 nm³/h RPS prototype	121
B.1 Part drawings	121
B.2 Assembly drawings	130
Dankwoord	137
Curriculum Vitae	139

Centrifugal separation for cleaning well gas streams: from concept to prototype

More than 16 % of the currently known global gas reserves cannot be produced due to severe CO₂ and/or H₂S contamination: CO₂ > 10% and H₂S > 5%. The traditional technology of amine treatment is not able to economically remove these contaminants. The objective of this thesis is to investigate the possibilities of centrifugal separation to resolve the problem.

Three methods of separation by centrifugation are considered. The first of these is gas/gas separation in a rotating cylinder based on the difference in molecular weight of the gaseous components. The method is directly derived from the gas ultracentrifuge for the enrichment of uranium isotopes. It is shown that by adopting countercurrent flow in the cylinder one can clean up a contaminated natural gas stream in a single production step. However, the production rates of such a gas centrifuge are extremely low. At lower enrichment levels, which also requires multiple separation stages, production rates are higher, but still very low – millions of centrifuges are required to handle a large gas well.

The second method considered is that where the centrifuge is operated at a pressure such that during operation condensation occurs at the wall. It is shown that this leads to a doubling of the production rate, but is still too slow to be economically feasible. So although a contaminated gas stream can be cleaned by gas centrifugation, the required capital investment to manufacture the equipment is simply too high – or the value of the gas too low. Gas centrifugation is a technology that is only interesting for application in the separation of materials with very high economic value, such as in the case of uranium enrichment.

The third method considered is much faster and economically attractive. It consists of two steps: (i) integral cooling of the gas by expansion to a temperature level whereby the contaminants condense to micron-sized droplets. (ii) Removing these droplets using the new technology of the rotating particle separator (RPS). The process is called: Condensed Contaminant Centrifugal Separation (C3-sep)

In order to prove that C3-sep works, a prototype is designed and built for cleaning a natural gas stream containing 50 mole% CO₂ at a flow rate of 60 nm³/h. The

thermodynamics of this prototype and large scale C3-sep application are evaluated for broad range of CH_4/CO_2 gas mixture compositions. Also, the necessity of using the RPS as separator in C3-sep instead of the in the oil and gas industry more common cyclone is demonstrated.

From the thermodynamic evaluation we learn that C3-sep is a bulk separation method. Purification is impossible with this technology, but the enrichment achieved with a single C3-sep system is very large: it is possible to enrich a 50/50 CH_4/CO_2 gas stream to a 78/22 product stream. Also, the flow rates of full scale production are not a problem for implementation of C3-sep. So although it will not be able to fully replace the existing technology, it can be used to access gas fields that are currently too contaminated for production. It can remove the bulk of the contaminants in these fields in a very energy and thus cost efficient way.

High enrichment of CH_4/CO_2 mixtures requires a final separation step where low temperatures occur, resulting in solid CO_2 formation near the walls of the RPS. Removing such particles is technically more difficult than contaminants in liquid form. If H_2S is also present in the gas mixture, lower temperatures and thus higher enrichments are possible without the formation of solids. In that case, enrichment in liquid form is possible up to ratios of 95 % CH_4 in the product stream. This is high enough to further purify the gas stream with conventional technology. Half of the contaminated fields known today contain large amounts of H_2S ; for initial implementation of C3-sep it may be more advantageous to concentrate on these fields.

Nomenclature

A	Centrifuge instrument parameter	$1/\text{m}^2$
A_0	Dimensionless centrifuge instrument parameter	-
C_c	Cunningham correction factor	-
C_m	Torque coefficient	-
D	Diffusion coefficient	m^2/s
D_0	Diffusion coefficient at $t = 0$	m^2/s
d_c	RPS channel height	m
d_p	Particle or droplet diameter	m
D_p	Particle diffusion coefficient	m^2/s
d_p^*	Critical cluster diameter	m
\dot{E}	Energy loss rate	kJ/s
f	Friction coefficient	-
F	Feed flow rate	kmol/s
F_0	Feed flow / Recirculating flow ratio	-
f_i	Dimensionless feed-product-waste mole flux profile	-
G	Momentum loss	Nm
I	Droplet current	$\text{nuclei}/(\text{m}^3\text{s})$
K	Coagulation coefficient	m^3/s
k^*	Number of molecules in a critical cluster	-
L	Centrifuge length	m
L	Separator length	m
l_0	Centrifuge length	m
M	Molar weight	kg/kmol
\dot{m}	Mass transfer rate	kmol/s
m_i	Molecular mass	kg
N	Number density of nuclei/droplets	m^{-3}
n_i	Molecular density	$\text{molecules}/\text{m}^3$
n_{i0}	Molecular density at $t = 0$	$\text{molecules}/\text{m}^3$
p	Pressure	Pa
P	Product flow rate	kmol/s
p_0	Pressure at $r = 0$	Pa
p_d	Dewpoint pressure	Pa
p_{in}	Turbine inlet pressure	bar
p_{sat}	Saturation pressure	Pa

p_{wall}	Pressure at wall	Pa
Q	Volume flow rate	m^3/s
Q_c	Cleaned-up (product) flow rate	kmol/s
Q_f	Feed flow rate	kmol/s
Q_w	Liquid waste flow rate	kmol/s
r	Radial coordinate	m
r	Recovery of CH_4 in cleaned up gas stream	-
R	Universal gas constant	J/kmol/K
R	Wall radius	m
R	Separator radius	m
r^*	Dimensionless radial coordinate	-
r_0	Centrifuge radius	m
r_{CO_2}	Recovery of CO_2 in liquid stream	-
r_d	Droplet radius	m
R_d	Maximum droplet radius	m
Re	Reynolds number	-
R_i	Axle radius	m
R_{id}	Inner RPS filter diameter	m
R_{od}	Outer RPS filter diameter	m
R_w	Separator radius	m
s_g	Radial spacing between RPS filter and housing	m
S	Separation factor	-
S	Supersaturation ratio	-
T	Temperature	K
Ta	Taylor number	-
T_F	Load momentum	Nm
T_{in}	Turbine inlet temperature	$^{\circ}C$
T_M	Motor torque	Nm
t	Time	s
u	Radial mixture velocity	m/s
v_0	Peripheral velocity	m/s
v_{ax}	Axial velocity	m/s
v_i	Gas mixture velocity in direction i	m/s
v_m	Molecular volume	m^3
v_r	Radial velocity	m/s
v_t	Tangential velocity	m/s
v_{t0}	Initial tangential velocity	m/s
w	Axial mixture velocity	m/s
W	Waste flow rate	kmol/s
x	Mole fraction CH_4	-
x_{∞}	Mole fraction of condensible gas in bulk	-
x_c	Mole fraction CH_4 in cleaned-up gas stream	-
x_d	Mole fraction CO_2 at dewpoint	-
x_f	Mole fraction CH_4 in feed stream	-
x_s	Mole fraction of condensible gas at saturation pressure	-

x_w	Mole fraction CH ₄ in liquid waste stream	-
y	Dimensionless droplet radius	-
y_c	Mole fraction CO ₂ in cleaned-up gas stream	-
y_f	Mole fraction CO ₂ in feed stream	-
y_w	Mole fraction CO ₂ in liquid waste stream	-
z	Axial coordinate	m
z^*	Dimensionless axial coordinate	-
z_F^*	Dimensionless axial coordinate of feed point	-
α	Aspect ratio of the centrifuge	-
β	Normalisation factor for counter-current flow	-
β	Empirical factor for velocity decay	-
δ	Inner to outer RPS filter diameter ratio	-
δU	Separative power	kmol
ϵ	Specific energy consumption	kJ/kg
η	Dynamic viscosity	Pa s
θ	Tangential coordinate	rad
Θ	Product/feed ratio	-
λ	Boundary layer thickness parameter	-
λ	Mean free path of the carrier gas	m
λ_F	Product/waste transition layer thickness parameter	-
μ	Dynamic viscosity	Pa s
ξ	Normalisation factor for feed-product-waste flow	-
ρ	Gas mixture molar density	kmol/m ³
ρ_∞	Concentration of condensible gas	kmol/m ³
$\rho_{\infty 0}$	Initial concentration of condensible gas	kmol/m ³
ρ_d	Droplet molar density	kmol/m ³
ρ_f	Carrier fluid mass density	kg/m ³
ρ_p	Particle mass density	kg/m ³
ρ_{vapour}	Total molar vapour density	kmol/m ³
$\rho_{vapour 0}$	Initial total molar vapour density	kmol/m ³
$(\rho v_i)^*$	Dimensionless counter-current mole flux profile	-
$(\rho v_i)^{*0}$	Dimensionless mole flux profile in direction i	-
σ	Surface tension	N/m
τ	Residence time	s
τ_{90}	Time to reach 90 % of steady-state enrichment	s
τ_{diff}	Dimensionless time	-
ϕ^*	Dimensionless recirculating flow	-
ϕ_{mc}	Counter-current flow rate	kmol/s
Ψ	Dimensionless stream function	-
Ω	Angular velocity	rad/s

Chapter 1

Introduction

1.1 Background

Recent price rises in natural gas are driven by oil and gas demand. Traditionally oil has been the main energy source, but with rising oil prices, relatively new technologies that exploit natural gas, such as Liquefied Natural Gas (LNG), become economically more attractive.

From a quick evaluation of public gas reserves data [2], it follows that in 2003 there was approximately $2.1 \cdot 10^{10}$ MMscf ($= 10^6$ standard cubic feet) or $4.3 \cdot 10^{14}$ kg of methane present in the known natural gas reserves. Most of these reserves are already being produced, but there is a substantial part that cannot be produced by existing technology. These gas fields contain large amounts of contaminating gases, mainly CO_2 and also H_2S [25]. By large amounts we mean $>10\%$ CO_2 and $>5\%$ H_2S . At lower levels of contamination, amine treatment is currently used for removing CO_2 and H_2S from well gas [5]. This process uses large amounts of energy even for low contaminations; the reheater that is required to recycle the absorption fluid is the main cost. A second disadvantage is that the waste gases are produced at atmospheric pressure, which results in high compression costs for reinjection. Due to these two disadvantages it is currently too expensive to produce from gas fields that contain more than ca. 10 % CO_2 and 5 % H_2S .

Approximately 16 % or $3.5 \cdot 10^9$ MMscf of the available methane in gas reserves is located in fields that contain more than 10 % CO_2 or 5 % H_2S . This adds up to 369 times the annual natural gas production in 2005 of the three largest oil and gas companies – ExxonMobil, BP, and Royal Dutch/Shell Group [3, 1, 4]. So there are very strong economic reasons to search for new technologies which enable the production of these contaminated gas fields.

Apart from the standard technology, amine treatment, several other technologies have been or are still being developed to tackle this problem. These are [29, 32]:

- absorption in organic solutions, mainly developed for removing CO_2 from exhaust gases,
- zeolite absorption, currently used for ppm level CO_2 removal, and

- membranes, which is a technology that is difficult to scale up.

The technologies in this list are like amine treatment not suitable to handle the contaminated gas reserves, because they are not able to either remove high levels of contaminants or handle the required the flow rates for natural gas production (> 100 MMscf/d). Selective gas hydrate formation seems promising but is still in an early stage of development.

A technology that has not yet been considered for contaminant removal is that of centrifugal separation. A centrifugal separator utilises the centrifugal force to separate matter on the basis of their weight difference. This can either be a difference in molecular weight, as is done in the high-G gas centrifuges, or a difference in density of multiple non-mixing phases, such as in an oil-water separator or in a dust collecting cyclone.

1.2 Goal and outline

The aim of this study is to develop a centrifugal separator that is able to remove CO_2 and H_2S from highly contaminated natural gas streams and is able to economically handle a flow of > 100 MMscf/d (> 23 kg/s).

In section 2.1, we will first evaluate the applicability of classic gas/gas centrifugation to clean the contaminated gas streams. It will be shown that this technology is too slow, resulting in low production rates or large equipment size and thus high investment costs. To speed up this process wall condensation can be applied, resulting in a condensing centrifuge, which is theoretically evaluated in section 2.2. Although this is a faster process, it is still not fast enough to meet the production rate requirements. The drawback of these gas centrifugation methods is that they are limited by gaseous diffusion, which is a very slow process.

A much faster process is that of instantaneous condensation of the contaminants by integral cooling of the gas mixture. The contaminants form fine mist particles which can be remove by the new technology of the rotational particle separator (RPS). The concept is called Condensed Contaminant Centrifugal Separation (C3-sep), and is presented in section 2.3.1.

Chapter 3 focusses on the thermodynamics and droplet formation process of C3-sep, which determine the operating conditions of the process and also set the separation performance requirements of the rotational particle separator.

In chapter 4 two competing in-line centrifugal separators, the axial cyclone and the rotational particle separator are evaluated and compared on the basis of objective parameters. These parameters are volumetric throughput, residence time and specific energy consumption. On the basis of this study the rotational particle separator is selected as the separator of the mist droplets in the C3-sep process.

In order to determine the potential of C3-sep outside the theoretical world, we want to experimentally prove that it works. Therefore a laboratory prototype is designed, which is outlined in chapter 5.

Chapter 2

Concept development

2.1 Separation of carbon dioxide and methane in continuous countercurrent gas centrifuges*

2.1.1 Introduction

The gas centrifuge is a device which spins a certain amount of gas to a rotational speed greater than 20000 rpm. Due to the large centrifugal field inside the centrifuge, typically 10^5 to 10^6 greater than gravity, the heaviest molecules are pushed to the wall, whereas the lighter molecules concentrate near the centre of the centrifuge. Gas centrifugation is thus a separation method that is based on centrifugal force and molecular weight difference. It is therefore a very suitable method for separating isotopes, since in this case the molar weight difference is a physical difference of the otherwise chemically identical molecules.

Over the years gas centrifugation has been developed to become the leading technology for isotope separation. However, there is currently no commercial application of gas centrifugation other than isotope separation. Now that the traditional technology fails in the area of cleaning highly contaminated well gas, we focus our attention to the complex but successful technology of gas centrifugation and try to discover if it is commercially feasible to apply gas centrifugation on large scale natural gas production.

A limited number of papers have previously examined the application of gas centrifuges to gas separation outside the usual isotope enrichment area of interest [6, 45, 24, 21]. However, there are some other difficulties which prevent direct implementation of gas centrifuge technology. One is the secrecy surrounding centrifuges. Though understandable because centrifuges are commonly used to produce highly enriched uranium, it means that there are few publications by people who have actually worked with them [7, 26, 30, 9, 10, 11]. Literature on the application of the

*Partially reproduced from: van Wissen, R.J.E., Golombok, M., Brouwers, J.J.H. Separation of carbon dioxide and methane in continuous countercurrent gas centrifuges. Chem Eng Sci. 2005; 60(16):4397

gas centrifuge for non-isotopic separation is scarce whereas natural gas separation by membranes and solvent absorption is well established [5, 29, 32]. A second disadvantage of the centrifuge is its high rotational speed which is essential for the process, but also requires very advanced technologies.

In section 2.1.2 we briefly overview the batch centrifuge as a basis from which the more complicated continuous countercurrent model can be developed. Practical operation requires a continuous device however previously developed results and derivations are not fully applicable due to several fundamental differences between isotope separation and CH₄-CO₂ separation which we formulate and develop in section 2.1.3. A similar approach to obtain a simplified differential equation for the countercurrent centrifuge is infeasible because we are dealing with matter with large differential molecular weight in contrast to uranium isotopes where the difference in molecular weight is relatively small. Therefore in order to assess achievable flows and separation in this paper the convection-diffusion equation is solved numerically. The same numerical code is also used to determine the influence of design parameters – the results are described in section 2.1.4.

2.1.2 Batch Centrifuge

A gas centrifuge is basically a rotating hollow cylinder which is filled with a gas mixture. Batch centrifugation is not very interesting for industrial application; however, because of the conceptual simplicity it is very useful for getting a better understanding of the basic working principle and for examining the influence of parameters such as pressure, speed and temperature.

The operating characteristics of the gas-gas batch centrifuge have been extensively reviewed in previous reports along with the modifications we have introduced for the application to natural gas [24]. A brief summary is given here in order to place the process development in a general context. The gas centrifuge is easiest understood by reference to fig. 2.1. A mass of gas with two components of different molecular weight is spun up. A pressure gradient develops nearly instantaneously with a concentration gradient for each component. Diffusion occurs along this concentration gradient until the centrifugal force is balanced.

Large centrifugal forces push the gas to the wall resulting in a pressure gradient which for a steady-state batch centrifuge is described for each component i by [6]:

$$p_i(r) = p_i(0) e^{A_i r^2} \quad (2.1)$$

where p_i is partial pressure of component i (MPa), and r the radial coordinate (m). The coefficient A_i is defined by

$$A_i = \frac{M_i \Omega^2}{2R_g T} \quad (2.2)$$

where M_i is the molecular weight of component i , Ω is the angular velocity, R_g the gas constant and T the temperature. Note that eq. (2.1) assumes ideal gas behaviour. In fact at higher pressures near the rotor periphery, dewpointing will occur and the model we have described would be inadequate for predicting the formation of condensation.

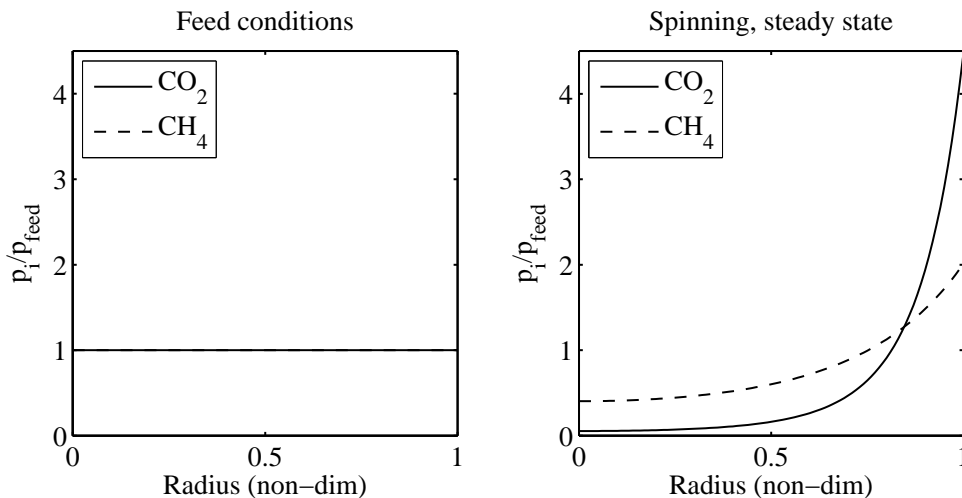


Figure 2.1. Schematic of batch centrifuge showing pressure distribution of two components under feed conditions and following spin-up.

We have previously shown that condensation can be described quantitatively [21] using a statistically based molecular interaction model. Based on these equations, gases with different molecular weights have different partial pressure profiles; therefore in steady-state operation their mole fraction profiles vary with radius. Cohen derived the partial differential equation which describes the time-dependent mole fraction distribution in a gas centrifuge of any type [20]. The simplified equation for a gas mixture consisting of two components denoted with subscripts 1 and 2 is:

$$\rho \frac{\partial x_1}{\partial t} + \rho v_z \frac{\partial x_1}{\partial z} + \rho v_r \frac{\partial x_1}{\partial r} = \frac{\rho D}{r} \frac{\partial}{\partial r} \left(r \frac{\partial x_1}{\partial r} + 2A x_1 (1 - x_1) r^2 \right) + \rho D \frac{\partial^2 x_1}{\partial z^2} \quad (2.3)$$

where D is the diffusion coefficient (m^2/s), ρ the mixture mass density (kmol/m^3), z the axial coordinate (m), t denotes time (s), v_i the gas mixture velocity in direction i (m/s), x_1 the mole fraction of component A where [36]:

$$A = A_2 - A_1. \quad (2.4)$$

Here, the terms on the left hand side represent change of mass transport per unit volume by instationarity and by convection. These changes are balanced by diffusion represented by the r.h.s. The following assumptions were made during the derivation of this equation:

- ρD is a constant
- Temperature is constant throughout the gas, i.e. $T = T_0$.
- Convective velocities of both components are assumed to be the same.

For a better understanding of the influence of the design parameters length and radius and to simplify the numerical modelling the following dimensionless coordinates are introduced: $z^* = z/l_0$ and $r^* = r/r_0$, where l_0 is the centrifuge length (m) and r_0 the centrifuge radius (m). For a batch centrifuge with no internal convection, eq. (2.3) can be simplified to

$$\frac{\rho r_0^2}{D} \frac{\partial x_1}{\partial t} = \frac{1}{r^*} \frac{\partial}{\partial r^*} \left(r^* \frac{\partial x_1}{\partial r^*} + 2Ar_0^2 x_1 (1 - x_1) r^{*2} \right) \quad (2.5)$$

Since there is no axial flow in the batch centrifuge, terms in $\partial/\partial z$ are neglected. Thus the mole fraction is independent of the axial co-ordinate $x_1 \neq x_1(z)$. The right hand side of this equation scales with $A_0 = Ar_0^2 = \Delta M \cdot v_0^2/(2RT)$, which is mainly dependent on the design parameter peripheral velocity, $v_0 = \Omega r_0$. From the left hand side it can be seen that the spin-up time, i.e. the batch time required to reach a certain enrichment, scales with r_0^2/DA_0 ; the number of moles inside the centrifuge, m , scales with $r_0^2 l_0$. Therefore the production rate, $\dot{m} = \int \rho dV/\Delta t$, scales as $\rho D l_0 A_0$. For a given level of enrichment the production per unit time is only a function of centrifuge length and peripheral velocity [20, 36].

Equation (2.5) is solved in order to estimate product flow magnitude and composition of a 50/50 CH_4/CO_2 feed stream. We used Aspen Custom Modeler (ACM) – an equation oriented modelling package. The problem is set up as spatially axisymmetrically discretised along a uniform grid and time integration is performed with a fourth order Runge-Kutta algorithm. Previous work has looked at a batch centrifuge [6, 24]. The current work extends the latter work and is used as a reference case for comparison with the countercurrent calculations. All calculations in this work are performed using an effective static fill pressure of 0.5 MPa and a fluid temperature of 293K. This choice of conditions is influenced by a number of application factors. Reservoir gas pressures are typically on the order of 10-30 MPa but are reduced significantly at the well head typically being throttled to around 7 MPa. Previous gas centrifuge work has been based on low pressures because of the desublimation of UF_6 . The limits for our study are therefore a feed pressure above atmospheric pressure but sufficiently low so that during centrifugation we do not reach dewpointing pressures (above 2.5 MPa). A feed pressure of 0.5 MPa fulfils this requirement. The results reported in this work are almost independent of pressure because the product ρD increases slightly for very high static fill pressures (> 7 MPa) which is academic as condensation will occur at this level anyway. In this study we used the value for the product $\rho D = 2.8 \times 10^{-5}$ kg/ms based on a calculation of known material properties for the gas mixture.

In order to solve eq. (2.5) the following boundary conditions have been applied:

$$\text{at } z^* = 0 \text{ and } z^* = 1, \text{ for } 0 < r^* \leq 1: \quad \frac{\partial x_1}{\partial z^*} = 0,$$

$$\text{at } r^* = 0, \text{ for } 0 \leq z^* \leq 1: \quad \frac{\partial x_1}{\partial r^*} = 0,$$

$$\text{at } r^* = 1, \text{ for } 0 < z^* < 1: \quad \frac{\partial x_1}{\partial r^*} = -2Ar_w^2 x_1 (1 - x_1),$$

which simply state symmetry around the axis and mass conservation at the walls.

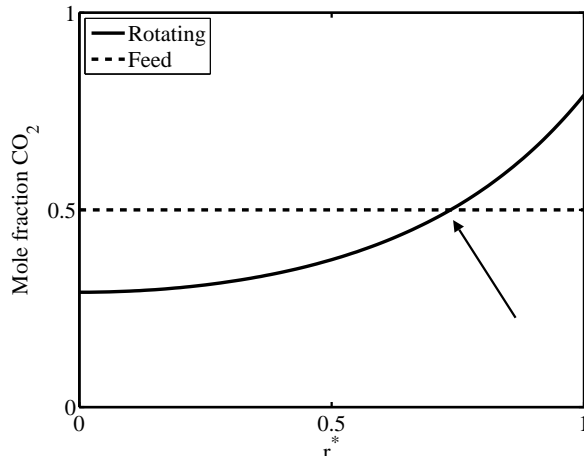


Figure 2.2. Mole fraction of CO_2 as a function of non-dimensionalised radius in a 5 cm radius centrifuge spinning at 70,000 rpm. The arrow indicates the radial crossing point – the point where the imposed equilibrium concentration exceeds that of the feed.

Product flows are calculated by dividing the methane enriched portion in the interior of the centrifuge by τ_{90} - the time required to reach 90 % of the equilibrium steady-state enrichment [24], because reaching steady-state would theoretically take an infinitely long time. The enriched fraction in the interior is everything inside the so-called radial crossing point, defined as the radius at which the composition is equal to the feed composition (fig. 2.2). Bearing in mind the exponential pressure distribution inside the centrifuge (eq. (2.1)) and the fact that the batch centrifuge is a closed system it is easy to see that due to mass conservation the pressure in the center of the centrifuge will be lower and the wall pressure will be higher than the static fill pressure [24]. The time τ_{90} is defined as the time required to get an average enrichment inside the product volume that is 90 % of the steady-state enrichment. The time required for refilling, pressurising and spinning up the centrifuge is neglected in this model. Production scales linearly with length, thus results will be presented per unit length, i.e. for a 1 m. long centrifuge. Fig. 2.3 shows the mole fraction CH_4 and the product and waste flows as a function of peripheral velocity. The graphs are plotted for peripheral velocities up to 1600 m/s; however, with current commercial rotor technology it is not possible to have a higher velocity than 800 m/s. This is mainly due to material limitations [20]. Even at high velocities the production of a 1 m. batch centrifuge is still very limited – on the order of kg/hr – whereas what is required is 100's of ton/hr – corresponding to 100's MMscf/d. The reason for this is that the separation process itself is dominated by diffusion and since diffusion is very slow this results in a low production rate. The only way to augment the separation rate is to use the radial pressure gradient to dewpoint the heavier waste component

as we have previously discussed [21].

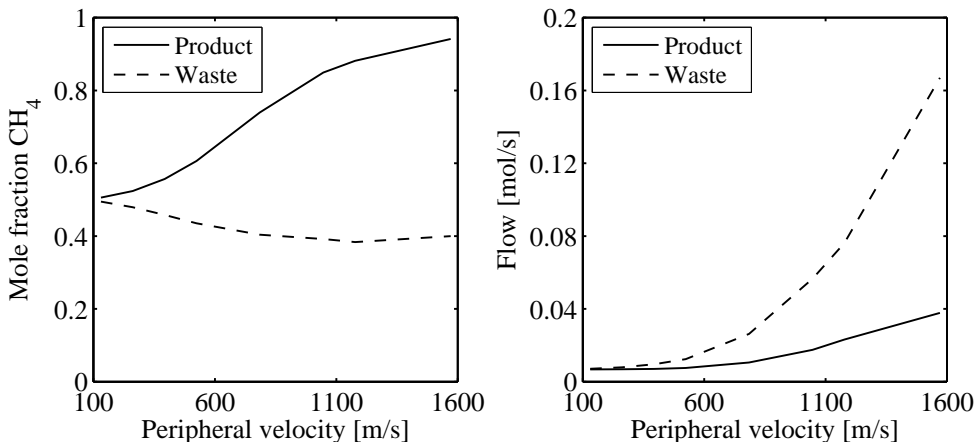


Figure 2.3. Mole fraction CH₄ and flows as a function of peripheral velocity for a 1 m long centrifuge.

2.1.3 Continuous Centrifuge

The batch process can be effectively accelerated by switching to a countercurrent process. Of course any practicable process has to be continuous and these may be divided up into cocurrent and countercurrent configurations [20]. The former is very similar to the batch process where the time co-ordinate is basically replaced by motion along the axial flow dimension. The flow is assumed laminarised by, for example, use of a channelled medium. This has previously been shown to decouple axial and radial turbulence – the radial flow must remain laminar of course so as not to spoil the centrifugal separation process. The countercurrent process is the one of interest because it is the most efficient and will form the emphasis in this section. It is well known from process engineering (and also convective heat transfer) that countercurrent processes with product (i.e. methane) and waste (i.e. contaminant) enriching streams flowing in opposite directions, lead to the maximum radial concentration gradient and thus the most efficient separation mechanics.

Isotopic vs. natural gas centrifugation

The continuous countercurrent mode (as in many applications e.g. heat exchangers) is the spatially most efficient operation. However when applied to the gas centrifuge, and as a result of the complicated coupling of extra terms, the formulation has a number of extra terms compared to the batch equation

$$\rho w \frac{\partial x_1}{\partial z} + \rho u \frac{\partial x_1}{\partial r} = \frac{D\rho}{r} \frac{\partial}{\partial r} \left(r \frac{\partial x_1}{\partial r} \right) + 2(A_2 - A_1)r^2 x_1(1 - x_1) + D\rho \frac{\partial^2 x_1}{\partial z^2} \quad (2.6)$$

where the symbols are as previously defined with the addition of z , the axial direction and w the velocity component in that direction. In a continuous unit there is of course axial flow. In fact the replacement of $\partial/\partial t$ by $w\partial/\partial z$ is not strictly correct because now x_1 is z dependent i.e. $x_1 = x_1(z)$ so a number of terms in the full equation need to be retained. In the original work available in the open literature, a number of mathematical issues in the handling of the equation are addressed [20]. This was necessary to deal with the restricted computing power available at the time. We now show that they are only valid for the heavy isotope separation case, and that they are not appropriate for natural gas processing. For example it was previously assumed that concentration gradients $\partial x_1/\partial r$ and $\partial x_1/\partial z$ are all small – this is not true for the methane/CO₂ centrifuge due to the boundary conditions and the spatial enrichment gradient that is imposed on a single unit. At any rate, advances in computing power mean that the full Eq. (2.6) can be handled – not a subject which appears to have been tackled – in the open literature at any rate.

The analytically based derivation of Cohen used simplifications of a number of parameters. The most important is the separation factor – usually defined by analogy with distillation for the batch case as the ratio of concentrations at the wall($r=R$) divided by that at the centre [35]:

$$S = \frac{x_1(0)/x_2(0)}{x_1(R)/x_2(R)} \quad (2.7)$$

In all previous literature analyses this parameter is assumed to be close to 1. Those comparisons were aimed at deriving the separative power. This assumes that the centrifuge can separate components to provide a given product and waste stream composition – and the separative power gives the corresponding flow rate at which these separations can be achieved. Cohen showed that the separative power has a maximum value of

$$\delta U_{\max} = \frac{Dp}{R_g T} [(A_2 - A_1)R^2]^2 \frac{\pi L}{2} \quad (2.8)$$

where in addition to previously defined symbols, L is the length of the centrifuge. This separative power is a combination of quantity and quality for the flow and achieved separation. It is effectively the separation factor S in eq. (2.7) above, combined with the flow at optimum internal flow conditions. The actual separation that can be achieved is given by

$$\delta U = \varepsilon \delta U_{\max} \quad (2.9)$$

where the factor ε is a function of the geometric configuration used and depends on the process flow and the number of “poles” in the system. i.e. the number of inlet and outlets. For example, a single feed inlet, product outlet and waste outlet constitutes a 3 pole system.

The assumptions used in deriving this term rested on the quantitative simplifications from assuming small concentration gradients as discussed earlier [20]. Crucial to the development of eq. (2.9) is the assumption that the elementary (unit) separation factor defined in eq. (2.7) is only very slightly greater than 1. This is in contrast

where $S \gg 1$. At various points in the derivation for the separation this assumption of “very small” $S-1$ is explicitly stated in order to simplify various sequential element balances in a cascade.

The difference between the molecular weights and the consequences it has for the analysis of the problem is the starting point for our analysis. We can compare the separation factor for isotopes and for natural gas in an experimentally realistic centrifuge. From our own experimental program [23] it is clear that realistic material and mechanical process parameters for a centrifuge are in the range 32000-100000 rpm with rotor radii of 7-9 cm. Currently we can continuously centrifuge at 32000 rpm with $r_0 = 8,9$ cm. The limits are set by the rotor material tensile strength which limits the maximum speed at the periphery of the rotor – and also the sliding speed of the rotating seal. This purchasable technology is already more than a decade old and so we feel justified in using the upper limits of these ranges. Table 2.1 shows the parameters for the experimentally attainable configurations for both UF_6 and CH_4/CO_2 . Notice that the separation factor is only nearly 1 for the lower speed isotope case. Yet this near unitary assumption is the basis for the extensive analysis and subsequent cascade requirements which have been carried out in the literature. i.e. the previously used assumptions for the countercurrent centrifuge are not correct. In our previous work we concentrated on the assumptions made in simplifying the countercurrent centrifuge equation. In a later account of the derivation of the separative power [36], one finds this assumption of near unitary separation factor entering at a number of points into the derivation of the mass transport, resulting separative power and the associated cascade configuration. Our main conclusion is that the assumptions used are thus not valid for the current state of technology and also not for the separation of natural gas components. For this reason we have re-examined the countercurrent centrifuge and rederive the associated equations without any of the simplifying assumptions which were only applicable to isotopes. Many of these simplifying assumptions date from a time when it was not possible to handle the full dynamic equations by numerical models. Although computer simulations have been able to do this for some time now, there has not been any report on addressing these issues – probably mainly because with two exceptions, all work has been concerned with isotopes. To the best of our knowledge no-one has ever pointed out before that this underlying assumption is not valid when it comes to considering lighter molecular weight components such as those found in natural gas.

Since the derivation of unit separative power (eq. (2.8)) seems to rest explicitly at several places on the $S \approx 1$, small product to feed ratios and also small concentration gradient assumptions, which we have demonstrated to not be valid for natural gas, it seems to us worth the effort that the model should at least solve the countercurrent equations for the centrifuge explicitly, rather than simply estimating the separations by using eq. (2.3) which we have now demonstrated to rest on inapplicable premises for the natural gas case.

Countercurrent Model

In order to perform numerical calculations on the countercurrent centrifuge, we non-dimensionalise the velocity field with physical parameters. Let us therefore first out-

Speed (rpm)	Rotor radius (cm)	Separated material	S – separation factor
32000	8,9	$^{235}\text{UF}_6/^{238}\text{UF}_6$	1,06
32000	8,9	CH_4/CO_2	1,7
100000	7	$^{235}\text{UF}_6/^{238}\text{UF}_6$	1,4
100000	7	CH_4/CO_2	27,4

Table 2.1. Comparison of separation factors for classical isotope and natural gas contaminant separations in a gas centrifuge

line the working principle of the countercurrent centrifuge. The basics are the same as previously reported: a high speed rotating hollow cylinder, filled with gas and a mole fraction gradient over the radius (fig. 2.1). Now a small internal circulation is imposed, either thermodynamically by heating at the bottom and cooling at the top or mechanically. This recirculating flux is varied in order to find the optimum performance – we shall see below that it is related to the Peclet number. It is also obvious that it cannot be much larger than the feed rate because this will slow down the process. Due to this circulation the gas is moving upwards at the centre and downwards at the outer wall. The upward moving stream is continuously enriched in the lighter element due to diffusion along the concentration gradient resulting from the imposed centrifugal field. In the downward streams the opposite occurs. A gas feed is added at the point on the axis where the feed composition is equal to the local composition. This is required to prevent mixing at the feed point. At the top and bottom of the centrifuge the product and waste are collected by scoops. This working principle of the countercurrent centrifuge is shown schematically in fig. 2.4. Note that the radial flux can occur via the porous channelled medium which we have previously introduced in order to suppress turbulence which would disable the centrifugal separation [10]

Bulk Flow Field

Fig. 2.5 represents the flow field in the bulk volume of the centrifuge. As indicated in fig. 2.4 the motion is upwards near the middle of the centrifuge and downwards near the wall. There is a requirement of course that for pure recirculation (i.e. when there is no material added or withdrawn) then along any radial line the net upward mass flow must balance that downwards (i.e. the fluxes integrated across the axial cross sectional areas.)

Since the velocity field inside the centrifuge is mainly axial we non-dimensionalise the axial mole flux with respect to the magnitude of the upward mass flow. We define this countercurrent mass flow (kmol/s) ϕ_{mc} as the total mass flow of the internal circulating stream flowing upward in the center of the centrifuge ϕ_{mc} from $r = 0$ to $r = r_1$, where r_1 is the radius $0 < r_1 < r_0$ at which the axial velocity $v_z = 0$. Due to mass conservation this mass flow is equal to the mass flowing down in the outer radii of the centrifuge. (Previously the value of the summed axial flow is taken as a

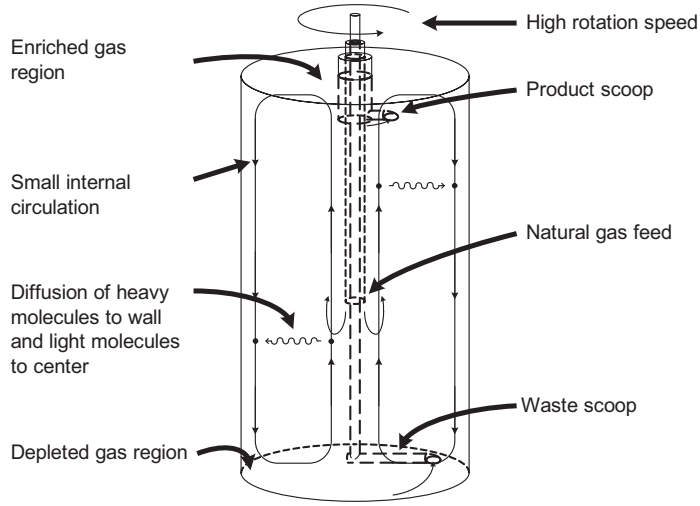


Figure 2.4. Schematic of countercurrent centrifuge.

scaling parameter [20] – this is twice our own nondimensionalising factor.)

$$\phi_{mc} = 2\pi \int_0^{r_1} \rho v_z r dr \quad (2.10)$$

This then leads to our definition of the dimensionless mole flux $(\rho v_i)^*$ profile in direction i which for the axial direction leads to

$$(\rho v_z)^* = \frac{r_0^2}{\phi_{mc}} \rho v_z \quad (2.11)$$

and for the radial direction results in

$$(\rho v_r)^* = \frac{r_0 l_0}{\phi_{mc}} \rho v_r \quad (2.12)$$

The definition of eq. (2.11) and (2.12) requires that the integral of $(\rho v_z)^*$ from 0 to r_1 is equal to 1. Since this is not the case for the velocity profiles used in this study, it is required that the left-hand sides of eq. (2.11) and (2.12) are multiplied by a normalisation factor, β . This normalisation factor can be calculated by inserting eq. (2.11) into eq. (2.10), adding the desired velocity profile and solving the resulting equation for $\phi_{mc} = 1$. (For the velocity profiles discussed here, the normalisation factor $\beta = 5.8$.)

Because we need to calculate flows in both the z and r directions, we make use of the stream function – a scalar function Ψ which fully describes a 2D-flow field. In this case the flow field is axi-symmetric and therefore 2D. The axial and radial velocity

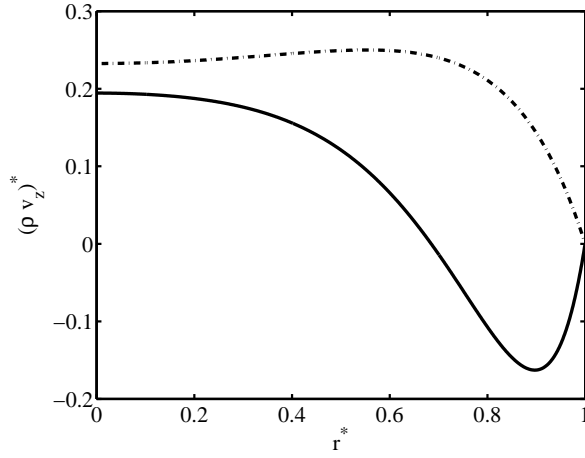


Figure 2.5. Countercurrent flow profiles in a centrifuge. Solid line: circulating flow, $F = P = W = 0$; dotted line: flow above feedpoint, $\phi_{mc} = 0$, $P/F = 1$.

field can be calculated by taking respectively the radial and axial derivative of the stream function i.e. $(\rho \mathbf{v})^* = \nabla(\rho \Psi)$

In order to calculate the dimensionless velocity field or stream function the full Navier-Stokes equations have to be solved. A full Direct Numerical Simulation (DNS) is not possible due to the high Reynolds numbers involved. For example, simple developed axisymmetric pipe flow can be modelled by DNS for Reynolds numbers up to 15000. In that case the largest computer in the Netherlands requires 3 months calculation time in order to get sufficient information on random fluctuations. Note that in our case, because of higher pressure, the Reynolds numbers is larger than for the isotope case – and required computer power increases exponentially with Reynolds number. Because of this complexity, an approximate solution will be used [11]:

$$\rho \Psi = e^{-x} (1 - e^{-x} - x e^{-x}) \quad (2.13)$$

where $x = A_\Psi (1 - r^{*2})$ and $A_\Psi = v_w^2 \bar{M} / (2RT)$

Eq. (2.13) is the analytical solution for the bulk flow in case the countercurrent stream is generated by a linear axial temperature gradient on the wall. This solution is an approximation of the solution for a stream generated by heating and cooling bottom and top end-caps [10], which is the accepted method for convectively ensuring recirculation in the centrifuge. This is of course an arbitrary solution, but has been shown previously to be of validity for modelling countercurrent flow in a centrifuge.

Flow field at ends

Since there is no z -dependent part in eq. (2.13) it actually describes an infinitely long centrifuge. In an actual centrifuge with a finite length the flow reverses at the top and bottom in very thin boundary layers, the so-called Ekman layers [10]. To avoid

complexity these layers are modelled using a very steep exponential function; mass conservation is preserved:

$$\rho\Psi = e^{-x} (1 - e^{-x} - xe^{-x}) \left(1 - e^{-\frac{z-z^*}{\lambda}}\right) \left(1 - e^{-\frac{1-z^*}{\lambda}}\right) \quad (2.14)$$

where λ is the dimensionless reversion layer thickness.

Input and output flow fields

So far only the flow field resulting from the countercurrent motion has been considered. The actual flow field also incorporates the flow induced by the feed stream and product and waste outlet. This flow can be described in a similar way as done for the circulating flow, however the non-dimensionalisation factor is now the feed flow rate F :

$$f_z(r^*, z^*) = \frac{r_0^2}{F} (\rho v_z)_{PW} \quad (2.15)$$

and

$$f_r(r^*, z^*) = \frac{r_0 l_0}{F} (\rho v_r)_{PW} \quad (2.16)$$

where F is feed flow rate (kmol/s) at the injection point $z^* = z_F^*$ and f_i dimensionless mole flux profile of the feed/product/waste flow in direction i .

Normalisation factors may be required, depending on the mole flux profiles that are used. These can be incorporated in equation (2.15) and (2.16) in a similar way as described above. The dimensionless mole flux profiles, f_z and f_r , are calculated using analytical solutions by Brouwers [10, 11]. According to this work, the feed-product-waste flow is positive above the feed point and negative below it. This phenomenon is modelled by a continuous function with a finite gradient to stabilise the numerical simulations. The full feed-product-waste dimensionless mole flux profiles are:

$$f_z(r^*, z^*) = \frac{1}{2} e^{-(1-r^{*2})} (1 - e^{-(1-r^{*2})}) \left[\Theta \left(\tanh \left(\frac{(z^* - z_F^*)}{\lambda_F} \right) + 1 \right) / 2 + (1 - \Theta) \left(\tanh \left(\frac{(z^* - z_F^*)}{\lambda_F} \right) - 1 \right) \right] \quad (2.17)$$

$$f_r(r^*, z^*) = \frac{1}{r^*} \frac{\left((\tanh((z^* - z_F^*)/\lambda_F))^2 - 1 \right)}{2\lambda_F} \times \left(\frac{1}{2} e^{-(1-r^{*2})} - \frac{1}{4} e^{-2(1-r^{*2})} - \frac{1}{4} \right) \quad (2.18)$$

Similarly we can define the output product stream as

$$P = 2\pi \int_0^{r_1} (\rho v_z)_{PW}|_{z^*=1} r dr = 2\pi \int_0^1 \xi f_z|_{z^*=1} r^* dr^* \quad (2.19)$$

where ξ is the normalisation constant, calculated by:

$$\xi = \frac{1}{2\pi \int_0^1 e^{-(1-r^{*2})} (1 - e^{-(1-r^{*2})}) r^* dr^*} \quad (2.20)$$

which has a value of 1.6 for our study. P is the product flow rate and Θ is product/feed ratio. The total flow field is calculated by superposition of the countercurrent velocity field and the feed/product/waste velocity field:

$$\rho v_z = \frac{\phi_{mc} \beta_{cal}}{r_0^2} (\rho v_z)_0^* \quad (2.21)$$

where

$$(\rho v_z)_0^* = \left((\rho v_z)^* + F_0 \frac{\xi}{\beta} f_z(r^*, z^*) \right) \quad (2.22)$$

and $F_0 = F/\phi_{mc}$. (The physical meaning of these parameters is discussed below.) Using the balancing procedure described in our previous work whereby the difference in component mass flow in and out of an axial section is equated to the radial induced flow through the corresponding annulus and considering stationary operation only, the convection-diffusion equation for the countercurrent centrifuge becomes in dimensionless form:

$$\begin{aligned} \phi^* \left[(\rho v_z)_0^* \frac{\partial x_1}{\partial z^*} + (\rho v_r)_0^* \frac{\partial x_1}{\partial r^*} \right] &= \frac{1}{r^*} \frac{\partial}{\partial r^*} \left(r^* \frac{\partial x_1}{\partial r^*} + 2A_0 x_1 (1 - x_1) r^{*2} \right) \\ &+ \alpha^2 \frac{\partial^2 x_1}{\partial z^{*2}} \end{aligned} \quad (2.23)$$

The significance of ϕ^* , A_0 and α are now discussed.

Controllable parameters

Based on the nondimensionalisation to reach eq. (2.23) the three independent dimensionless numbers can be identified in this equation: ϕ^* , A_0 and α and are defined from the derivations as:

$$\phi^* = \frac{\phi_{mc}}{\rho D l_c} \approx \frac{r_0^2 v}{D l_c} \quad (2.24)$$

This represents the nondimensionalised recirculating flow defined above. We have in fact nondimensionalised the inertial flow with the diffusive flow – when simplified, this parameter is the same as the more familiar Peclet number Pe . Physically this means that the small internal circulation introduced above is on the order of 10^{-5} kmol/s. ϕ^* is a variable parameter – we shall see that it is the only parameter with an optimal value for separation. Working back through eq. (2.24) and (2.10) we arrive at the value of the order of 10^{-5} kmol/s. The optimum value of near unitary Pe number

is also explained physically by the fact that the inertial processes must not dominate the diffusive process otherwise poor separation will be achieved.

$$A_0 = Ar_0^2 \quad (2.25)$$

This represents the non-dimensionalised centrifuge instrument parameter and contains the interaction between the gaseous material (the molecular weight thus) and the mechanical parameters of the centrifuge, namely the radius and the rotational speed.

$$\alpha = \frac{r_0}{l_0} \quad (2.26)$$

This number is the aspect ratio of the centrifuge. These numbers fully determine the outcome of the equation and are a function of the design parameters ϕ_{mc} , l_c , v_w and the radius/length ratio of the centrifuge. With the addition of feed, product and waste flows, two more variables enter the equation, namely F_0 the feed rate nondimensionalised against the recirculating flow

$$F_0 = \frac{F}{\phi_{mc}} \quad (2.27)$$

and Θ defined by the product flow to feed flow ratio

$$\Theta = \frac{P}{F} \quad (2.28)$$

So in total 5 independent variables (eq. (2.24)–(2.28)) can be identified in the convection-diffusion equation of a countercurrent centrifuge.

2.1.4 Results

The influence of these 5 variables is investigated using numerical simulation of the convection-diffusion equation. As in our previous work, Aspen Custom Modeler (ACM) is used to solve equation (2.23). Boundary conditions of the countercurrent centrifuge are similar to those of the batch centrifuge, except for the feed point. At this point, located somewhere on the axis, the boundary condition is that of a fixed composition instead of mass conservation. The exact location of the feed point on the axis can not be chosen arbitrarily; in order to prevent mixing the feed point has to be chosen such that the feed composition is equal to the local composition. This process of selecting the feed point location is dependent on the solution of the convection-diffusion equation, which in turn is dependent on the feed point location. Therefore, the location of the feed point has to be determined iteratively. Also, the feed point location is dependent on the 5 independent variables, i.e. a change in one of these variables inevitably leads to a change in the feed point location. In real life application this does not lead to any problems: countercurrent centrifuges are meant to be operated in steady-state conditions. In case of the simulations mentioned above the feed point matching adds more complexity to the numerical solving process.

Using ACM the convection-diffusion equation is solved for a standard case (see table 2.2). This standard case is defined using existing knowledge and consideration of

ϕ^*	2,73
A_0	1,4
α	0,06
F_0	0,92
Θ	0,4

Table 2.2. Controllable parameter values expressed in the nondimensionalised form corresponding to the standard case used in the simulations.

mechanical properties. It is known that the peripheral velocity of the centrifuge should be as large as possible and due to mechanical limitations this can be anywhere from 350 to 800 m/s. This is based on commercially available ultra-centrifuges which we are developing for an experimental program. An example is a commercial centrifuge manufactured by Beckman Coulter and modified by us, which rotates at 100000 rpm and has a diameter of 14 cm with a corresponding peripheral velocity of 750 m/s [11]. A quite moderate value is thus 500 m/s which is selected for the standard case. Together with $\Delta M = 28$ g/mol for CH_4/CO_2 mixtures this leads to $A = 1.4$ for ambient temperature conditions. The radius/length, α , ratio depends on the required axial stiffness and can range from 0.02 to 0.2 or even larger. Previous research on isotope centrifuges indicates that α should be as small as possible [30, 9]. Therefore a value of $\alpha = 0.06$ is selected for the standard case. For the product/feed ratio also a moderate value is selected on the bases of literature: $\Theta = 0.4$; any value from 0 to 1 can of course be selected. The last two variables, F_0 and ϕ^* , depend on feed composition and required enrichment. Again a feed mixture of 50 mole% CH_4 and 50 mole% CO_2 is considered. The product stream should have a composition of 80 mole% CH_4 . (This leads to a feed flow of $3 \cdot 10^{-3}$ mol/s.) The 5 independent variables are varied one at a time, i.e. 4 variables are kept at their value for the standard case. Results of these simulations are shown in fig. 2.6.

The ranges of fig. 2.6 are chosen such that they comply with realistic conditions. The lines drawn in the figures are trend lines. Fig. 2.6(d) and 2.6(e) show the most important and obvious trend: an increase in the feed flow rate results in a decrease of the enrichment. It is concluded from fig. 2.6(a) that there is an optimal ϕ^* -value which leads to a maximum enrichment at a given flow rate. This means that ϕ^* can not be chosen arbitrarily; only one ϕ^* gives the maximum efficiency. An increase in A results in a strong increase in enrichment. This works two ways; for a certain enrichment level an increase in A results in an increased flow rate, i.e. higher production levels are possible for higher values of A . Thus performance increases with increasing peripheral velocities and molecular weight differences – this is in line with the earlier presented results of the batch centrifuge [24]. Varying the radius/length ratio has a large influence on the enrichment; the smaller this ratio, the higher the enrichment. The dynamic properties of the centrifuge limit its length. e.g. the bending stiffness, a function of the radius/length ratio, should be high enough to withstand the vibration forces that occur due to the high speed rotation [26].

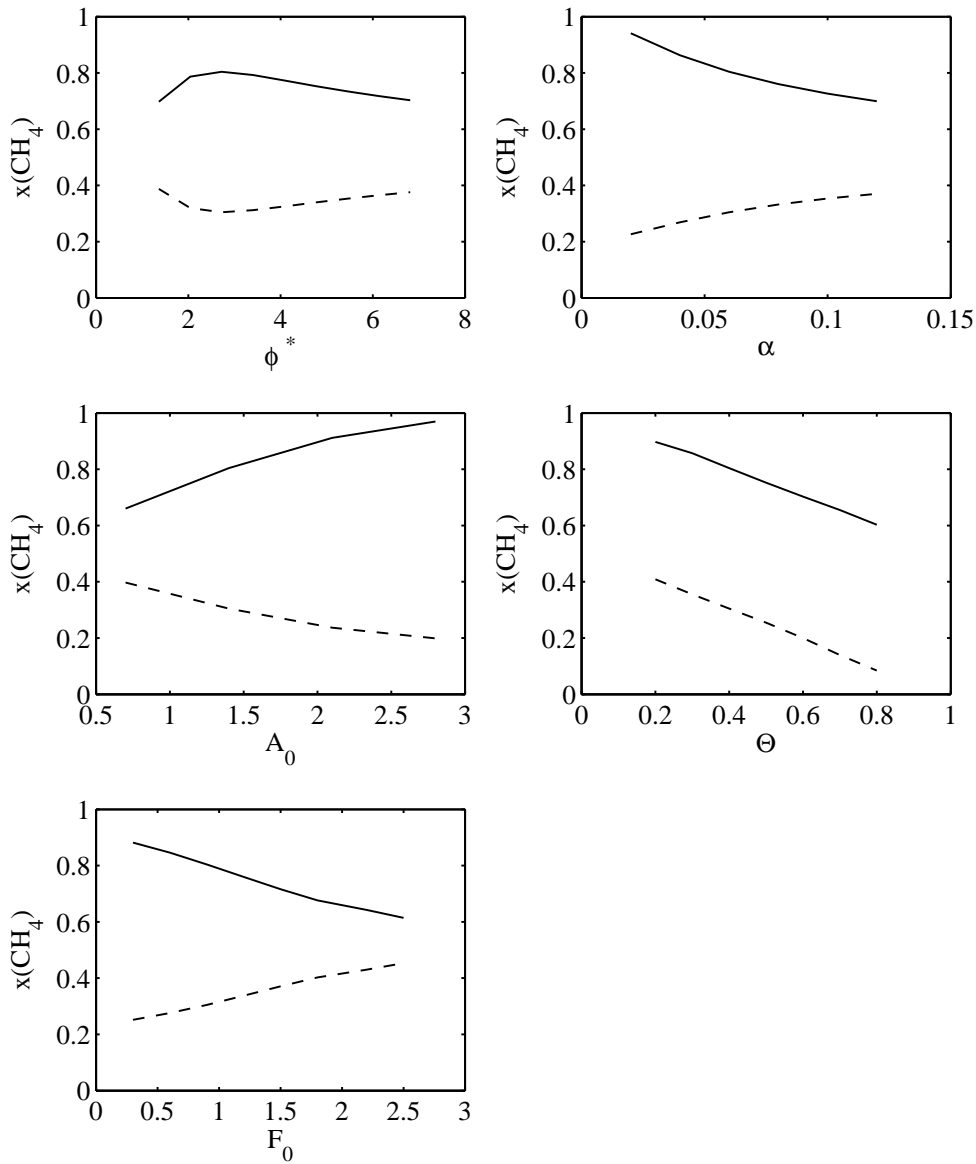


Figure 2.6. Concentration x_{CH_4} in product and waste streams as a function of the 5 independent variables, x_{CH_4} vs (a). ϕ^* – normalised convective recirculation/diffusive ratio, (b) A_0 – centrifuge operating parameters (c), α – aspect ratio, (d) Θ – product-feed ratio and (e) F_0 – feed/recirculation ratio.

The product/feed ratio has no real influence on performance. It can be used to set the balance between enrichment and depletion of product and waste, i.e. a lower product/feed ratio results in a higher enrichment of the product and a lower depletion of the waste. Using these results and considering material limitations an optimised centrifuge configuration is calculated for the 50/50 CH₄/CO₂ case. Commercial available centrifuge cores can rotate with a maximal peripheral velocity of 750 m/s. The minimum value of the radius/length ratio is 0.02 for these units. Setting the product/feed ratio at 0.3 results together with the above values to a maximum flow of $8 \cdot 10^{-5}$ kmol/s for an enrichment from $x_{F,CH_4} = 0.5$ to $x_{P,CH_4} = 0.7$ in a 5 metre long unit. The optimal value for ϕ^* is in this case 2.8. Although significantly enhanced, the available throughput still falls far short of the desired level for natural gas separation.

2.1.5 Conclusions

1. Centrifugation of a contaminated gas mixture into a gaseous product (CH₄) stream and gaseous waste (CO₂) stream can not be carried out fast enough to perform the separation in one or a small number of units at the required commercial rates (100's MMscf/d i.e. on the order of 100 tons per hour). The schemes using large numbers of centrifuges in cascades are not economically feasible for natural gas.
2. Centrifugal separation of natural gas has a significant number of component and process differences from the separation of isotopes. The lighter molecular weights and large product and waste molecular weight differences lead to non-unity separation factor. The correct analysis for the non-unitary values of separation factor has been carried out.
3. The enhancement due to countercurrent centrifugation compared to the batch process is still not sufficient to make the gas-gas process interesting.
4. All calculations in this work were based on the example of a 50/50 CH₄/CO₂ mixture. In real applications, contaminated gas fields extend from the currently treatable limit of ca. 10% CO₂ to up to 70% CO₂. At the lower level of contamination the relatively smaller concentration gradient will increase separation times. At higher concentrations the effect of condensation on the centrifuge will become much more important and since this is a fast process, the separation will occur more quickly.
5. Increasing the separation rates requires boosting the mass transfer rates and spatial separation rate of product and waste. Using the radial pressure gradient to cause phase separation is one way forward and this is the focus of our current modelling and experimental efforts. This would require some cooling: for example for the 50/50 CH₄/CO₂ mixture analysed in this study, the temperature needs to be below -10 °C so that compression will cross the dewpointing curve. However many of the fields have higher levels of contamination – for a 70% CO₂ field, this temperature is only 9 °C. Cooling the gas is in itself no problem, as the high reservoir pressures make expansion cooling a straightforward procedure.

6. In the above study we were concerned with removing a single contaminant from a pure natural gas stream. In reality of course, gas streams contain multiple components of different molecular weights. The only difference this would make is the complexity of the equations. In the above treatment all equations are binary – there is one component and the other one is complementary. An additional component simply doubles the calculation time. For transparency, and in order not to obscure the essential physics, we confined our calculation to the binary case in order to home in on the essential problem – however the result is equally valid for multiple components.

2.2 Gas centrifugation with wall condensation[†]

2.2.1 Introduction

As we have shown in the previous section, separation of CO₂ from CH₄ using the principles of gas centrifugation is not an economically viable process. However, a separate study [23] indicates that this process can be greatly accelerated by increasing the pressure. Increasing the pressure is not that helpful for component separation in the gas phase, because to a first approximation the product of diffusion constant and pressure pD is constant i.e. at high pressures the diffusion constant decreases [24]. However at the higher pressures generated in a centrifuge, there is a second much more dominant mechanism which will also cause separation - namely condensation due to the radial compression [21]. This effect has some similar physical properties to what happens in the so-called evaporative centrifuge which has been previously analysed for isotope separation and which we have recently shown to be quite different from natural gas separation behaviour in a centrifuge [44].

In this study we examine whether condensation speeds up the separation process for a contaminated natural gas scenario. We identify two mechanisms for this condensation. A model is constructed which simulates the effect of condensation by centrifugal enrichment. The results of this model are compared to results of simulations of a gas/gas centrifuge. It is investigated in how far the concept of wall condensation leads to a significant increase of the separator performance in comparison with that of pure gas/gas separation by centrifugation.

2.2.2 Theory and Model

Fig. 2.7 shows the condensation curves at different temperatures for various mixtures of methane/CO₂ as a function of the concentration of CO₂ in the mixture. This was calculated using an extended equation of state program based on a cubic equation of state of the Soave-Redlich-Kwong type. There are, in the case of a condensing centrifuge, two mechanisms for condensation. Pure *compression* work corresponds to moving up the vertical pressure line: e.g. with a 50/50 CO₂/CH₄ mixture at -25 °C, if we increase the pressure (e.g. along the radius of the centrifuge rotor) then around 4 MPa, condensation of a CO₂ rich waste liquid starts to occur. Pure *enrichment* work corresponds to moving horizontally to the right whereby the local concentration of CO₂ at any point is increased as a result of centrifugally induced diffusion. For example, if we started with a 2,5 MPa 50/50 mixture of CO₂/CH₄ and allowed CO₂ enrichment to proceed near the rotor wall, then around $x_d=0.6$, condensation will occur.

Thus, rather than considering fig. 2.7 to be a curve which shows condensation pressure p_d as a function of composition x , we may equally well consider it as a curve which shows the condensing composition x_d as a function of pressure p . It is with this latter function which we are concerned and which forms the focus of our effort to see to what extent condensation enhances centrifuge performance above pure gas/gas

[†]Partially reproduced from: van Wissen, R.J.E., Golombok, M., Brouwers, J.J.H. Gas centrifugation with wall condensation, A.I.Ch.E. Journal 2006; 52(3): 1271–1274

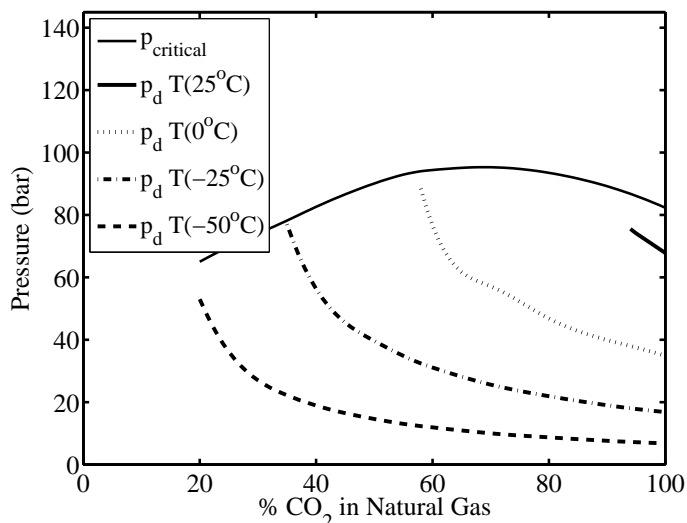


Figure 2.7. Condensation curves at different temperatures as a function of %CO₂ in natural gas. Thus $p_{sat}(T)$ refers (for temperature T) to the pressure at which the first condensed liquid forms (also known as the “dewpoint”). The envelope gives the critical pressure denoted “ $p_{critical}$ ”.

operation. We want to resolve and extrapolate pure compression and pure centrifugal enrichment contributions to separation.

The core idea in this work is thus to operate the centrifuge with a sufficiently high feed pressure that when the gas mixture is spinning, then at a certain radius, condensation will occur. This idea is shown schematically in fig. 2.8. Initially the process runs identically to the gas-gas centrifuge. However at one point along the radius, at $r = r_d$, the pressure is sufficient that the condensing pressure is reached. Initially when the pressure profile is (almost instantaneously) established, we still have a uniform composition throughout the cylinder, because the diffusion process concentrating CO₂ near the wall occurs much slowly than the fast pressure generation profile - at this point r_d is determined purely by the partial pressure. Subsequently centrifugally driven mass transfer occurs of CO₂ from the centre to the outer region of the centrifuge. This net transport of CO₂ has the effect of shifting condensation closer to the centre to the equilibrium value.

The region where condensation occurs is shown in fig. 2.8 by the shaded area where the pressure exceeds that required for condensation of liquid (referred to as the “dewpoint”). The condensing separation is faster than pure gas-phase separation because CO₂ is removed from the gas phase. This will act to further drive the mass transport of CO₂ from the centre to the outer radial annulus.

In our analysis of the condensing centrifuge we have followed the techniques and criteria which we have previously derived [24]. Since the fundamental concern is to

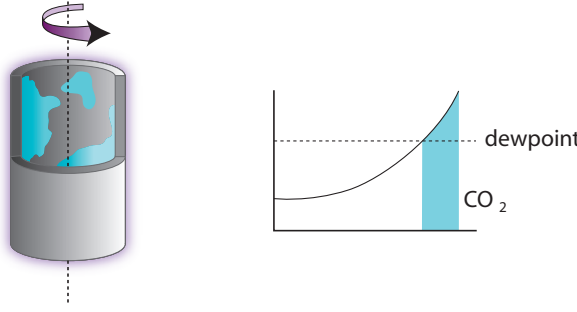


Figure 2.8. Principle of operation for condensing centrifuge.

determine whether the condensation will help speed up the centrifugal process, we perform our calculation with respect to the batch process in order to determine the reduction in separation time due to condensation. The unit is filled with gas to a feed pressure just below the condensation pressure for the mixture (in this case 50/50 CH_4/CO_2). The mixture is then spun up and instantaneously acquires the centrifugal pressure profile with uniform feed composition. There is thus a portion of radially uniform concentration gas near the wall which is at a pressure above the condensation pressure. Condensation of CO_2 rich liquid occurs rapidly and is considered removed from the system. However this has the effect of changing the total composition of the remaining gas phase and reducing the total number of gas molecules thus leading to an overall pressure reduction so that condensation stops. The remaining gas now undergoes a much slower centrifugal enrichment process to a new radial composition distribution. The composition distribution is enriched in CO_2 near the wall so that the local condensing pressure is exceeded and the process iteratively cycles until no more condensation occurs.

In a gas centrifuge, the dimensionless partial differential equation describing the time-dependent mole fraction distribution of one component is [44, 20]:

$$\frac{\rho R^2}{\rho D} \frac{\partial x_1}{\partial t} = \frac{1}{r^*} \frac{\partial}{\partial r^*} \left(r^* \frac{\partial x_1}{\partial r^*} + 2(A_2 - A_1) x_1 (1 - x_1) (Rr^*) \right)^2 \quad (2.29)$$

where D is the diffusion coefficient (m^2/s), ρ the mixture mass density (kmol/m^3), r_0 the wall radius, r^* the dimensionless radial coordinate, defined as $r^* = r/R$, t denotes time (s), x_i the mole fraction of component i . Whereas for a centrifuge where only gas-gas separation occurs, the boundary conditions are constant, in a condensing centrifuge these vary continually and are a function of composition. Condensation occurs, resulting in liquid, which because of its higher density and the large centrifugal forces, is pushed to the wall, where it is extracted. This removal of mass from the system results in new boundary conditions - those for the gas/gas case are no longer valid. The feed concentration is equal to the condensation concentration for the wall pressure at $t=0$:

$$x_{Feed}(r^*, t=0) = x_{Dewpoint}(p_{wall}(t=0)) \quad (2.30)$$

Any liquid that is formed by condensation is considered to be removed instantaneously. Since this will only occur at the wall, it is sufficient to correct the boundary conditions at the wall:

$$\text{if } p_{wall} \geq p_{sat} \text{ then } x(Rt) = x_{Dewpoint}(p_{wall}(t)), \text{ for } 0 < z^* < 1 \quad (2.31)$$

Equation (2.29) is solved using the finite volume method in Aspen Custom ModelerTM (ACM - an equation oriented modelling package) and the boundary conditions discussed above. The problem is set up as spatially axisymmetrically discretised along a uniform grid and time integration is performed with a fourth order Runge-Kutta algorithm. Peripheral velocity and centrifuge length are the only two independent design variables; this can be seen in eq.(2.29) which is dependent on the *product* of w^2 (in A_i) and R^2 , i.e. the peripheral velocity. Radial velocity and wall radius are therefore not independent parameters. The centrifuge has a length of 1 m. All condensed liquid is considered to be removed instantaneously. The remaining gas is considered to be the product gas. Product flow is calculated by dividing the gas mass by the time required to perform the separation. Since product flow and product enrichment, i.e. product composition, are not independent variables, the product flow is calculated as a function of the enrichment level that the gas/gas centrifuge would have at the given peripheral velocity. It has been previously shown that one cannot [21, 44] realistically use the steady-state enrichment level of the non-condensing gas-gas centrifuge, as this would take infinitely long to achieve, but an enrichment level that is 90 % of this steady-state enrichment. The time, τ_{90} , to reach this 90 % of equilibrium enrichment, is used to calculate the product flows of the non-condensing gas-gas centrifuge. This enables us to compare the performance of the condensing centrifuge with the non-condensing, purely gas phase centrifuge.

2.2.3 Results and Discussion

Fig. 2.9 shows that condensation processes yield a product flow that is approximately twice that of the gas/gas centrifuge. The doubling of the removal rate due to condensation of a centrifugally enriched mixture is still small compared to the pure compression work which removes a large amount of the CO₂. Note that we are here focussing on the removal due to enrichment work decreasing the condensation pressure i.e. we have specifically excluded the compression work. Independent of inlet conditions, we first remove all condensed material assuming rapid phase separation under the imposed pressure gradient. If however, the compression removal is included then of course a much higher throughput can be obtained - however a gas centrifuge is not the ideal way for carrying out compression - although it does have the advantage of a predetermined spatial separation of gas and liquid phase inside the rotor, as opposed to the spatially uniform behaviour in a compressor. In any case, for pure centrifugal condensation, the rate is still dependent on the CO₂ molecules diffusing to the wall where they concentrate sufficiently to decrease the local condensing pressure below the local quasi-stationary pressure. The process thus still depends on diffusion, but over a smaller distance.

This model has used a batch centrifuge to calculate the time required for separation. It has previously been shown that the countercurrent continuous process is

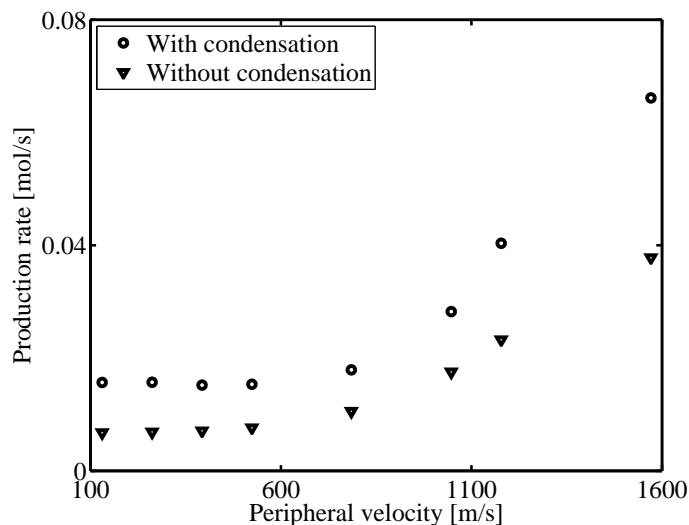


Figure 2.9. Production as a function of peripheral velocity for enrichment levels equal to that of the gas/gas centrifuge.

faster than the batch version by a factor of 2-5 depending on operating conditions - however this augmentation in process rate is certainly not by the order of magnitude which we require for commercial utilisation. It is thus unfortunately clear, that a countercurrent condensing centrifuge will not enable sufficiently fast separation to be of commercial interest. Although there is some improvement, product flows are still of the same order of magnitude. Our own experiments [23] indicate that an improvement of several orders of magnitude is required to make gas/gas centrifugation a viable option for removing contaminating gases from natural gas streams. Condensation by compression has more potential, since it is not a diffusion dominated process. However, since the gas centrifuge is not a dedicated compression device, and the benefits of the centrifugal enrichment are limited, it is better to seek for other means to optimise this process.

Finally, it is worth drawing attention to one interesting result. The major application of centrifuges to date has been for separating out isotopes of UF_6 . In that process, low pressure (and thus low throughput) operation is required in order to avoid reaching the desublimation pressures of UF_6 (0.016 MPa at 20 °C) which unbalance the spinning cylinders due to asymmetric solids formation on the walls. This is not a problem if liquids could be formed as they will spread symmetrically around the rotor circumference. This would require operation between the triple point of UF_6 (64 °C, 0.1 MPa) and the critical point of that material (233 °C, 4.7 MPa). In that regime a liquid/gas boundary can be formed for condensation in the scheme we have identified above. We wonder whether the process we have described in this study has ever been considered for uranium enrichment - normally, higher temperatures are avoided because the equilibrium separation is less favourable - however in this case

there is a clear processing advantage. The higher production rates here are still of interest because of the higher unit value of the enriched isotope compared to natural gas.

2.3 Condensed contaminant centrifugal separation (C3-sep)[‡]

2.3.1 Introduction

Pure gas/gas centrifugal separation is even with partial condensation not a very fast and thus economically interesting process. A much faster process is that of Condensed Contaminant Centrifugal Separation: C3-sep. It has two steps:

- Cooling the gas to a temperature whereby the gaseous contaminant becomes liquid in the form of a mist of micron-sized droplets.
- Separating the mist from the gas by the rotational particle separator (RPS) a device which has already found application in such areas as domestic healthcare and environmental emission control [14, 15] and which is a spin-off of the gas-centrifuge [16]. This is the core innovatory element in our process.

The idea of gas/gas separation via transition of one of the gaseous components to liquid or solid aerosols and subsequent removal by the RPS arose with the inception of the RPS in 1987 [12, 13]. Initial applications thought off were removal of water vapour from air [12, 13] and filtering of gaseous salts and heavy metals from biomass conversion installations [18]. The concept is particularly suited for the application of CO₂ and H₂S removal from natural gas as it is not hampered by high energy demands and involves very short residence times (i.e. compact units). It has the potential to boost recoverable gas reserves by amounts which are energetically equivalent to multi-billions of barrels of oil. We now examine each of the two steps in greater detail: section 2.3.2 examines the thermodynamics and section 2.3.3 deals with the separation device.

2.3.2 Thermodynamics

To achieve feasible gas/gas separation in an economically attractive manner, one of the components has to be transformed into a phase capable of forming particles. This can be achieved by cooling and condensation. Since gas in reservoirs is already compressed (130–450 bars is typical), then expansion can be used to attain the necessary cooling for contaminant condensation. Even the reduced pressures available top hole (80–130 bar) are still sufficient to drive expansion cooling. An expansion turbine is in most cases preferred to techniques employing expansion by acceleration such as the Joule-Thompson process. The turbine can be used to drive a compressor to bring the gas back to system pressure. In addition, after the turbine the velocity of the gas can be kept relatively small, cooling occurs by withdrawing power from the gas rather than from gas-speed. This avoids the risk of heating up by internal friction of the gas - the ultra-fine condensed droplets could easily evaporate.

The low pressure side of the expansion refers to a condition which is sufficient to lead to cooling so that two separate phases form. The product phase is gaseous

[‡]Partially reproduced from: Brouwers, J.J.H., van Wissen, R.J.E., Golombok, M. Novel centrifugal process to access contaminated gas reserves, accepted for publication, Oil and Gas Journal

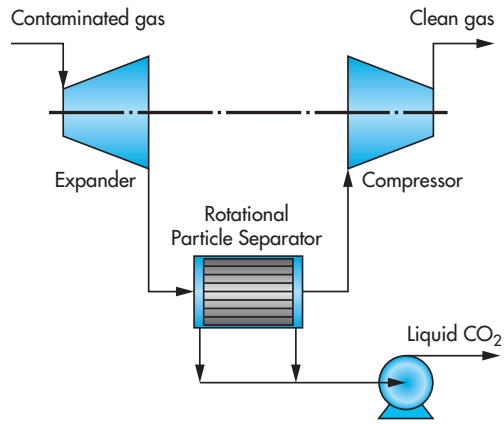


Figure 2.10. Schematic of condensed contaminant centrifugal separation.

and enriched in methane (and thus depleted in CO_2). The waste phase is liquid and is enriched in CO_2 and depleted in methane. Of course this process does not spontaneously lead to a nicely separated liquid and gas phase - a mixture of fine CO_2 rich droplets in a methane riched gas forms. Between the expansion and separation steps the microdroplets have to grow to a sufficient size that they can be separated. This so-called "induction" process is known for knock-out vessels or for example, condensate components using cyclones. However these devices can only be used at high volume throughputs for droplet sizes greater than around $15 \mu\text{m}$ and with much lower mass loadings than are present in contaminated gases. (Removal of smaller droplets is possible but only for extremely low throughputs, so-called microcyclones.) In our case droplet sizes will be smaller than this with mass loading much higher than condensate in gases.

Consider a feed flow (Q_f) of contaminated gas which is split into a cleaned-up stream (Q_c) and a waste stream (Q_w) of CO_2 rich liquid. Conservation of mass requires that input is the same as output

$$Q_f = Q_c + Q_w \quad (2.32)$$

If we define x_i as the concentration of methane in each of the three streams $i = f, c, w$ then a mass balance on the methane component yields

$$x_f Q_f = x_c Q_c + x_w Q_w \quad (2.33)$$

The most obvious condition is that we wish to have the highest concentration x_p of methane possible in the product stream. Simultaneously we need to minimise the loss of incoming feed methane into the waste stream so that the maximum number of molecules of methane in the feed end up in the product stream. This corresponds to maximising the recovery r given by

$$r = \frac{x_c Q_c}{x_f Q_f} \quad (2.34)$$

In the above there are 7 variables with two specified input - the feed composition x_f and the flow Q_f . We calculate the methane content in the clean and waste streams (x_c and x_w) from the pressure and temperature p, T - the remaining unknowns can then be solved using the three equations above. However there is a large range of feasible p, T conditions with corresponding solutions for x_c and x_w . We need to find realistic values which also optimise the recovery r , at the same time.

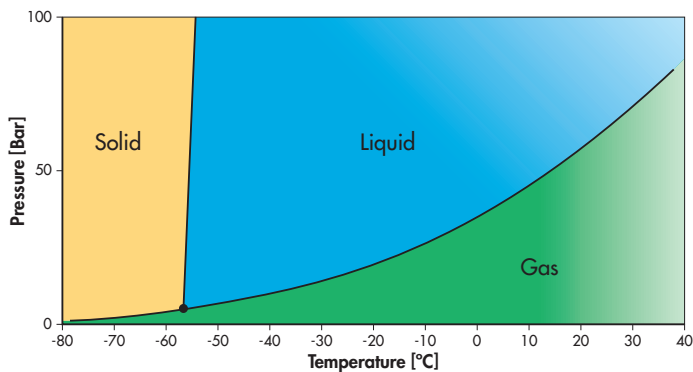


Figure 2.11. Phase diagram for CO_2 showing triple point at 5 bar and -58 C .

Consider a 50/50 mixture of CH_4/CO_2 i.e. $x_f = 0.5$, which is representative for contaminated gas and which we use as a basis of design. We wish to ascertain the optimum values of product concentration x_c and methane recovery r for a variety of pressures and temperatures [39]. The lower bound for these conditions can be obtained from an evaluation of the phase boundary for pure carbon dioxide as shown in fig. 2.11 which shows the freeze-out curve. Most materials have a triple point below atmospheric pressure with normal melting and boiling points corresponding to the temperature points at 1 atm. (i.e. ca. 1 bar) where solid-liquid and liquid-gas transitions occur respectively. However for CO_2 the triple point is actually above atmospheric pressure. For CO_2 $p_t = 5.1\text{ bar}$ and $T_t = -56.6\text{ C}$ - the subscript t referring to triple point conditions. Fig. 2.11 shows that operation in the liquid regime requires that we be above 5 bar and -56 C and this forms the minimum value for our thermodynamic conditions. The maximum value is set by reasonable pressures for the expansion and bearing in mind that this will be after the cooling expansion phase.

Fig. 2.12 shows the methane recovery r plotted against methane product concentration x_c for a range of pressures and temperatures. This was obtained from an extended cubic equation of state simulation based on the Soave-Redlich-Kwong model. This shows that in a single separation step it is possible to get high methane recoveries however the problem is maximising the methane concentration in the product stream. At the ideal point $x_c \sim r \sim 0.85$, the turbine inlet pressure would be 600 bar which is clearly unrealistic. In general - given the restrictions for pipe wall thickness and corresponding safety and handling considerations we would wish to be below 200 bar at the inlet.

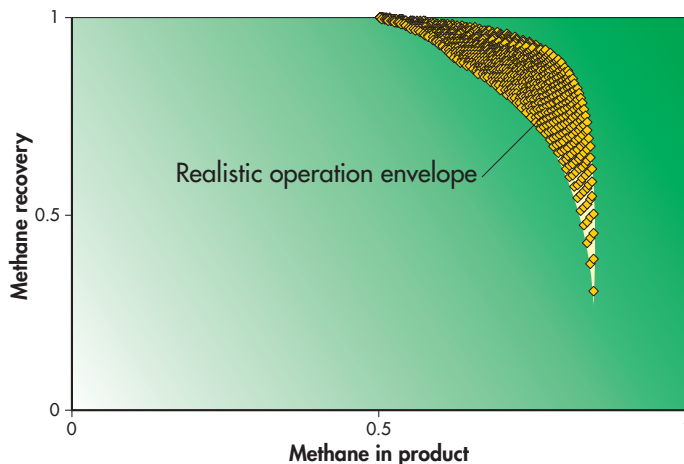


Figure 2.12. Methane recovery as a function of methane concentration in product stream - displayed for a variety of pressure and temperature separation conditions.

The question then is to choose the optimal realistic p, T values for the operation of the separator. If there is too much expansion, the temperature may be sufficiently low but the pressure will be too low for liquefaction to take place. If we restrict the expansion process we may have sufficient pressure but not enough cooling and hence insufficient yield. An examination of the various p, T conditions coupled to the parameters above shows that an expansion to around the regime 25–30 bar providing the inlet pressure is above 100 bar gives significant phase separation.

From a practical engineering standpoint, an inlet pressure of 102 bar to the expander is sufficient to recover ca. 95% of the methane into the product gas stream with a concentration of around 67%. Note that phase separation is only initiated by the expansion and is only complete by the end of the induction period - here the liquid state is materialised in droplets of a few microns in size. Subsequently, the spatial separation of the dispersed waste and purified product takes place in the rotational particle separator. The foregoing analysis assumes that the CO_2 rich liquid is already in the dispersed waste material of flow rate W which will be spatially concentrated and separated to the waste stream in the RPS.

2.3.3 Separation

In section 2.3.2 we evaluated the equilibrium conditions required for formation of a condensed waste phase. In this section we are concerned with the kinetics of droplet removal. This needs to occur within a very short time and for very small droplet sizes. In principle a standard cyclone would be capable of doing this, however for very small droplet sizes a long residence time is required and this is difficult to attain when the throughput is very high. The main advantage of the rotational particle separator (RPS) is that it enables this to happen much more quickly (i.e. at much higher

throughputs) and for much smaller droplets than is the case with other centrifugal methods such as the cyclone or the gas centrifuge.

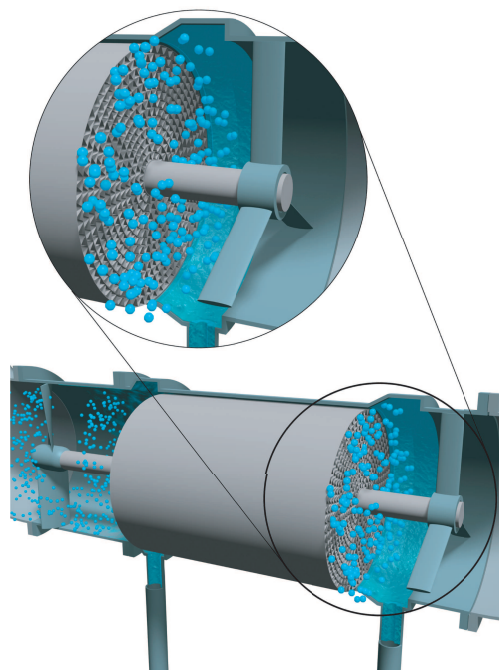


Figure 2.13. Detail of rotational particle separator (RPS) during condensed contaminant centrifugal separation.

The core of the RPS is a cylindrical body which consists of a large number of axially oriented channels with a diameter $1 - 2\mu\text{m}$ [15]. The assembly is mounted on bearings and rotation is induced by swirling the high gas flow. Inside the channels the particles in the gas will move radially to the outer walls by the action of centrifugal force. As the channels are very narrow, particles can arrive at the collecting outer walls during the short residence time and the liquid films formed at the outer walls are squeezed out of the channels and leave the RPS through exit ports (fig. 2.13). The travel distance of a particle is much shorter than in say, a cyclone, so that much smaller particles can be collected. The basis of our separator is thus the use of centrifugal force to separate small condensed droplets from the gas flow. The velocity by which the particles move radially can be calculated from a balance between the centrifugal force and the fluid force which is exerted on the particle in case of motion relative to the surrounding carrier fluid [10]. We can express the critical separable droplet size as a function of three important variables [43]. These are the flow rate Q_f i.e. the feed flow rate of the gas stream, τ the residence time in the separator (effectively a measure of size and thus capital cost) and ϵ the specific energy consumption (i.e. the operating costs). Fig. 2.14 presents a comparison of this last parameter for a number

of level of CO_2 gas stream decontaminations. It is clear that our process compares very favourably in terms of energy consumption.

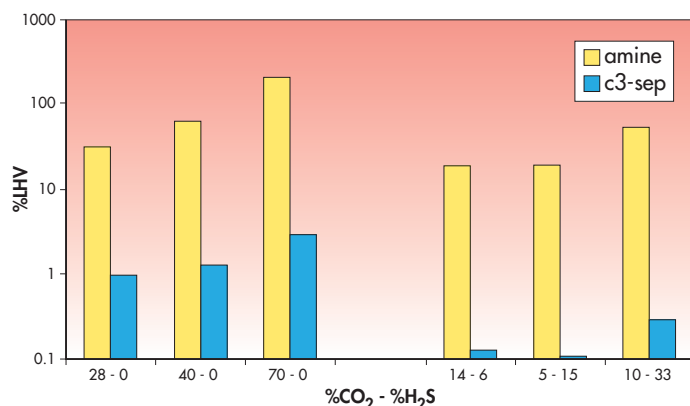


Figure 2.14. Comparison of energy consumption of amine vs. centrifugal process for cleaning gas streams of varying contamination - expressed in terms of lower heating value of clean gas produced.

2.3.4 Conclusion

1. We have presented a process which has a distinct CAPEX/OPEX advantage compared to both the cyclone and amine process. The application of this process represents a potential for enormous decreases in equipment size and energy consumption for gas decontamination.
2. Pressures and temperatures are designed such that dissolved methane in particles and gaseous pollutant in methane are at a minimum ensuring maximum enrichment and depletion of product and waste streams. In cases of very high degrees of contamination it may be necessary to compress the single stage product gas and repeat the process in order to obtain still higher purity.
3. The whole process occurs under pressure so that the size of the unit as a whole is small. Energy consumption is small, costing a few percent of the calorific value of the gas at most. Capital and operating expenditure are therefore low; they form no obstacle for profitable exploitation. For a typical gas field producing methane at a rate of 100 kg/s and contaminated with 50% CO_2 , the nucleation pipe can be designed at a length of 10 m and a radius of 1 m. The RPS has the same radius and a length of 0.5 m; it rotates with a peripheral speed of 50 m/s. Pressures and temperatures downstream of the turbine are typically 25 bar and -50°C . These figures illustrate the attractiveness of the process.
4. Another major advantage here is that whereas standard processes produce CO_2 and/or H_2S contaminant at low pressures, our process automatically generates

the waste stream at high pressures enabling reinjection back into the gas reservoir from which it originally came, while yielding clean natural gas with a much lower net production of polluting gases.

Chapter 3

Thermodynamic and phase change considerations

3.1 Introduction

The core of the C3-sep system is the two-phase equilibrium after the expansion and the spatial separation of the two phases by the rotational particle separator (RPS). In this chapter we look closer at the two-phase equilibrium; the RPS will be discussed in the next chapter. For now we consider the RPS to be a perfect two-phase separator, i.e. we assume that the liquid and vapour can be fully split in the separator, so no liquid will be present in the gas stream.

The thermodynamic evaluation that will follow is focussed on the application of C3-sep in the natural gas industry. Other applications of C3-sep are processes where gases are separated that have a reasonable difference in saturation pressure; C3-sep works only when one component can be condensed while the other is still gaseous. Also, the gaseous component should not fully dissolve in the condensed component as this makes the spatial separation impossible.

The C3-sep process has several applications in natural gas separation:

- Methane enrichment of natural gas streams that are contaminated by CO₂ and/or H₂S.
- Liquid CO₂ extraction from a contaminated natural gas stream, in order to use the CO₂ enriched liquid to inject it into nearly depleted oil fields to get a higher oil recovery.

The latter process is also called enhanced oil recovery (EOR). So the first application is focussed on methane enrichment and the second on carbon dioxide enrichment. For each application the thermal conditions of the C3-sep process have to be determined.

Let us recapitulate what C3-sep does in the natural gas processing case. A natural gas stream containing CH₄, CO₂ and/or H₂S with a surface manifold pressure of 70 to 120 bar and ambient temperature ($\sim 20^\circ\text{C}$) is (if necessary) compressed and cooled to

a pressure of 100 to 250 bar and a temperature slightly above the critical temperature. Subsequently the gas is expanded in a turbine to a certain pressure and temperature such that part of the CO_2 and H_2S condenses; some CH_4 may dissolve in this liquid. Since the cooling takes place by expansion rather than wall cooling, condensation takes place in the medium by homogeneous and heterogeneous nucleation, which results in a mist formation. This mist of liquid CO_2 and/or H_2S droplets is extracted from the gas using the RPS.

The most important thermodynamic parameter in this process is the pressure and temperature after the expansion and partial condensation of the natural gas stream. These pressures and temperatures determine the liquid/vapour equilibrium, and should therefore be chosen such that they are optimal for the desired application. When these thermal conditions are known, the other thermal conditions, i.e. before the expansion, before the cooler and before the compressor, follow from simple thermodynamic calculation: the expansion in the turbine is isentropic, the cooling in the heat-exchanger is isobaric and the compression is again isentropic, all with a certain efficiency.

The first part of this chapter focusses on the thermodynamic conditions before and after the expansion, focussing on both applications, and including an optimisation for an experimental C3-sep unit. A real optimisation of the thermodynamic conditions involves heat integration of the whole process and a economic study on the operational and investment costs of the system as a function of all the design parameters. This will not be considered in this thesis; focus will be on the experimental implementation of the process, so one stage enrichment of either CH_4 or CO_2 . After proving that the process actually works, the commercial applicability and optimisation can be assessed in a future research program.

The last part of the chapter discusses the mist formation after the expansion. The spatial separation in the RPS is dependent on the size of the droplets that are to be separated. Therefore the design of the RPS also strongly depends on the size of droplets. Classical nucleation, diffusion, and monodisperse coagulation theory are used to estimate a range of diameters which can be expected to enter the separator.

3.2 Equilibrium separation for methane enrichment

In order to acquire the optimal thermodynamic conditions for methane enrichment, we focus on equilibrium separation. We thus assume that the residence times between the separate steps in the process, i.e. cooling by expansion and separation, are sufficient to reach equilibrium before the spatial separation in the RPS takes place. In reality, condensation takes a certain amount of time, so an induction section is added to the system. This induction section adds residence time to the system such that the two phase stream is in thermodynamic equilibrium before the separation in the RPS.

So, suppose that equilibrium is reached before the separator, then figure 3.1 schematically depicts what happens after the expansion. A feed stream with mass flow rate Q_f (kmol/s) and a mole fraction CH_4 of x_f (kmol/kmol) is expanded to a pressure p (bar) and a temperature T ($^\circ\text{C}$), which in equilibrium results in a two-phase flow. This two-phase flow is then split up by the separator in a cleaned-up or product

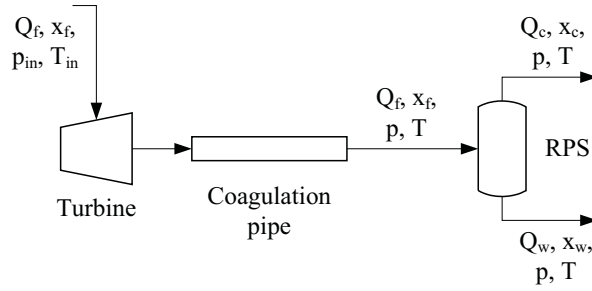


Figure 3.1. Schematic of the expansion and separation process.

gas flow with mass flow rate Q_c (kmol/s) and a mole fraction CH_4 of x_c (kmol/kmol) and a waste liquid flow with mass flow rate Q_w (kmol/s) and a mole fraction CH_4 of x_w (kmol/kmol). These quantities are linked by the total mass balance:

$$Q_f = Q_c + Q_w, \quad (3.1)$$

and the component mass balance:

$$x_f Q_f = x_c Q_c + x_w Q_w \quad (3.2)$$

By rewriting these equations one can derive an expression for the gas (product) flow rate to total flow rate ratio:

$$\frac{Q_c}{Q_f} = \frac{x_f - x_w}{x_c - x_w}, \quad (3.3)$$

and a similar expression for the liquid (waste) flow rate to total flow rate ratio:

$$\frac{Q_w}{Q_f} = \frac{x_f - x_c}{x_w - x_c}, \quad (3.4)$$

which eliminates the need to do calculations with actual flow rates; all equilibrium calculations are a function of the mole fraction CH_4 in the three streams.

The pressure and temperature that are present after the expansion determines the values of x_c and x_w . Now in order to enrich the incoming stream as much as possible in a single stage of C3-sep, it is desirable to maximise the mole fraction of CH_4 in the product stream, x_c . We also want to recover as much as possible of the methane in the product stream; i.e. it is undesirable to have a lot of methane in the waste stream. So we want to maximise the recovery of methane in the product stream, r , which is expressed as the ratio between the number of moles of methane in the product stream and the number of moles of methane in the feed stream:

$$r = \frac{x_c Q_c}{x_f Q_f}. \quad (3.5)$$

Using eq. (3.3) this expression can be rewritten in a form independent of the mass flow rates:

$$r = \frac{x_c(x_f - x_w)}{x_f(x_c - x_w)}. \quad (3.6)$$

In order to optimise the values of x_c and r we have to optimise the pressure and temperature after the expansion. This can be done by using an equation of state model. Using such a model one can calculate x_c , x_w , and thus r for a certain pressure, temperature and feed composition. We use the Peng-Robinson equation of state model and the Aspen Custom Modeler™ (ACM) package to do these calculations. For validation purposes, the results of the ACM calculations are compared with the results of a separate extended equation of state program based on a cubic equation of state of the SoaveRedlichKwong type with pure component parameters fitted to vapour pressures and liquid densities along with a composition dependent mixing rule. This comparison shows that the Peng-Robinson equation of state model is very accurate for CH₄/CO₂ gas/gas and gas/liquid mixtures. Gas/solid and Gas/liquid/solid mixtures are not well predicted by this model. However, in the current conceptual and prototype state of C3-sep we do not wish to have solid formation anywhere in the process, for simplicity and to ensure safe operation, so we will avoid the solid regime anyhow. In the future, after successful implementation of the C3-sep technology, one can of course expand the operational envelope to the solid regime; the RPS is capable of handling solids but considerable efforts will have to be made to design a solid removal mechanism and to prevent solids from clogging up the coagulation pipe, the solid removal channels or even the RPS channels.

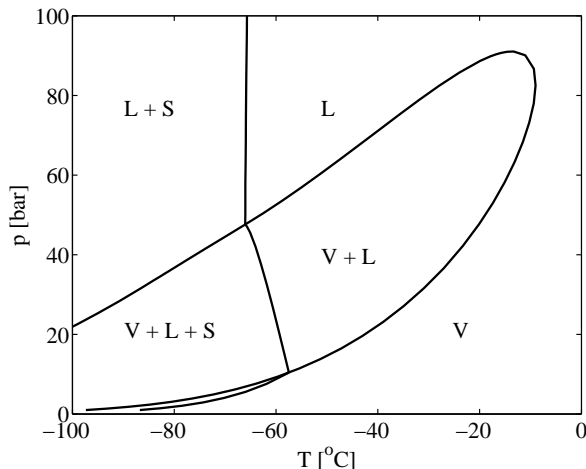


Figure 3.2. Phase diagram of a 50/50 CH₄/CO₂ mixture. Vapour is indicated with V, liquid is indicated with L, and solid CO₂ is indicated by S.

Figure 3.2 shows the $p - T$ phase diagram of a 50/50 CH₄/CO₂ mixture. This phase diagram is constructed using the RK-Soave equation of state model mentioned

above. In ACM we calculate the equilibrium conditions for a grid of pressures and temperatures in the vapour-liquid region, whereby the boundaries of this region are determined by figure 3.2. The required turbine inlet pressure, p_{in} , to reach the given p and T after isentropic expansion is also calculated in this model. The turbine inlet temperature, T_{in} , which is required for this calculation, is chosen such that it is as low as possible while staying in the vapour regime. It is critical that no liquid is formed before the expansion – this could damage the turbine. For a 50/50 CH_4/CO_2 mixture condensation can occur at temperatures below -9°C ; therefore we use a turbine inlet temperature of $T_{in} = -5^\circ\text{C}$, which is even slightly higher to ensure safe operation.

By doing these calculations for various feed compositions and a large number of pressures and temperatures, we end up with a very large data set containing x_c , x_w , r , and p_{in} as a function of the input variables p , T , T_{in} , and x_f , all in the liquid-vapour regime. Figure 3.3 outlines how the unknown variables are calculated in ACM. Further processing of the results, as is described in the following paragraphs, is done in MatlabTM; ACM is only used to generate the data set.

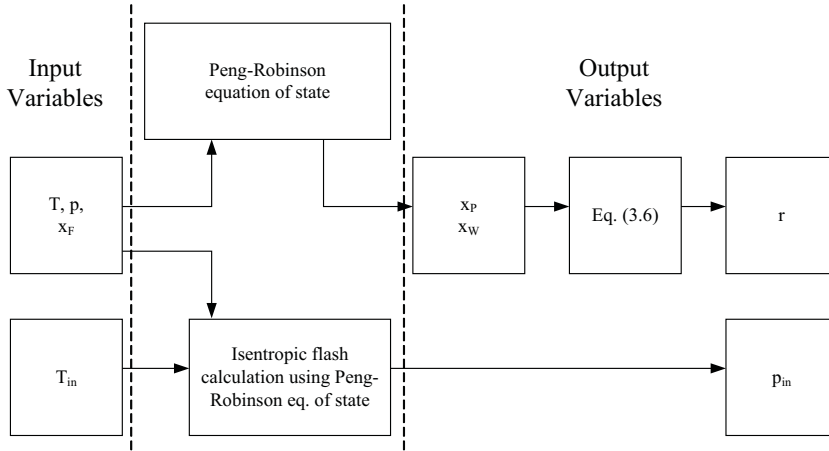


Figure 3.3. Schematic of the calculations performed in Aspen Custom ModelerTM.

For a single feed composition we can plot the values of x_c as a function r , see figure 3.4. In the left hand side of this figure all of the data is plotted for a 50/50 CH_4/CO_2 mixture, with a maximum temperature of -40°C ; higher temperatures give worse (i.e. lower x_c) results. When looking at the other data belonging to the points in this graph, it can be seen that many points require an extraordinary turbine inlet pressure of up to 2000 bar, which are not very realistic operating conditions. Therefore in the graph on the right hand side of figure 3.4 all points that require a turbine inlet pressure higher than 250 bar have been deleted. The data set has shrunk now considerably. The optimum point, i.e. with a large enrichment and recovery, is somewhere in the upper right corner in the cloud of points. Economical parameters have to be added to calculate the real optimum, i.e. that which gives the largest amount of enrichment at the lowest costs for a single gas well, whereby one could

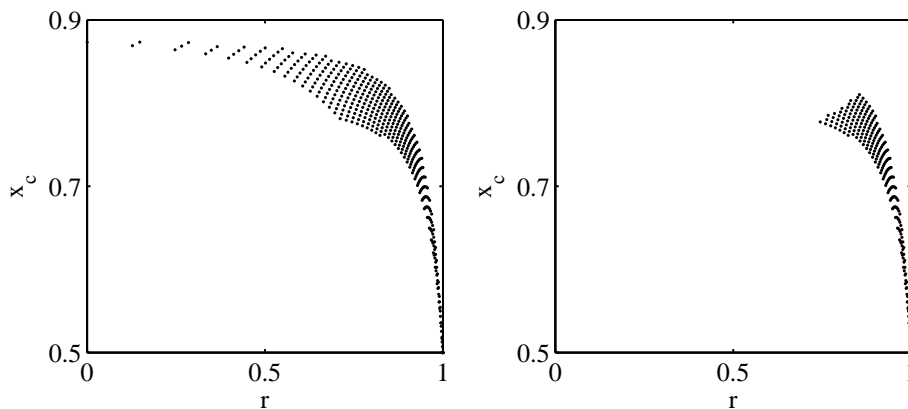


Figure 3.4. Mole fraction of CH_4 in the product stream as a function of the recovery for a 50/50 CH_4/CO_2 mixture. The right hand side graph only shows points that require a turbine inlet pressure less than 250 bar.

use multiple units of C3-sep. Such an economical study is not in the scope of this work. We can, however, plot the highest possible enrichment for a certain recovery. In figure 3.5 this is done by plotting the maximum mole fraction CH_4 in the product as a function of the mole fraction CH_4 in the feed stream for various minimal recoveries. It is noted that this is data from equilibrium calculations in the liquid-vapour regime. Calculations using the RK-Soave based model indicate that the maximum enrichment can be much larger in the solid-vapour regime.

The single-C3-sep-stage enrichment for high CO_2 content feed streams is very large; a step from $x_f = 0.3$ to $x_c \simeq 0.6$, while having a recovery of $r > 0.9$ is possible. However, for the low CO_2 content streams the enrichment is only minor; there is a limit of $x(\text{CH}_4) \sim 0.88$ above which no enrichment is possible. At least, not when requiring that the waste stream is liquid. Again, calculations using Shell software indicate that it is possible to go above $x(\text{CH}_4) \sim 0.88$, but the waste stream will then be solid.

Figure 3.6 shows the mole fraction CH_4 in the waste stream as a function of that in the feed stream. These results are complementary to the optimal results of figure 3.5. As can be seen the CH_4 content in the waste stream increases strongly as the CH_4 content in the feed stream increases. However, since this is a fully liquid stream, part of the methane can be evaporated out of the waste stream by lowering the pressure in a separate flash vessel. This methane-rich gas could then be recycled to a feed stream before the turbine. But that is an integration process that we will not focus on.

The pressures and temperatures after expansion and condensation belonging to the optimal results of figure 3.5 are plotted in figure 3.7. There are some fluctuations in these results caused by the limited resolution we use to calculate the data set; the data is sampled at 1 °C and 1 bar intervals.

Comparing these results to the phase boundary graph in figure 3.2 it is easy to see

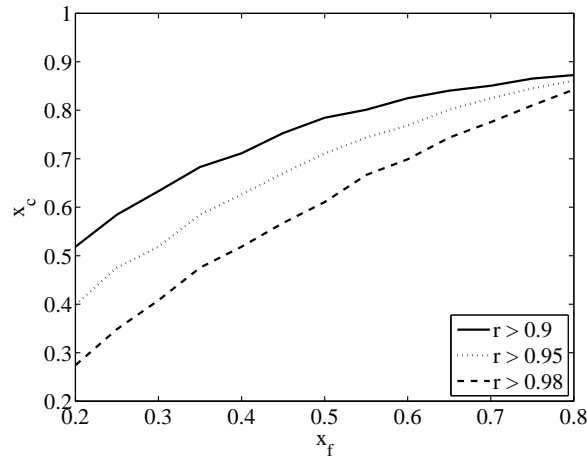


Figure 3.5. Maximum mole fraction of CH_4 in the product stream as a function of the mole fraction of CH_4 in the feed stream for various minimal recoveries.

that the temperatures and pressures are all in the vicinity of the solid boundary line. Temperatures are fairly constant, but the pressures vary almost a factor 5, making a C3-sep machine that can handle any feed composition for large scale application practically impossible; at the same residence times the required volume of the coagulation pipe and RPS will vary also almost a factor 5. A universal machine can be built but will not be very cost efficient for the lower contaminated flows, since there one can operate at higher pressure with smaller equipment. This also means that in the area where the enrichment is lower (i.e. high CH_4 content streams) the investment costs will be lower and the operational costs as well; the gas is produced at a higher pressure, resulting in lower recompression costs. However when we look at the required turbine inlet pressure, shown in figure 3.8, we see that for the higher recoveries, the inlet pressure increases with increasing methane content in the feed stream. This can add extra operational costs in the form of compression costs before the expansion. The results shown in figure 3.8 slightly fluctuate, similar to the results in figure 3.7; this is again caused by the limited resolution at which the data is sampled.

A final result of the equilibrium calculations is the weight and volume fraction of liquid in the two-phase flow entering the separator are shown in figure 3.9. The amount of liquid in the RPS is very large compared to one of the current applications of the RPS where water is removed from natural gas [34]; there liquid loading is only a few mass percent. The data presented in figure 3.9 plays an important role in the estimation of the particle sizes that will enter the separator – more on that in the following sections. Also it indicates how much liquid is to be drained from the separator and is therefore the most important parameter in the design of the separator drainage system.

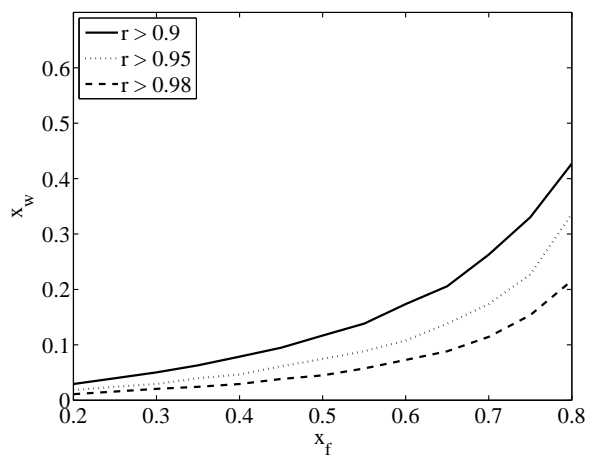


Figure 3.6. Mole fraction of CH₄ in the waste stream as a function of the mole fraction of CH₄ in the feed stream for various minimal recoveries.

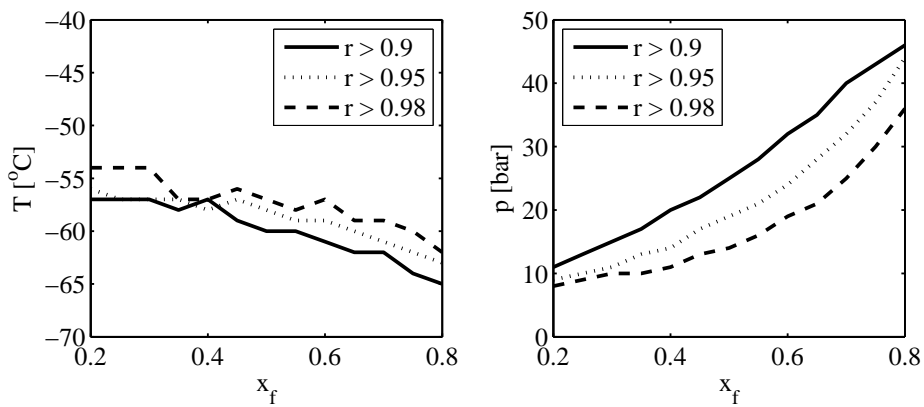


Figure 3.7. Temperature and pressure after isentropic expansion as a function of the mole fraction of CH₄ in the feed stream for various minimal recoveries.

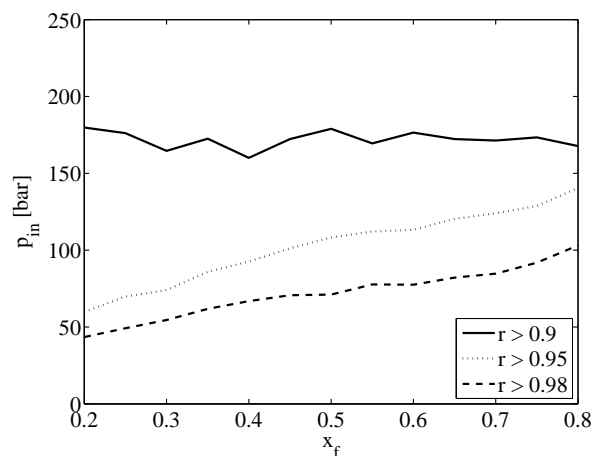


Figure 3.8. Pressure before isentropic expansion as a function of the mole fraction of CH_4 in the feed stream for various minimal recoveries.

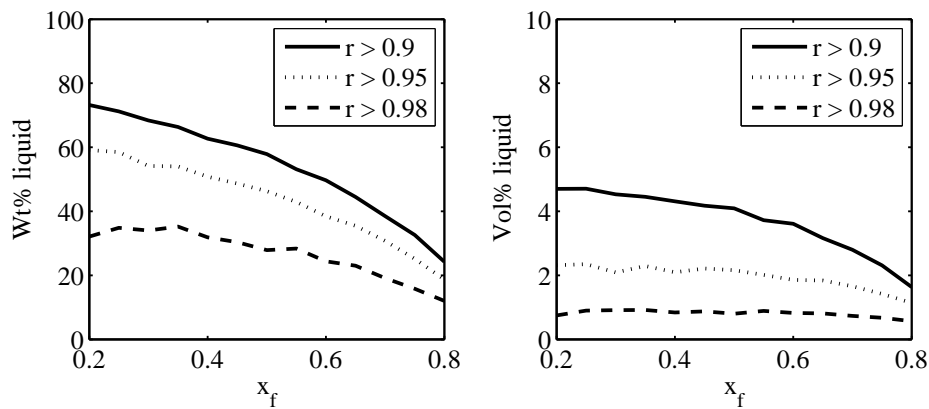


Figure 3.9. Weight% ($\text{kg}/\text{kg} \times 100\%$) and volume% ($\text{m}^3/\text{m}^3 \times 100\%$) liquid after expansion and condensation.

3.3 Equilibrium separation for carbon dioxide enrichment

In order to optimise the C3-sep process for CO₂ enrichment, the same approach can be used as for the CH₄ enrichment case; only now the liquid stream is considered to be the product stream. This is quite obvious as the liquid stream is the stream that is enriched with CO₂. To prevent confusion with the naming convention used in chapter 2 and the previous section, the liquid stream is still called "waste" stream in the current section. For a binary CH₄/CO₂ mixture, the mole fraction CO₂, y , is related to the mole fraction CH₄, x as

$$y_i = 1 - x_i, \quad (3.7)$$

where y_i is the mole fraction CO₂ in stream i . In this case we want to optimise the mole fraction CO₂ in the liquid 'waste' stream, y_w , and the recovery of CO₂ in the liquid, which is the ratio between the number of moles of CO₂ in the liquid to that in the feed stream:

$$r_{CO_2} = \frac{y_w Q_w}{y_f Q_f}, \quad (3.8)$$

which using eqs. (3.4) and (3.7) can be rewritten in a form independent of the mass streams and only dependent on the mole fractions of CH₄:

$$r_{CO_2} = \frac{(1 - x_w)(x_f - x_c)}{(1 - x_f)(x_w - x_c)}, \quad (3.9)$$

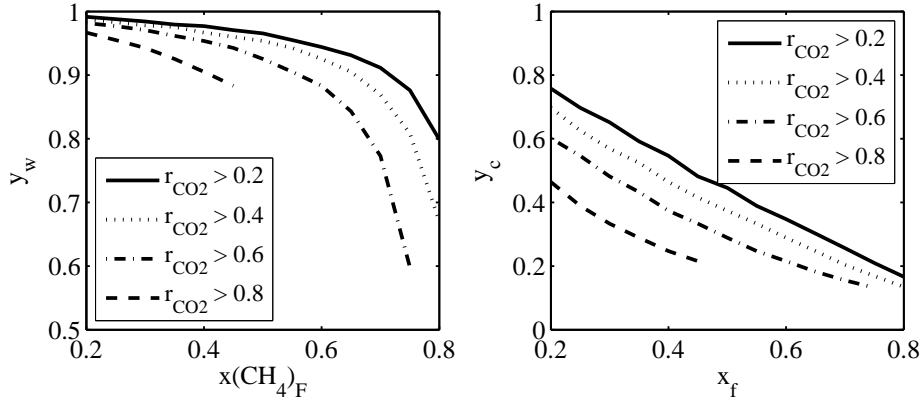


Figure 3.10. Maximum mole fraction of CH₄ in the liquid 'waste' and vapour stream as a function of the mole fraction of CH₄ in the feed stream for various minimal recoveries.

The same data set as is used for the CH₄ case is then used to generate the results depicted in figure 3.10. Here the mole fraction CO₂ in the liquid and vapour stream

are plotted as a function of the mole fraction CO_2 in the feed stream, for various minimal values of the CO_2 recovery. For low values of the CO_2 recovery and for low CH_4 content feed streams it is possible to get an almost pure CO_2 liquid stream. Looking at figure 3.11 one can see that these results are achieved at a relatively low pressure after expansion. Less expansion, i.e. a higher pressure after expansion,

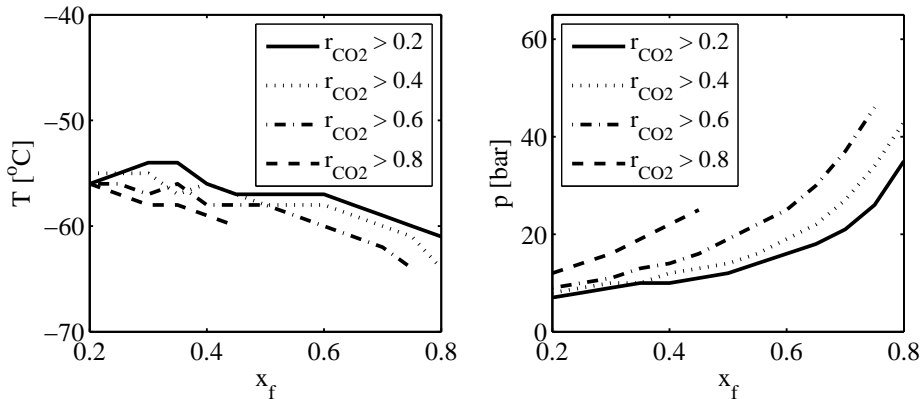


Figure 3.11. Temperature and pressure after isentropic expansion as a function of the mole fraction of CH_4 in the feed stream for various minimal recoveries. Conditions are complementary to the results in fig. 3.10.

results in more CO_2 condensing but also in more CH_4 dissolving in the CO_2 liquid, which then results in a higher recovery of CO_2 in the liquid stream but also in lower purity. The recovery of CO_2 in the liquid is only limited as can be seen by the abrupt end of some of the lines plotted in the results; recoveries of $r_{\text{CO}_2} > 0.6$ and $r_{\text{CO}_2} > 0.8$ are not possible for feed streams with $x_f > 0.75$ and $x_f > 0.45$ respectively, at least not without creating solids. Recoveries of $r_{\text{CO}_2} > 0.9$ are not possible for any of the evaluated feed streams. As stated earlier, data points in the data set are limited by a maximum allowed turbine inlet pressure of 250 bar. This limitation is also a reason that $r_{\text{CO}_2} < 0.9$ for the whole data range as can be seen in figure 3.12; for higher recoveries and lower CO_2 content feed streams a higher turbine inlet pressure is required. This in turn can be explained by looking at figure 3.11; temperatures are all near the solid boundary, as was also the case for CH_4 enrichment, but pressures increase with increasing recovery and increasing CH_4 content in the feed stream. To reach a temperature of approximately $T \sim -60^\circ\text{C}$ at increasing pressures, also increasing turbine inlet pressures are required, given that the turbine inlet temperature stays the same.

The weight and volume fractions of liquid are shown in figure 3.13. Both show a strong increase with increasing recovery of CO_2 , which is as expected; more recovery simply means that more CO_2 is condensed. The liquid loading can be even higher than in the CH_4 enrichment case: up to more than 75 weight% and 5.5 volume% liquid can enter the separator.

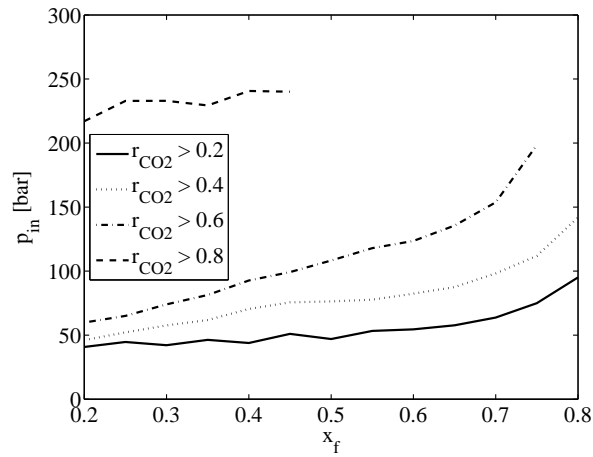


Figure 3.12. Pressure before isentropic expansion as a function of the mole fraction of CH_4 in the feed stream for various minimal recoveries.

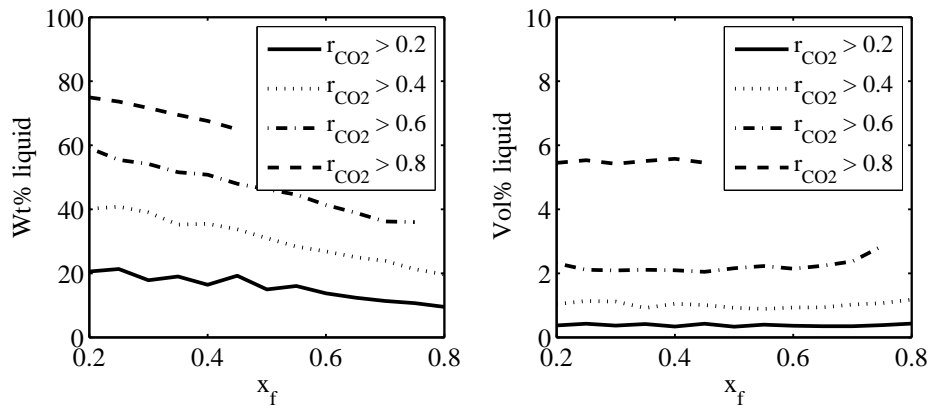


Figure 3.13. Weight% ($kg/kg \times 100\%$) and volume% ($m^3/m^3 \times 100\%$) liquid after expansion and condensation for the CO_2 enrichment case.

3.4 The influence of the presence of H₂S on equilibrium separation

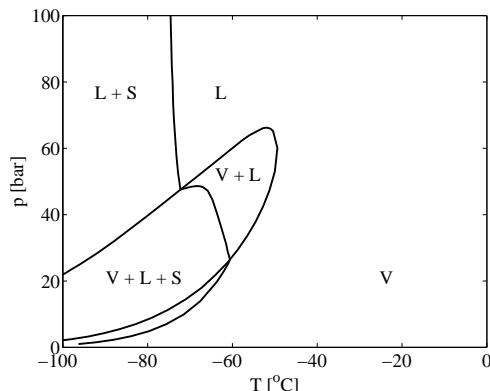


Figure 3.14. Phase diagram of a 80/20 CH₄/CO₂ mixture. Vapour is indicated with V, liquid is indicated with L, and solid CO₂ is indicated by S.

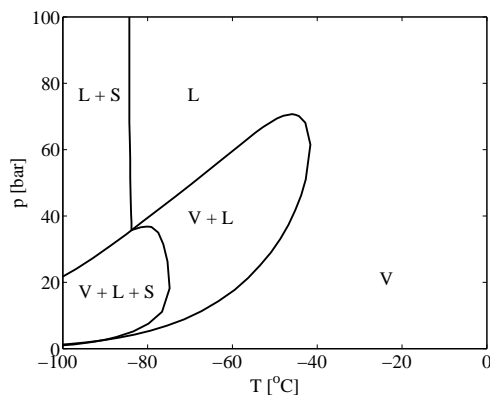


Figure 3.15. Phase diagram of a 80/14/6 CH₄/CO₂/H₂S mixture. Vapour is indicated with V, liquid is indicated with L, and solid is indicated by S.

The phase diagrams of three 80 % methane systems are shown in figures 3.14, 3.15, and 3.16; they all contain 20 % CO₂ or H₂S. It is easy to see that the 80/20 CH₄/CO₂ has a relatively small vapour-liquid region, and that this vapour-liquid region increases in size with increasing H₂S content. This has two reasons: the maximum temperature at which liquid can be formed increases, and the solid boundary shifts to the left, i.e. towards lower temperatures.

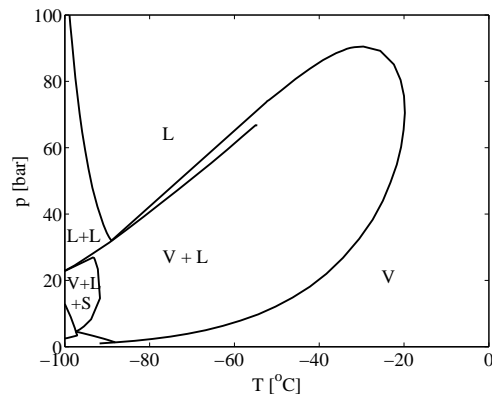


Figure 3.16. Phase diagram of a 80/5/15 CH₄/CO₂/H₂S mixture. Vapour is indicated with V, liquid is indicated with L, and solid is indicated by S.

For separation in a C3-sep system, this means that the operational regime, in terms of thermodynamics becomes larger; it is possible to operate at lower temperatures with H₂S present in the system. This in turn means that we can expect better separation performance with H₂S in the system, as the optimal thermodynamic conditions of CH₄/CO₂ separation are all in the vicinity of the solid boundary, i.e. the lowest temperature possible in practice with a C3-sep system.

To see whether this statement is true, data sets containing x_c , x_w , r , and p_{in} as a function of p , T , T_{in} , and x_f are calculated for the gas compositions presented in figures 3.14, 3.15, and 3.16, in a similar way as is done in section 3.2. The system of 80/14/6 CH₄/CO₂/H₂S complies to the gas composition present in the field Harweel in Oman, and the system 80/5/15 CH₄/CO₂/H₂S complies to the gas composition present in the field in Kashagan, Kazakhstan. Again, the maximum mole fraction of methane in the product (gas) stream, x_c , is calculated as a function of the recovery, r . The results are shown in tables 3.1, 3.2, and 3.3.

$r \geq 0.9$	max. x_c	T (°C)	p (bar)	p_{in} (bar)
80/20 CH ₄ /CO ₂	0.87	-65	46	168
80/14/6 CH ₄ /CO ₂ /H ₂ S	0.91	-73	31	144
80/5/15 CH ₄ /CO ₂ /H ₂ S	0.96	-89	21	173

Table 3.1. Maximum mole fraction of methane in the product stream, x_c , for $r \geq 0.9$. Results are shown for 80 mole% methane systems with 0, 6, or 15 mole% H₂S content.

As can be seen, the optimal pressures and temperatures after expansion are lower with H₂S present than without, while the required turbine inlet pressures are pretty similar. More importantly, the mole fraction CH₄ in the product stream, x_c , is higher

$r \geq 0.95$	max. x_c	T (°C)	p (bar)	p_{in} (bar)
80/20 CH ₄ /CO ₂	0.86	-63	44	141
80/14/6 CH ₄ /CO ₂ /H ₂ S	0.89	-73	25	112
80/5/15 CH ₄ /CO ₂ /H ₂ S	0.96	-89	17	138

Table 3.2. Maximum mole fraction of methane in the product stream, x_c , for $r \geq 0.95$. Results are shown for 80 mole% methane systems with 0, 6, or 15 mole% H₂S content.

$r \geq 0.98$	max. x_c	T (°C)	p (bar)	p_{in} (bar)
80/20 CH ₄ /CO ₂	0.84	-62	36	103
80/14/6 CH ₄ /CO ₂ /H ₂ S	0.86	-73	17	74
80/5/15 CH ₄ /CO ₂ /H ₂ S	0.94	-87	11	98

Table 3.3. Maximum mole fraction of methane in the product stream, x_c , for $r \geq 0.98$. Results are shown for 80 mole% methane systems with 0, 6, or 15 mole% H₂S content.

when H₂S is present in the feed mixture. Normally, when no H₂S is present, it is difficult for a feed stream containing 80 % CH₄ to get above 88 % CH₄ in the product stream while staying in the liquid regime, see section 3.2. But when H₂S is present in the system then the CH₄ content in the product stream can be as large as 96 %; large enough to economically remove the remaining contaminants with conventional technology. For the real-life implementation of C3-sep it is thus best to initially focus on the H₂S rich gas fields, as they are the easiest to enrich to high purity CH₄. Contaminated gas fields without H₂S present will require at least one C3-sep step where solid formation will occur. The drawback of H₂S in the system is that it poses a much higher hazard, since H₂S is very poisonous. Therefore in the prototype development we still only focus on CH₄/CO₂ enrichment – a proof of concept is more important at this stage.

3.5 Droplet formation and growth

As the contaminated natural gas is expanded in the turbine, it cools down. At a certain point during this cooling process the saturation pressure becomes, due to the lower temperatures, lower than the partial vapour pressure of the contaminants. When this happens part of the gas starts to condense. In the C3-sep process there are two main condensation processes. Condensable matter can form new droplets or so-called nuclei, which is the homogeneous nucleation process, or the condensable matter diffuses to and condenses on existing droplets or particles, which is heterogeneous condensation. Matter can also diffuse to and condense on the walls of the equipment, but since the walls are in this process warmer than the gas –the gas is cooled by expansion, not by the walls!– and because the specific area of the walls is small compared to that of the existing particles, the influence of this process can be neglected. So by expanding the gas in a turbine bulk condensation occurs as opposed to wall condensation which is the process that dominates condensation in for instance refrigerators and condensers.

Next to droplet formation and growth there is a third process that influences the size of the droplets; when droplets collide they can form a new larger droplet, i.e. the numbers of droplets decreases while their size increases. This process is called coagulation and it is not a condensation process; it is fully determined by the chance that droplets collide.

Thus, in total there are three processes which determine the size of the droplets that are formed by the bulk condensation process:

- Homogeneous nucleation
- Heterogeneous condensation
- Coagulation

In the next sections the governing equations, according to theory, for homogeneous and heterogeneous condensation will be stated, as well as that for monodisperse coagulation theory. The latter is a simplification of the real situation: it assumes that all particles have the same size. In reality there will be some sort of particle size distribution. When the equations for the three processes are coupled to energy, momentum, and mass balance equations, they can be solved to get an estimate on the size of the particles and the number of particles that can be expected after expansion and condensation.

However, from literature [31] it follows that for natural gas under 'high' pressure, i.e. a similar pressure to what we have after expansion, the estimates that result from theory are highly inaccurate when compared to measurements with real natural gas experiments. In fact, we calculated such estimates, using the theory from literature, and found them to be very sensitive to the values of physical parameters such as the surface tension and to the rate and way the expansion takes place. Since a real natural gas stream contains traces of higher hydrocarbons, the actual value of for instance the surface tension is not known with great accuracy; an error of a few percent in this value can result in an uncertainty of the eventual number of particles estimate of

one order of magnitude [22]. The rate and way of expansion can result in an error of several orders of magnitude.

Therefore we will not estimate the particle size and number of particles using the coupled solution of all equations, but instead we produce a worst case estimate using an engineering approach. This worst case estimate gives us the limits within which we can expect the size of the droplets will be. Such limits enable us to design a separator to collect the droplets, which is also the goal of this droplet formation study. In follow up PhD thesis projects experiments will be performed to measure the particle size distribution. These measurements can then be used to determine the influence of process parameters on the particle size distribution.

The limits within which the actual droplet diameter can be found depend on which condensation process is dominant. There are two scenarios possible:

1. Homogeneous nucleation is the fastest process: Homogeneous nucleation is a nuclei formation process. If it is the dominant process, then the number of droplets will be very large. There is only a fixed volume of liquid, so this results in very small droplets. These droplets must then grow by coagulation in order to be able to separate them. The size of the droplets depends on the time in which coagulation takes place.
2. Heterogeneous condensation is the fastest process: In that case, as soon as a limited number of droplets is formed (by homogeneous nucleation) all condensible matter diffuses and condenses on these droplets. This results in a limited number of relatively large droplets. The size of the droplets depends on the ratio between the homogeneous and heterogeneous condensation rate.

So the worst case is when homogeneous nucleation is dominant; this will lead to the smallest droplets, which are the most difficult to collect. In order to estimate which process will be the fastest, each process is separately evaluated to acquire insight in their timescales.

3.5.1 Thermodynamic conditions

The results presented in the following sections apply to the conditions present in the laboratory C3-sep unit that will be discussed in chapter 5. Here a stream that contains 50 mole% CH₄ and 50 mole% CO₂ is compressed and cooled to a pressure of 150 bar and a temperature of -5 °C. This stream is expanded in a Joule-Thompson valve – a turbine is unavailable as will be explained in chapter 5 – to a pressure of 27 bar and a temperature of -48 °C. In case a turbine would be used, then the resulting temperature after expansion would be -55 °C. After expansion in the Joule-Thompson valve, part of the gas condenses and the remaining gas contains 68 mole% CH₄ (or 75 mole% in case a turbine is used). Optimisation of these thermodynamic conditions is done in Aspen PlusTM and Aspen Custom ModelerTM, using the same procedure as discussed earlier in this chapter. The only difference is that the compressor is now limited to a pressure of 150 bar.

3.5.2 Homogeneous nucleation

A gas with a pressure higher than the saturation pressure is called a supersaturated gas. The degree of supersaturation is indicated by the supersaturation ratio:

$$S = \frac{p}{p_{sat}} \quad (3.10)$$

where p_{sat} is the saturation pressure (bar). In a supersaturated gas molecules constantly collide and form clusters. The smallest clusters will evaporate again but if a cluster has a certain critical size it becomes a stable nucleus which will grow. This critical cluster diameter follows from the Classical Nucleation Theory (CNT) and is expressed by the Kelvin relation [22]:

$$d_p^* = \frac{\sigma v_m}{kT \ln S}, \quad (3.11)$$

where σ is the surface tension (N/m), v_m the volume of a molecule (m^3), and k Boltzmann's constant ($1.381 \cdot 10^{-23}$ J/K). It can be seen that the critical diameter is dependent on the supersaturation ratio. The rate at which these nuclei are formed is also strongly dependent on the supersaturation ratio; according to the CNT this rate, also called the droplet current, I (nuclei/ m^3s), is expressed as [22]:

$$I = 2 \left[\frac{p_i}{(2\pi m_i kT)^{1/2}} \right] \left(n_i v_m^{2/3} \right) \left[\frac{\sigma v_m^{2/3}}{kT} \right]^{1/2} \exp \left[-\frac{16\pi\sigma^3 v_m^2}{3(kT)^3 (\ln S)^2} \right], \quad (3.12)$$

where p_i is the partial pressure (Pa), m_i the molecular mass (kg), and n_i the molecular density (molecules/ m^3) of the condensable component.

By substituting the ideal gas law in this equation and subsequently rewriting it, we end up with a more compact equation:

$$I = \sqrt{2} v_m \left(\frac{\sigma}{\pi m_i} \right)^{1/2} n_i^2 \exp \left[-\frac{16\pi\sigma^3 v_m^2}{3(kT)^3 (\ln S)^2} \right], \quad (3.13)$$

which expresses the droplet current I as a function of the molecular density n_i , the supersaturation ratio S , the temperature T , and a number of material properties. These material properties are not or only weakly dependent on temperature over the range of temperatures we are interested in; they can thus be considered to be constant. The temperature has only a small influence on the outcome of eq. (3.13). If we set the temperature to the equilibrium temperature after expansion, i.e. -48 °C, the maximum error in the calculated value of I , due to this effect only, is ca. 30 %. This might seem a large error, but a small change in the value of S (i.e. $S = 1.3$ instead of $S = 1.5$) leads to several orders of magnitude difference. The benefit of fixing the temperature to a constant value is that we do not have to solve the energy and momentum equations in order to simulate the expansion process. With a fixed value of T we can analytically solve eq. (3.13) and we see directly the influence of the supersaturation ratio on the homogeneous nucleation rate, i.e. the droplet current.

Before we can do that we have to couple eq. (3.13) to a mass balance. If we evaluate eq. (3.13) for a fixed value of S , then the molecular density n_i is equal to the

molecular density at time zero minus the molecules that have condensed into newly formed droplets:

$$n_i = n_{i0} - k^* N, \quad (3.14)$$

where n_{i0} is the molecular density (molecules/m³) at $t = 0$, N the number of nuclei, and k^* the number of molecules in a nucleus:

$$k^* = \pi/6 (d_p^*)^3 / v_m. \quad (3.15)$$

Substitution of eq. (3.14) and $I = dN/dt$ in eq. (3.13) leads to:

$$\frac{dN}{dt} = C_1 (n_{i0} - k^* N)^2 \exp \left[\frac{-C_2}{(\ln S)^2} \right], \quad (3.16)$$

where $C_1 = \sqrt{2} v_m (\sigma / (\pi m_i))^{1/2}$, and $C_2 = (16 \pi \sigma^3 v_m^2) / (3 (kT)^3)$ are constants if we assume that the temperature is constant.

Integration of eq. (3.16) for a fixed value of S gives:

$$N = \frac{n_{i0}}{k^*} \left(1 + \left(n_{i0} k^* C_1 \exp \left[\frac{-C_2}{(\ln S)^2} \right] t \right)^{-1} \right)^{-1} \quad (3.17)$$

Eq. (3.17) is dependent on the supersaturation ratio, which in turn is dependent on the expansion rate. If the expansion would take place instantaneously, then for the thermodynamic conditions encountered in the laboratory C3-sep unit, i.e. a 50/50 CH₄/CO₂ mixture expanded to $p = 27$ bar, one would have a supersaturation ratio of $S = 2.1$. A slower expansion results in particle formation during expansion, which means that this maximum supersaturation ratio of $S = 2.1$ can not be reached, since part of the gas has already condensed as the pressure reaches its lowest point. It is thus possible to control the supersaturation ratio by controlling the expansion rate. In figure 3.17 the particle number concentration as a function of time, calculated with eq. (3.17), is plotted for various values of the supersaturation ratio.

The results in figure 3.17 are divided by the maximum possible particle number concentration, $N_{max} = n_{i0}/k^*$, which is dependent on the number of molecules in a nucleus. From eqs. (3.15) and (3.11) it can be seen that this is also dependent on the supersaturation ratio. For a larger supersaturation ratio the formed droplets will be smaller, resulting in a higher possible maximum particle number concentration for a certain gas density. At this point we are only interested in the speed of the homogeneous nucleation process for application in C3-sep, so we normalised the results; the maximum particle number concentration is in the range of $N_{max} \sim 10^{24} \dots 10^{26} \text{ m}^{-3}$.

The time within which homogeneous nucleation takes place in the C3-sep conditions is very short. Even for $S = 1.3$ the number of particles formed within 1 ms is more than $N = 10^{20}$. Why this process is so fast can be explained by looking at eq. (3.12). Not only is this equation dependent on the supersaturation ratio and material properties, but also on the partial pressure of condensable matter, p_i , and the number of condensable molecules, n_i , which in turn is related to partial pressure, thus $I \sim p_i^2$. For processes where the partial pressure of condensable matter is low,

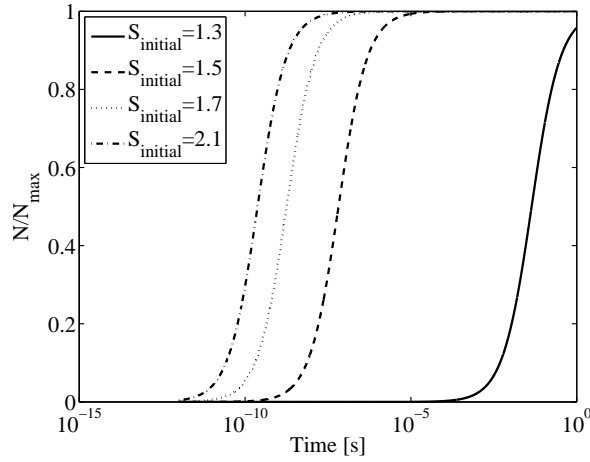


Figure 3.17. N/N_{max} as a function of time for various maximum values of the supersaturation ratio, S . Calculated using the equation for homogeneous nucleation rate and a mass balance; heterogeneous condensation is omitted.

such as aerosol formation, this means that the nucleation rate can only be high if the supersaturation ratio is very large, i.e. the saturation pressure is very low. But for the C3-sep process where the partial pressure is of the same order as the total pressure, and thus thousands times larger than in aerosol formation, it results in the nucleation rate being very large even for low to moderate values of S , such as $S = 2.1$ in this case. Thus homogeneous nucleation, and also condensation, will be very fast in case of the C3-sep process.

3.5.3 Heterogeneous condensation

The second condensation process that plays an important role in C3-sep is heterogeneous condensation. Here molecules condense on existing particles, or droplets, and the rate at which they condense is limited by diffusion; in order to condense on the particles they have to reach them first. Since heterogeneous condensation is a process depending on diffusivity one might think that, as in the gas of gas centrifugation (see chapter 2), this is a very slow process. However, it is not, as we will see in the following paragraphs. The reason it is fast is that the surface area to which the molecules have to diffuse is huge, due to the large amount of tiny droplets that are present due to the fast homogeneous nucleation process. These tiny droplets, nuclei, have a very large specific surface area ($A/V \sim 1/r!$) which multiplied by their number density, N , results in a very large specific surface area for the whole diffusion process.

The mass transfer of condensing gas to a single droplet, \dot{m} (kmol/s) is equal to [8]:

$$\dot{m} = -4\pi r_d \rho_d D \ln \left(\frac{1 - x_\infty}{1 - x_s} \right), \quad (3.18)$$

where r_d is the radius of the droplet (m), ρ_d the molar density of the droplet (kmol/m³), D the diffusion coefficient (m²/s), x_∞ the mole fraction of the condensible gas in the bulk, and x_s the mole fraction of the condensible gas at saturation pressure. Assuming that all droplets in a certain volume have the same size and that the number density of these droplets, N (droplets/m³), is known, then the change of molar density of the condensible gas, ρ_∞ (kmol/m³) per unit time can be expressed as:

$$\frac{d\rho_\infty}{dt} = \dot{m}N. \quad (3.19)$$

Substituting eq. (3.18) in eq. (3.19) results in:

$$\frac{d\rho_\infty}{dt} = -4\pi r_d \rho_d D N \ln \left(\frac{1 - x_\infty}{1 - x_s} \right). \quad (3.20)$$

The maximum radius, R_d (m) a droplet under these conditions can reach is that where all the gas condenses, i.e. $x_s = 0$. This radius is equal to:

$$R_d = \left(\frac{3\rho_{\infty 0}}{4\rho_d \pi N} \right)^{\frac{1}{3}}, \quad (3.21)$$

where $\rho_{\infty 0}$ is the molar density of condensible gas at the time of the start of the condensation, $t = 0$. The value of the maximum radius as a function of the particle number concentration for the C3-sep experimental conditions is shown in figure 3.18.

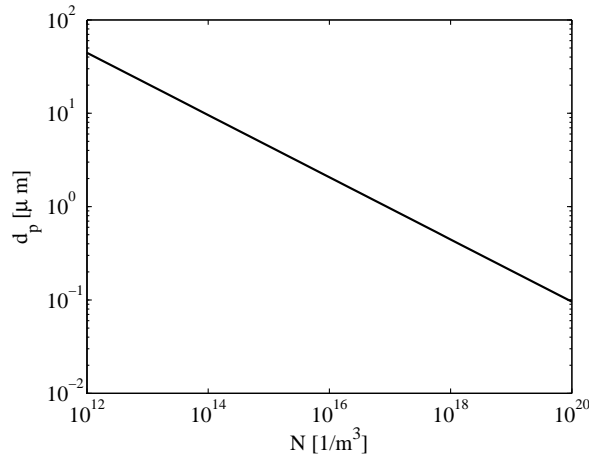


Figure 3.18. Droplet size as a function of number density for the experimental C3-sep conditions.

Using the defined maximum radius we can introduce a dimensionless droplet radius:

$$y = \frac{r_d}{R_d}, \quad (3.22)$$

and also a dimensionless time:

$$\tau_{Diff} = t4\pi ND_0R, \quad (3.23)$$

where D_0 is the diffusion coefficient at $t = 0$. The diffusion coefficient varies in time due to the fact that, in an expansion process, the pressure varies in time; the product pD and thus also ρD is relatively constant, see chapter 2. A reference diffusion coefficient is used as scaling parameter. The corresponding density, the total vapour density at $t = 0$, $\rho_{vapour0}$, is used to introduce a dimensionless partial vapour density:

$$\chi = \frac{\rho_\infty}{\rho_{vapour0}} \quad (3.24)$$

Substituting eqs. (3.10), (3.22), (3.23), and (3.24) into eq. (3.20) gives an equation for the dimensionless partial vapour density as a function of the supersaturation ratio, S , and the dimensionless droplet radius:

$$\frac{d\chi}{d\tau_{Diff}} = -y \ln \left(\frac{1 - x_\infty}{1 - x_\infty/S} \right). \quad (3.25)$$

The dimensionless partial vapour density and droplet radius are coupled due to mass conservation; the mass flux to a droplet leads to a droplet growth calculated by:

$$\dot{m} = \frac{4}{3}\pi\rho_d \frac{dr_d^3}{dt}, \quad (3.26)$$

which by substitution of the above equations, together with the fact that $\rho_{\infty0}/\rho_{vapour0} = x_{\infty0}$ leads to a second differential equation that links the dimensionless partial vapour density and droplet radius:

$$\frac{d\chi}{d\tau_{Diff}} = -3x_{\infty0}y^2 \frac{dy}{d\tau_{Diff}}. \quad (3.27)$$

We now have two differential equations (eqs. (3.25) and (3.27)) that have to be solved simultaneously to estimate the heterogeneous condensation time. For these calculations we again neglect the energy and momentum balance calculations by setting the supersaturation ratio to a constant value. In a numerical model eqs. (3.25) and (3.27) are coupled to a mass balance stating that the rate of change of vapour mass is equal to the rate at which mass condenses. Using this model we calculate the time that heterogeneous condensation requires to condense 99 % of the condensable matter as a function of the number of nuclei, N and the supersaturation ratio, S . This estimate can then be compared to the estimate that is made for homogeneous nucleation. In figure 3.19 this is depicted by plotting this time as a function of the (fixed) number of nuclei for various maximal supersaturation ratios for the C3-sep process of single-stage enrichment of a 50/50 CH_4/CO_2 mixture.

From figure 3.19 it can be seen that for high nuclei number densities the heterogeneous condensation process is very fast; condensation takes place in less than milliseconds for $N > 10^{12}$ nuclei/m³ or even in less than microseconds for $N > 10^{18}$

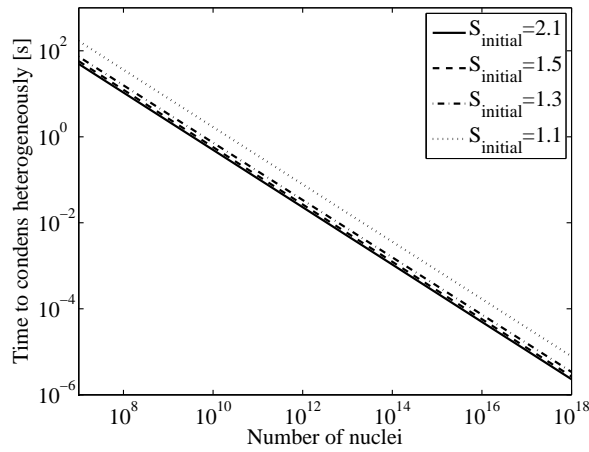


Figure 3.19. Condensation time as a function of number of nuclei for various maximum values of the supersaturation ratio, S . Calculated using a diffusion equation and a mass balance; homogeneous nucleation is omitted, number of nuclei is fixed during a single calculation.

nuclei/m³. This is as expected, since more nuclei or droplets means that diffusion area increases, since the specific surface area for small objects is larger than for large objects. The actual value of the maximum supersaturation ratio has not much influence on the time to condense in these calculations performed for the C3-sep process, as can be seen by looking at figure 3.19.

So far we have seen that both condensation processes are very fast, which means that condensation time is not an issue when designing a C3-sep setup. The residence times between the separate stages, i.e. expansion and separation, will be more than 0.1 s. due to the physical size of the devices and their supporting equipment. Expansion and condensation will be faster than that. If the expansion process would be infinitely fast, i.e. $S \sim 2.1$, then the condensation process would take less than 1 μ s due to homogeneous nucleation. On the other hand, if the expansion process would take 0.1 s, which is slow (turbines have expansion times of 1–10 ms), then the bulk of the condensation takes also place within approximately 0.1 s, regardless of what heterogeneous condensation does.

This can be explained as followed: if there would be a considerable amount of uncondensed matter after the expansion, then the supersaturation ratio would still be considerably larger than 1 (e.g. $S > 1.3$, see figure 3.17). At $S = 1.3$ (or even $S = 1.1$ which is not depicted in the graphs) homogeneous nucleation still takes place within a very short time. The only way to prevent homogeneous nucleation is by very slowly expanding the gas, preventing the supersaturation ratio from becoming slightly larger than 1. This would also slow down heterogeneous condensation as there are no droplets formed to condense onto. So it is safe to say that condensation takes place in approximately the same time as the expansion process.

In order to design a separator to separate the condensed droplets from the gas,

we need to know the size of the droplets that are formed by condensation. If thermal equilibrium is reached then the amount of liquid is known and the approximate size of the droplets is only dependent on how much droplets there are. This could be calculated by coupling homogeneous and heterogeneous condensation theory with mass and energy balances and solving the system of equations to end up with the particle size distribution. As stated earlier, for natural gas under high pressure, this type of calculations has been compared to experimental data in the past [31]. The conclusion of this research was that the number density predictions could be off by a factor 10^5 . From this we can conclude that for each separate case experimental data is required.

From a designers perspective it is not important to know the particle size distribution, one only needs to know how small the droplets will be in the worst case. That is the droplet size that the separator has to be designed for. If we turn this statement around, we can also say that the droplets have to be at least in the micron range in order to be able to separate them with an industrial sized RPS. From figure 3.18 it can be seen that the number density must be maximally $N \sim 10^{17} \text{ 1/m}^3$ for the droplets to be larger than $1 \text{ }\mu\text{m}$.

By considering typical expansion times (1 to 10 ms) and by looking at figure 3.19 we can say that the number density is at least $N > 10^{12}$. A lower number density would mean that the heterogeneous condensation is much slower than the expansion resulting in a high supersaturation ratio, and thus high homogeneous nucleation rate, after expansion, which again results in a higher number density; i.e. a lower number density is impossible. The size of the droplets is in this case almost large enough to separate them with a conventional cyclone. This is the result if heterogeneous condensation dominates the condensation process. If homogenous nucleation dominates the condensation process than the maximum number density, and thus the minimal droplet size, is only limited by the maximum supersaturation ratio. As we saw above, this can lead to a number density as large as $N \sim 10^{24}$. Figure 3.18 shows that the droplet size will in that case be much smaller than $d_p < 10^{-7} \text{ m}$, which is too small to be collected in the RPS.

It can be concluded that condensation will take place within reasonable residence time, but can lead to high number densities and thus droplets that are too small to be separated. Luckily there is a process that leads to a decrease in number density and thus increase in droplet size, this process is coagulation and will be discussed in the next section.

3.5.4 Monodisperse coagulation

In this section the time is calculated to coagulate small sized droplets with a high number density ($N > 10^{17} \text{ 1/m}^3$) to droplets with a size that can be separated in a RPS, i.e. $d_p > 1\mu\text{m}$. This will be done by evaluating monodisperse coagulation theory. In reality the mixture will be polydisperse, but monodisperse theory is accurate enough to calculate this estimate.

The rate of change of number concentration which occurs in a monodisperse mixture, i.e. a mixture with a single droplet size, due to diffusion and collision of droplets

can be calculated by [28]:

$$\frac{dN}{dt} = -KN^2, \quad (3.28)$$

where K (m^3/s) is the coagulation coefficient:

$$K = 4\pi d_p D_p, \quad (3.29)$$

where D_p is the particle diffusion coefficient [28]. Using the Stokes-Einstein equation for the aerosol particle diffusion coefficient,

$$D_p = \frac{kTC_c}{3\pi\eta d_p}, \quad (3.30)$$

it is possible to express the coagulation coefficient in a form (partially) independent of the droplet diameter:

$$K = \frac{4kTC_c}{3\eta}, \quad (3.31)$$

where k is Boltzmann's constant and C_c is the Cunningham correction factor [28]:

$$C_c = 1 + \frac{\lambda}{d_p} \left[2.514 + 0.800 \exp \left(-0.55 \frac{d_p}{\lambda} \right) \right] \quad (3.32)$$

where λ is the mean free path of the carrier gas. The coagulation coefficient is only dependent on the droplet diameter via the Cunningham correction factor. This is a correction for the fact that very small particles ($d_p < \lambda$) do not comply to the so-called no-slip condition and therefore experience less resistance when travelling through a gas. For the C3-sep application of $\text{CH}_4/\text{CO}_2/\text{H}_2\text{S}$ separation the Cunningham correction factor is $C_c \sim 1$ for particles as small as $d_p > 10^{-7}$ m, due to the fact that the mean free path of the gas is very short in this cold, high pressure C3-sep application. The coagulation coefficient is for this application: $K \simeq 3.65 \cdot 10^{-16}$ m^3/s for $d_p > 10^{-7}$ m. Smaller particles have a larger coagulation coefficient due to the larger Cunningham correction factor; this results in faster coagulation for these particles. The coagulation coefficient of the C3-sep process is only slightly higher than that for air at ambient conditions: $K_{air} \simeq 3.0 \cdot 10^{-16}$ m^3/s [28]. Numerical integration of eq. (3.28) gives the decrease of the particle number concentration, N , due to monodisperse coagulation as a function of time, see figure 3.20. By looking at figures 3.17 and 3.19 it is easy to see that compared to the nucleation processes, the coagulation process is rather slow. With a sufficiently high supersaturation ratio it is possible to create a very high number concentration within milliseconds, but it will take seconds to coagulate to moderate number concentrations ($N \sim 10^{13}$ m^{-3} [28]). By coupling eq. (3.28) to a mass balance, it is easy to calculate the droplet diameter as a function of time for a monodisperse coagulation process, see figures 3.21 and 3.22. Here the droplet diameter is plotted as a function of time, for various volume fractions of liquid or for various gas field compositions. The top line in figure 3.21 corresponds

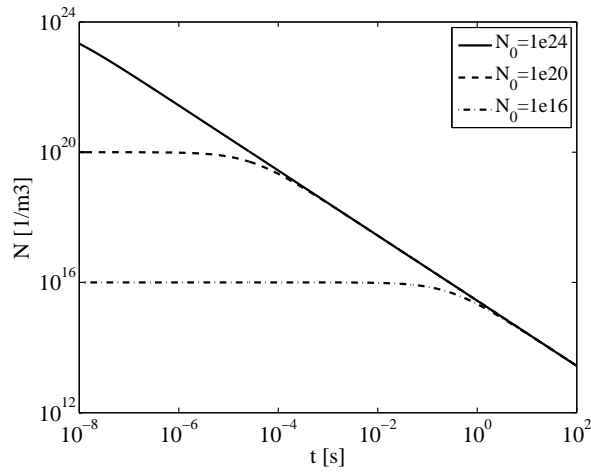


Figure 3.20. Particle number concentration as a function of time for various initial particle number concentrations.

to the volume fractions liquid that are encountered in C3-sep applications: vol% liquid $\sim 5\%$. From this line we can conclude that in the worst case of nucleation possible for the C3-sep process, i.e. that where we have a huge amount of tiny particles, $N > 10^{20} \text{ m}^{-3}$, coagulation will lead to particles larger than one micron in typically 0.1 s. In terms of residence times this is very short, making the C3-sep process suitable for large scale natural gas processing applications.

On other end of the volume fractions liquid scale; that corresponding to vol% liquid $\sim 5 \cdot 10^{-6}\%$, we find the results for coagulation as is encountered in aerosol formation processes, for instance in biomass combustion processes. Here particles will not reach micron size within hours, again assuming that one has a huge amount of particles after nucleation ($N > 10^{20} \text{ m}^{-3}$). Such particles can therefore not be collected by a RPS, unless the amount of particles formed by homogeneous nucleation can be controlled.

In view of the experimental setup that is to be designed and build it is safe to say that 0.1 s. coagulation time should be enough to be sure to have droplets that can be collected by a RPS, i.e. $d_p > 1 \mu\text{m}$. For a more safe operation regime it is desirable to have droplets larger than $d_p > 5 \mu\text{m}$. In that case a residence time of several seconds is required. To validate all this data and conclusions, the experimental C3-sep system should have a variable residence time between expansion and separator, to vary the coagulation time, and it should also incorporate a particle size measurement system.

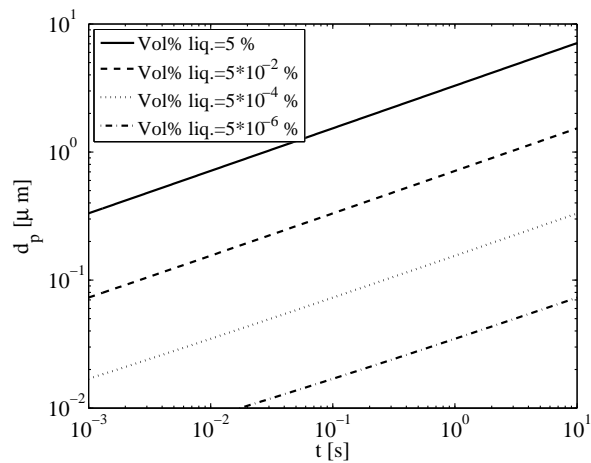


Figure 3.21. Droplet diameter as a function of time for various volume fractions of liquid. Calculated using monodisperse coagulation theory.

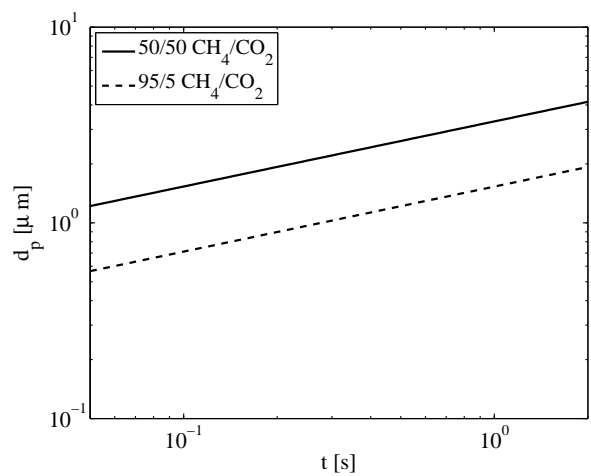


Figure 3.22. Droplet diameter as a function of time for various field compositions. Calculated using monodisperse coagulation theory.

Chapter 4

In-line centrifugal separation of dispersed phases*

4.1 Introduction

Separation of liquid dispersions from another fluid is one of the most important unit operations in the oil and gas business [38, 29]. The dispersions are either oil/water or liquid/gas mixtures. The latter category has until now mainly been concerned with removal of water droplets and light hydrocarbon liquids from gas streams. A new area is where ultra fine CO₂ rich mists are created by expansion. This is a novel method which removes natural gas contaminants by condensation and enables access to gas reserves where the CO₂ or H₂S content is too high to be removed by traditional amine methods [17].

Cyclones are standard for liquid/gas separation in hydrocarbon processing plants. However these are only applied in the industry for condensate removal and do not appear to have been applied for removing condensed contaminants. When condensing contaminants from natural gas, the droplet size of the dispersed contaminant is small - typically on the order of 1 μm . Cyclones can only handle droplet sizes [41] above 15 μm . There are cyclone developments that can handle smaller droplets but then the throughput is very small. Note that in gas well applications we are talking of flow rates on the order of 100's MMscf/d (million standard cubic feet per day) which is on the same order as ca. 100's tons/hr. To handle such throughputs large banks of cyclones are required effectively enclosed in a pressure vessel [41]. Droplet size and process intensification are thus the drivers for development of a new centrifugal technology.

In this study we examine a single device which by contrast can be placed in a pressurised pipeline rather than requiring a large pressure vessel. It is thus much smaller than a cyclone bank and as we will show can separate smaller droplets. The objective of this study is quantification of the improvement in the rotational particle

*Partially reproduced from: van Wissen, R.J.E., Brouwers, J.J.H., Golombok, M. In-line centrifugal separation of dispersed phases, submitted for publication, AIChE Journal

separator (RPS) with respect to a cyclone [14, 15]. The principle is always to get the maximum gravitational effect but design for a small compact volume. At equal separator volume the RPS can remove smaller particles (ca. $1 \mu\text{m}$) and for removing larger particles, the separator volume is a lot smaller than for cyclones.

In section 4.2 we identify independent process parameters in which the performance of both in-line centrifugal separators can be expressed. These parameters are the residence time, τ , which defines the separator size and thus the capital cost, and the specific energy consumption, ϵ , defining operating cost. These are compared for the same throughput duties defined by feed flow Q . Section 4.3 evaluates these parameters for the axial cyclone and this is also done for the RPS in section 4.4. The two devices are compared and discussed in section 4.5.

4.2 Centrifugal Separations

We summarise the controllable variables for separation of dispersed phases in a rotating gas. The effect of the different mechanisms will be subsequently considered - here we assume that an element of fluid containing dispersed phases has been brought into rotation around an axis (fig. 4.1). The essential engineering is then the different mechanical configuration geometries which we subsequently apply.

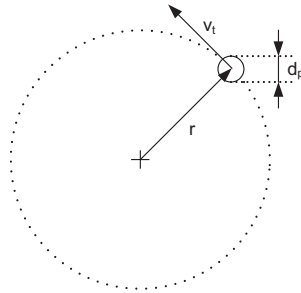


Figure 4.1. Schematic for a particle rotating around an external axis in a gas flow.

4.2.1 Particle kinematics

The dispersed phase is represented by spherical particles of diameter d_p and density ρ_p . The velocity by which the particles move radially can be calculated from a balance between the centrifugal force and the fluid force which is exerted on the particle in case of motion relative to the surrounding carrier fluid[8]. For particles with diameters ranging from about $0.1 - 100 \mu\text{m}$, the fluid force can be described according to Stokes-law. For smaller and larger particles Cunningham and Reynolds' number corrections have to be introduced[28], respectively, but these are not considered here. We equate the viscous drag (from Stokes equation) to the centrifugal force on the

particle. Solving for the radial migration velocity of the particle we obtain:

$$v_r = \frac{dr}{dt} = \frac{(\rho_p - \rho_f) d_p^2 v_t^2}{18\mu r} \quad (4.1)$$

where ρ_f is density of carrier fluid and μ its dynamic viscosity, v_t tangential velocity and r radial position. Tangential and axial velocity of dispersed phases are to first order equal to those of the carrier fluid. Furthermore, for the separator configurations considered, the tangential velocity can be taken constant with respect to the radial distance over which the migration of particles takes place. Integration of eq. (4.1) yields

$$r^2(\tau) - r^2(0) = \frac{2(\rho_p - \rho_f) d_p^2}{18\mu} \int_0^\tau v_t^2 dt \quad (4.2)$$

The last term on the right hand side must be left as an integral because it is an integration for the time that the mixture experiences rotational impulse. Common to all forms of centrifugal separation is that this takes place over a characteristic length of separating unit L . The axial velocity v_{ax} of carrier fluid and particles is taken constant with respect to radius and the time τ in eq. (4.2) is the time for the fluid mixture to travel that axial distance i.e.

$$\tau = \frac{L}{v_{ax}} \quad (4.3)$$

To evaluate the integral on the right hand side of eq.(4.2), the behaviour of the angular speed of the particle in the course of time has to be known. While in a cyclone the swirl decays, in the rotational particle separator it is maintained through the presence of rotating walls. For now we keep the operating engineering equations as general as possible in their universally applicable form.

Uniform axial flow distribution enables us to estimate the lower bound capture particle diameter - the characteristic dimensions are shown in fig. 4.2. We consider a cylinder of radius R_w which is the typical distance to some form of wall where particles are collected. An axle of radius R_i is located in the centre of the cylinder. A swirling flow enters the cylinder on the left side. Because of uniform inlet flux 50% of particles which enter the cyclone will be present in the area defined by the radius $r > R_{50}$ and correspondingly the other 50% in the area $r < R_{50}$. The cut radius, R_{50} , is dependent on the presence and thickness of the axle in the centre of the cylinder, and has therefore a different value for respectively the cyclone and the RPS.

From eq. (4.2) it is clear that particles with larger diameter d_p , will undergo greater radial displacement in time $t = \tau$ than is the case for smaller particles. Particles with small diameter will go through the separator without contacting the wall. Because of the uniform flux, the smallest particle which undergoes a radial displacement $R_w - R_{50}$ in time τ has a 50% chance of being collected at the wall. The diameter of the particles which have a probability of 50% of reaching the collecting wall in a cyclone of length L can therefore be calculated from eq. (4.2) by substituting the boundary conditions

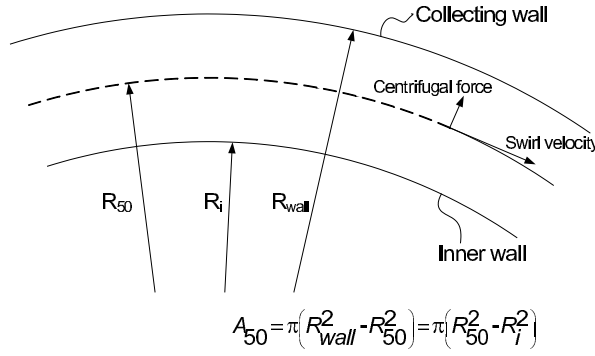


Figure 4.2. Geometry of droplet collection in centrifugal separation.

of eq. (4.3) (expressed in variable form $dt = dz/v_{ax}$) and $r(\tau) = R_w$ and $r(0) = R_{50}$. This results in

$$d_{p50} = \left[\frac{18\mu v_{ax} (R_w^2 - R_{50\%}^2)}{2(\rho_p - \rho_f) \int_0^L v_t^2 dz} \right]^{1/2} \quad (4.4)$$

Particle collection efficiency versus particle diameter is generally described by an S-curve in which the particle diameter is non-dimensionalised by d_{p50} : see figure 4.3. For $d_p \gg d_{p50}$ practically all particles will be removed by the inline separator; for $d_p \ll d_{p50}$ separation will be minimum. Given a certain particle distribution of dispersed phase, the overall separation will be governed by d_{p50} . Its value depends on specific design parameters: tangential velocity, axial velocity, radial distance to collecting wall, etc. In the subsequent section we will further specify d_{p50} for the cyclone and RPS, respectively. Before doing so, there is one other mechanical parameter to consider - namely the energy of the rotational swirl.

4.2.2 Swirl energy

Energy consumption occurs through the pressure drop the fluid undergoes when flowing through the separator. One can assume that the kinetic energy of the swirl which is induced at the entrance and all radial pressure build-up by swirl is eventually lost: the total irreversible pressure loss due to the swirl valve can be taken equal to

$$\Delta p_{cyc} = \rho_f v_{t0}^2 \quad (4.5)$$

where v_{t0} is initial swirl velocity of the fluid at the entrance of the separation device. $1/2\rho_f v_{t0}^2$ is due to axial friction and $1/2\rho_f v_{t0}^2$ is associated with reversible axial to rotational dynamic conversion. The total energy loss is given by the product of the volume flow rate and this pressure loss. The flow rate is simply the axial velocity

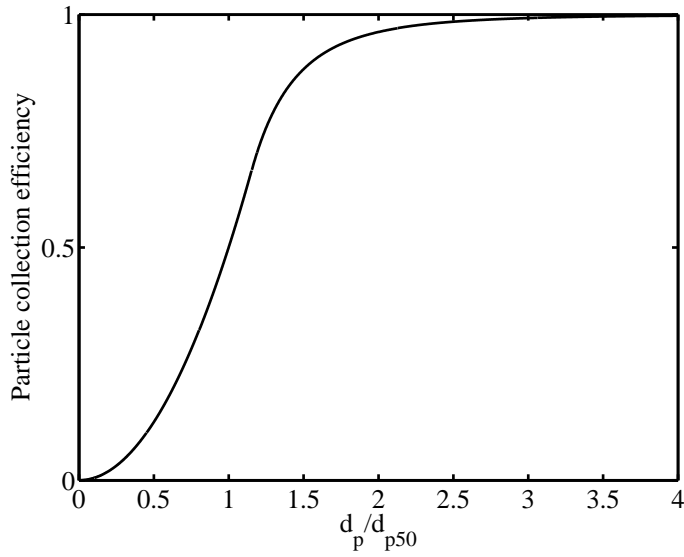


Figure 4.3. Particle collection efficiency as a function of particle size normalised to d_{p50} .

integrated over the cross sectional area

$$dQ = v_{ax} r dr d\theta \quad (4.6)$$

so that the total energy loss can be calculated by integrating over all radial positions:

$$\dot{E} = \int_0^{2\pi} \int_0^R \rho v_{t0}^2 v_{ax} r dr d\theta \quad (4.7)$$

Because we have constant uniform inlet flux this reduces to

$$\dot{E} = 2\pi \rho v_{ax} \int_0^R v_{t0}^2 r dr \quad (4.8)$$

with the constraint that the tangential velocity v_t is a function of the radial position. When the energy loss is related to the mass flow the specific energy consumption is obtained:

$$\epsilon = \dot{E} / \dot{m} \quad (4.9)$$

We have now defined three independent process variables, τ , ϵ , and Q . In the following eq. (4.4) is derived for both the axial cyclone and the rotating particle separator. Subsequently these equations are rewritten such that they are only a function of the three independent process variables. At a given flow, Q , τ is a good indication of

investment costs and ϵ of the operating costs. Therefore these variables form a good basis to compare the performance of the axial cyclone with that of the rotating particle separator.

4.3 Axial Cyclone

4.3.1 Geometry

The axial cyclone, also known as vortex tube or unflow cyclone, consists of a stationary cylindrical pipe which contains at the entrance stationary vanes or blades (fig. 4.4). Fluid enters the pipe and passes through these blades and attains a swirling motion. Dispersed phase entrained in the fluid attains this swirling motion as well. Having a density which is higher than the density of the carrier fluid, the dispersed phase will be subjected to a centrifugal force which causes it to move radially towards the cylindrical wall. It leaves the device via outlets so situated at the end of the pipe constituting the axial cyclone. Detailed investigations of swirling flows in pipes[40] have shown that the tangential velocity v_t changes its radial shape with axial distance from the point where the swirl is initiated. While initially the radial profile may be more like that of a free vortex ($v_{t0} \propto 1/r$ with a correction as $r \rightarrow 0$), with axial distance tangential velocity profiles evolve more towards that of solid-body rotation ($v_t \propto r$). At the same time the strength of the swirling motion decays as a result of wall friction. In the present analysis we shall assume that v_t is constant with respect to r intermediate between the two extremes. The axial decay is described by an exponential function in accordance with experimental observations[40].

$$v_t = v_{t0} \exp\left(-\frac{z}{2R}\beta\right) \quad (4.10)$$

where z is axial distance, R radius of cyclone wall and β an empirical factor which for conditions existing in cyclones is about 0.05[40]. v_{t0} is the initial swirl velocity provided by the (stationary) swirl valve i.e. v_t at $z = 0$.

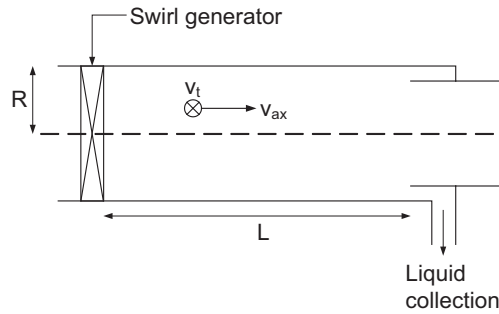


Figure 4.4. Schematic drawing of the axial cyclone.

The cut radius, R_{50} , of an axial cyclone can in absence of an axle be expressed as

a function of the wall radius R :

$$R_{50} = \frac{R}{\sqrt{2}} \quad (4.11)$$

Substituting into eq. (4.4) and performing the integration using eq. (4.2) we obtain

$$d_{p50\%} = \left\{ \frac{18\mu R}{4(\rho_p - \rho_f)v_{t0}^2} \frac{\beta v_{ax}}{1 - \exp\left(-\frac{\beta L}{R}\right)} \right\}^{1/2} \quad (4.12)$$

4.3.2 Swirl Energy

For v_{t0} and v_{ax} constant with respect to r , the energy loss of the swirl valve is:

$$\dot{E} = \rho v_{t0}^2 Q \quad (4.13)$$

where Q is the volume flow through the cyclone:

$$Q = v_{ax} \pi R^2 \quad (4.14)$$

The energy consumption rate per unit mass flow (eq. (4.9)) is thus $\epsilon = \dot{E}/(\rho_f Q)$ which on using eq. (4.13) and (4.14) becomes

$$\epsilon = v_{t0}^2 \quad (4.15)$$

We can use this result to rewrite the pressure drop over the cyclone (eq. (4.5)) which now relates to ϵ as:

$$\Delta p = v_{t0}^2 \rho_f = \epsilon \rho_f \quad (4.16)$$

The degree of swirl imposed at the inlet of the cyclone is in general limited[40]. For large values of the swirl ratio (tangential velocity to axial velocity i.e. $Sw = v_{t0}/v_{ax}$) a reverse flow in the centre of the cyclone will appear which leads to mixing of separated material. To avoid this, the swirl ratio is limited to a value $Sw = 2$. We thus have

$$v_{ax} = v_{t0}/2 \quad (4.17)$$

which on applying eq. (4.15) becomes

$$v_{ax} = \frac{\epsilon^{1/2}}{2} \quad (4.18)$$

4.3.3 Parameter re-expression

In line with our wish to express performance in terms of τ , ϵ and Q we can use eq. (4.3) along with eq. (4.18) to obtain

$$L = v_{ax} \tau = \frac{1}{2} \epsilon^{1/2} \tau \quad (4.19)$$

as well as the expression for the volume $V = Q\tau = \pi R^2 L$ in which we now substitute eq. (4.19). Cancelling out τ and solving for R we obtain

$$R = \sqrt{\frac{2Q}{\pi}} \frac{1}{\epsilon^{1/4}} \quad (4.20)$$

We have now obtained expressions for the cyclone length L and radius R in terms of the desired controllable variables namely the volume flow (Q), energy consumption (ϵ), and residence time (τ). These are now used together with eqs. (4.15) and (4.18) to express d_{p50} given by eq. (4.12) as a function of the volume flow of carrier fluid Q which is to be filtered:

$$d_{p50}^2 = \frac{9\mu}{(\rho_p - \rho_f)\pi} \frac{Q}{\tau\epsilon^{3/2}} \frac{\gamma}{1 - e^{-\gamma}} \quad (4.21)$$

where

$$\gamma = \beta \left(\frac{\pi}{8}\right)^{1/2} \frac{\tau\epsilon^{3/4}}{Q^{1/2}} \quad (4.22)$$

In the above relation we emphasise again the two important design parameters which occur: the residence time τ which is a measure for the size of the device and thereby for the capital costs, and the energy consumption ϵ which determines to a large extent the operating costs. Using these parameters it is possible to compare the separative performance of the cyclone with that of the rotational particle separator, as will be done in section 4.5.

4.4 Rotational Particle Separator

4.4.1 Geometry

The inline version of the rotational particle separator (RPS) is an axial cyclone within which a rotating separation element is built[34, 42]: Fig. 4.5. The rotating element consists of a multitude of axially oriented channels of diameter of about 1 to 2 mm. The element is freely mounted in bearings and rotates as a result of the torque executed by the swirling flow entering the element. As the rotating element is entirely contained within a cylindrical stationary pipe the device is also suitable for operating under high pressure.

The separation process taking place in the channels of the RPS is similar to that in the cyclone. The radial migration velocity of a particle can be expressed by eq. (4.1), where in this case r is the radial position of the channel. First we consider the configuration of concentric rings, see figure 4.1. The rings are narrowly spaced: therefore, the radial path of a particle in the channel can be calculated disregarding variations of velocities with r . To determine the diameter of the particle which is collected with 50% probability, two steps have to be made. First of all the radial position R_{50} of the channel for which 50% of the inlet flow occurs at $R > R_{50}$ and 50% of the flow

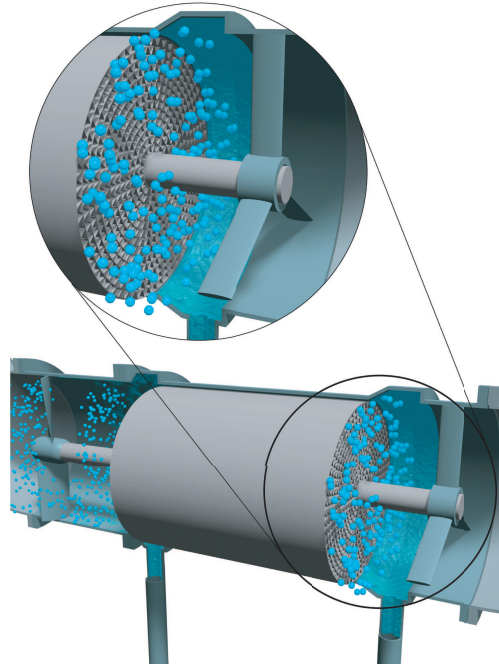


Figure 4.5. Rotational particle separator construction geometry showing operating principle.

occurs at $R < R_{50}$ has to be identified. In our case the axial gas flow entering the filter element of the RPS is constant with radius so we may immediately write

$$\pi(R_{50}^2 - R_{id}^2) = \pi(R_{od}^2 - R_{50}^2) \quad (4.23)$$

where the channels begin at an inner radius of R_{id} and extend to R_{od} . If we define $\delta = R_{id}/R_{od}$ - the ratio of inner to outer radius - then the expression for R_{50} is:

$$R_{50} = \frac{R}{\sqrt{2}} (1 + \delta^2)^{1/2} \quad (4.24)$$

The second step is to determine d_{p50} for the particles entering the channel located at R_{50} . Again assuming uniform flow and uniform distribution of particles at the entrance, the particle which is collected with a chance of 50% is the particle which starts halfway at the entrance and reaches the collecting wall at the exit (see fig. 4.2).

We can now substitute the terms relevant for the RPS geometry into the general defining equation eq. (4.4). The tangential velocity equals Ωr where Ω is the angular speed of the rotating element. As for the cyclone, the axial velocity v_{ax} is constant with respect to r so that

$$v_{ax} = \frac{Q}{\pi R^2 (1 - \delta^2)} \quad (4.25)$$

One then obtains

$$d_{p50}^2 = \frac{9\sqrt{2}\mu d_c Q}{(\rho_p - \rho_f)(1 + \delta^2)^{\frac{1}{2}}(1 - \delta^2)\pi\Omega^2 LR^3} \quad (4.26)$$

4.4.2 Swirl energy

As in our analysis of the cyclone, we wish to obtain an expression for the size selective separative power in terms of the residence time τ , throughput Q and the energy consumption ϵ . In the case of the RPS, the procedure to do this is somewhat more extended than for the cyclone because the energy consumption of the RPS consists of two parts.

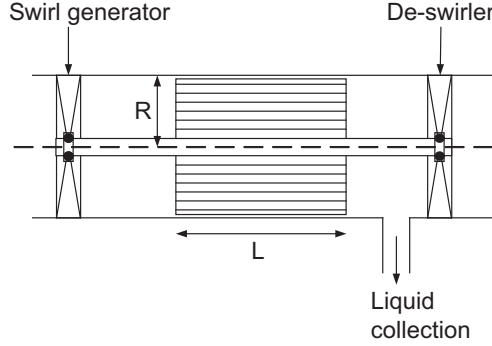


Figure 4.6. Schematic drawing of the rotational particle separator.

First there is the energy loss because of rotation. Downstream of the filter element a stationary de-swirler is installed (Fig. 4.6) which recovers about half of the energy associated with swirl - the reversible axial to rotational dynamic conversion identified in section 4.2.2 above. Therefore the irreversible pressure drop along each stream line passing through the rotating filter element is taken equal to half of that of the cyclone (eq. (4.10)). This irreversible pressure drop is given by $1/2\rho v_t^2$. Since $v_t = \Omega r$ then at the average point $r = R_{50}$ the pressure drop defined by eq. (4.24) is

$$\Delta p_t = \frac{1}{4}\rho(\Omega R)^2(1 + \delta^2) \quad (4.27)$$

The second source of energy consumption is pressure drop in the small-sized channels of the RPS. The pressure drop over the channels is the standard drag term given by

$$\Delta p_{ch} = \frac{1}{2}\rho_f v_a x^2 f \frac{L}{d_c} \quad (4.28)$$

where f is friction factor which depends on Reynolds number of the flow. For $Re < 10^5$ one can take the Blasius formula[8]:

$$f = 0.316Re^{-0.25} \quad (4.29)$$

The total energy consumption per unit volume flow, or equivalently irreversible pressure drop, can be expressed as the sum of these two terms

$$\Delta p_{RPS} = \Delta p_t + \Delta p_{ch} \quad (4.30)$$

As stated at the beginning of this section, we wish to re-express eq. (4.26) in terms of the independent variables Q , τ , ϵ rather than L , R , v_{ax} and Ω . To do this we show that the minimum size of particle that can be removed in the RPS is determined by pressure drop. Eqs. (4.25), (4.27) and (4.28) can be used to eliminate L , R and Ω from the right hand side of eq. (4.26), following a procedure similar to that done for the cyclone. (The derived expressions for the dimensions can be found in the appendix.) The result is:

$$d_{p50}^2 = \frac{9\mu d_c^{\frac{5}{6}} (1 + \delta^2)^{\frac{1}{2}} f^{\frac{1}{6}}}{2^{\frac{5}{3}} (\rho_p - \rho_f) \pi^{\frac{1}{2}} (1 - \delta^2)^{\frac{1}{2}} (\Delta p_{ch})^{\frac{1}{6}} \Delta p_t} \frac{\rho^{\frac{7}{6}}}{Q^{\frac{1}{2}} \tau^{-\frac{5}{6}}} \quad (4.31)$$

Recall that d_{p50} is the critical size parameter of droplet which have a 50% chance of being collected. If the pressure drop specified by eq. (4.30) becomes larger, then eq. (4.31) indicates that this critical size gets smaller i.e. the separator can pick out even smaller particles. i.e. d_{p50} becomes smaller (better separation performance) with increasing dissipations Δp_t and Δp_{ch} .

The question now is which is more important? - Δp_t the pressure drop due to swirl or Δp_{ch} , the pressure drop due to drag in the channel. To analyse this, we define the ratio of dissipation in the channels to the total dissipation,

$$x = \Delta p_{ch} / \Delta p_{RPS} \quad (4.32)$$

so that the complimentary swirl energy dissipation fraction is given by $1-x$. Eq. (4.31) now has the form

$$d_{p50}^2 \sim \frac{1}{(\Delta p_{ch})^{\frac{1}{6}} \Delta p_t} = \frac{1}{(\Delta p_{RPS})^{\frac{7}{6}} (x)^{\frac{1}{6}} (1-x)} \quad (4.33)$$

From eq. (4.31) it is clear that we want x to have a value such that the total dissipation is a maximum and the value d_{p50} is a minimum as well (maximum separation performance). Differentiation and minimisation of eq. (4.33) shows that this happens when $x = 1/7$, so that

$$\begin{aligned} \Delta p_{ch} &= \frac{1}{7} \Delta p_{RPS} \\ \Delta p_t &= \frac{6}{7} \Delta p_{RPS} \end{aligned} \quad (4.34)$$

Of course, in real application it is impossible to ensure that this always applies - so the question is then, how sensitive is performance to having $x = 1/7$. If we do a sensitivity analysis of d_{p50} as a function of x around the desired value we find that it is only slightly sensitive to deviations of x from its optimum value of $1/7$. For example a deviation of x of 20% from its optimum value leads to an increase of d_{p50} of 0.2%. For $x = 1/7$ the expression for d_{p50} becomes

$$d_{p50\%}^2 = \frac{4.57\mu d_c^{\frac{5}{6}} f^{\frac{1}{6}}}{(\rho_p - \rho_f) \pi^{\frac{1}{2}} \left(\frac{1 + \delta^2}{1 - \delta^2} \right)^{\frac{1}{2}}} \epsilon^{-\frac{7}{6}} Q^{\frac{1}{2}} \tau^{-\frac{5}{6}} \quad (4.35)$$

where $\epsilon = \Delta_{RPS}/\rho_f$ (the RPS analogy to the cyclone equation (4.16) above) and

$$f = \left(0.316 \left(\frac{2}{7} \right)^{-\frac{1}{12}} \rho_f^{-\frac{1}{4}} d_c^{-\frac{1}{3}} \mu^{\frac{1}{4}} \epsilon^{-\frac{1}{12}} \tau^{\frac{1}{12}} \right)^{\frac{12}{11}} \quad (4.36)$$

For given values of d_c and δ , eq. (4.35) thus specifies d_{p50} of the RPS versus flow Q with residence time τ and specific energy consumption ϵ as parameters. Two results of this analysis are worth noting:

- d_{p50} decreases with δ - the ratio of channel inner to outer diameter (eq. (4.24) above). However as for x defined above, the dependence is weak; in practice the inner radius of the filter element is taken about 1/3 to 1/2 of the outer radius
- from eq. (4.35) it is seen that d_{p50} of the RPS becomes smaller with channel diameter d_c . In practice, however, d_c is limited by fabrication and operational requirements to about 1 mm.

This last point leads naturally to a consideration of the optimal channel geometry which we consider in the next sub-section.

4.4.3 Channel geometry

In reality the usage of open concentric rings is not ideal as it can lead to unwanted tangential flows between the rings i.e. within the annular channels. A way to resolve this is to partition the rings using radial separators. The effect these partitions have on the axially streaming flow is only minor. Therefore eq. (4.26) is still applicable for this situation. However, from an engineering point of view it is difficult and thus expensive to produce an RPS with partitions. A more practical way is to make RPS filters of two layers of sheet metal, one straight and one corrugated which are coiled to form the necessary layers of channels (a process similar to the fabrication of corrugated paper). The resulting channels are triangular-like in shape, see fig. 4.7.

The geometry of channel used affects the separation performance because the distance which a particle has to travel is shortened for most of the channel width. Thus in fig. 4.7(b) for the concentric rings the particle must still travel a distance determined by the channel separation d_c which is constant. However for the triangular channels, the effective channel thickness varies around the concentric rings. The channel width varies linearly with the half periodicity s along the ring between the maximum separation $h(0) = d_c$ and $h(s) = 0$ so that the channel width at any point is now given by

$$h(x) = d_c(s - |x|)/s \quad (4.37)$$

The effective channel width, d_{eff} , for this type of channel can be calculated by evaluating the travel distance over volume flow to arrive at a weighted or effective channel height:

$$d_{eff} = \frac{\int_0^s h(x) Q(x) dx}{\int_0^s Q(x) dx} \quad (4.38)$$

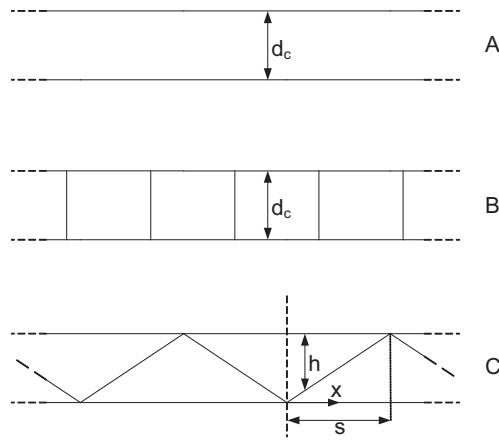


Figure 4.7. Possible shapes of the RPS channels (a) concentric rings, (b) concentric rings with radial partitions, and (c) corrugated triangles.

Using $Q = Q_0(s - |x|)/s$ where Q_0 is flow through the channel, this results in $d_{eff} = \frac{2}{3}d_c$. As the effective channel height of the triangular channels is smaller than that of the concentric rings it can be seen from equation (4.26) that the separation performance of these channels will be better. However, there will be more friction losses at the wall, leading to higher energy consumption. To avoid this, a larger height has to be designed effectively leading to roughly the same channel height as in the case of concentric rings.

4.5 Discussion

Eqs. (4.21) and (4.35) can be used to compare the separative performance of the cyclone and RPS as a function of volume flow Q at equal values of specific energy consumption ϵ and residence time τ (=building volume). The result for separation of water droplets ($\rho \approx 1000\text{kg/m}^3$) from air at ambient conditions ($P = 1$ bar, $T = 20$ °C, and $\rho = 1.2\text{kg/m}^3$) is shown in fig. 4.8, which displays d_{p50} for both units as a function of flow in actual cubic metres per second. Residence time and specific energy consumption are set at values commonly found in practice of $\tau = 0.1$ s and $\epsilon = 2\text{kJ/kg}$ which corresponds to $\Delta P \sim 2500$ Pa at $P = 1$ bar and $T = 20$ °C. The RPS channel diameter and inner/outer radius ratio are taken equal to the standard production values of $d_c = 1.5$ mm and $\delta = 0.5$. As can be seen, the smallest particles collected by the RPS are an order of magnitude smaller than those collected by the axial cyclone. Equivalently we see that an RPS can take a throughput 10000 times higher than a cyclone when it comes to collecting 1 m sized droplets.

Fig. 4.9(a) and 4.9(b) show the results for varying values of residence time and energy consumption respectively. Throughput is fixed here at a moderate value of 1 m³/s. The results for the RPS are in both cases again an order of magnitude better

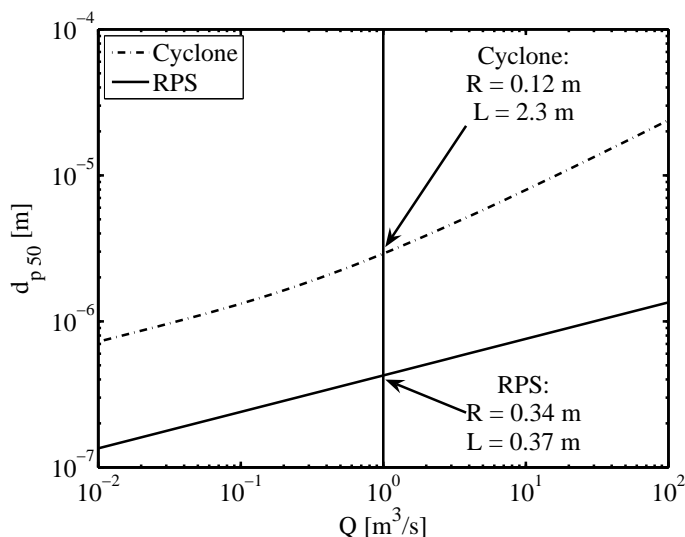


Figure 4.8. d_{p50} as a function of volume flow.

than that of the axial cyclone. Both units show a large increase in performance for higher residence time and energy consumption.

Although fig. 4.8 and 4.9 are plotted using the properties of air at ambient conditions, they are approximately valid for all gases at a large pressure range, since the properties of the carrier fluid are of minor influence as follows from eq. (4.21) and (4.35). The influence of pressure is seen in both cases to be inversely proportional to the difference between the particles and gaseous phases i.e. $\rho_p - \rho_f$. For a carrier gas pressure of 100 bar the density difference term in these equations still has approx. 90% of the value it has for a carrier gas at ambient pressure, i.e. $\Delta\rho \approx 900$ kg/m³ instead of 1000 kg/m³. Using eqs. (4.21) and (4.35) one can see that in this case this would lead to an increase in d_{p50} of about 6%, which is only marginal. When the carrier fluid is a gas, then this inverse density term is at best a second order correction for the range of pressure conditions normally encountered in practice - the justification for this is the range of surface facility inlet manifold pressures - these are typically in the range 70 – 130 bar. Thus the performance of the separator at 1 m³/s can correspond to either a gas flow at 1 bar or at 100 bar equivalent to 100 normal m³/s. (The latter corresponds in imperial production units to 300 MMscf/d - a good sized gas well.)

The only situation where the inverse term *is* important, is when the carrier fluid is a liquid instead of gas at ambient pressure. An example is the application of oil-water separation when decrease of the pressure difference term is of course substantial. This leads to a shift upwards, i.e. larger d_{p50} , for the results in fig. 4.8 and 4.9 which remain universally applicable. This effect is equally large for both the cyclone and the RPS as follows from eqs. (4.21) and (4.35).

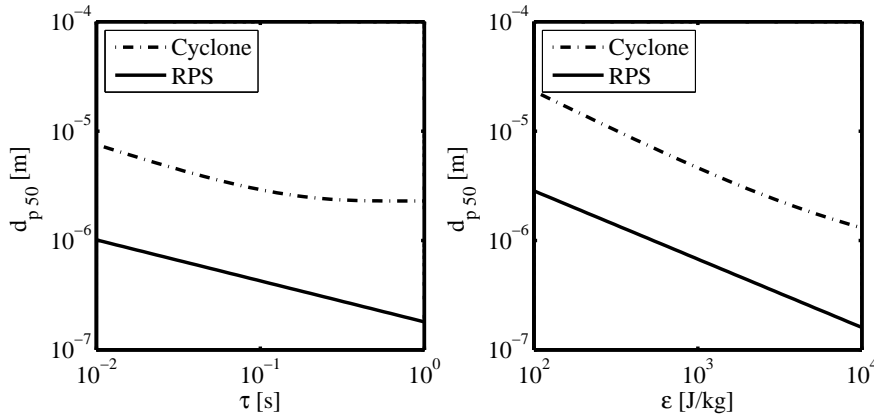


Figure 4.9. d_{p50} as a function of (a) residence time (left), and (b) energy consumption (right).

In addition we note that for application to contaminated gas, that condensed hydrocarbon fluid droplets are significantly more compressible than water. This compressibility actually means that it is favourable to carry out the processes at higher pressure because any increase in the density gas is more than offset by the significant increase in the fluid density in eq. (4.35). This all the more so for contaminated gas since the condensed waste liquid CO_2 contains typically ca. 10% methane gas which makes the liquid phase even more compressible. The relative advantage of using the RPS system for cleaning gas is seen in fig. 4.10 where the effect of pressure is seen to be large at the levels of flow associated with gas well production. For this example of industrial relevance the units of flow are the gas production industry norm: MMscf/d (millions of standard cubic feet per day -for SI conversion 1 MMscf/d= 0.33 norm m^3/s .)

The results for both units are a function of volume flow and *not* of mass flow. This means that an increase in pressure will not only lead to a smaller unit, at constant residence time, but also to a better separation performance at equal mass flow. For instance, from fig. 8 it can be seen that for air at ambient pressure carrying water droplets the d_{p50} of a well designed RPS with a throughput of 1 m^3/s is equal to $d_{p50} \sim 0.4\mu\text{m}$. Increasing the pressure to 10 bar leads, at equal mass flow and for an ideal gas, to a volume flow of 0.1 m^3/s . Fig. 8 shows that for this flow the d_{p50} for an RPS reduces to $0.2\mu\text{m}$. At the same time the volume of the RPS has decreased equally with the volume flow, to 0.1 times the original size. If the original separation performance, before the pressure increase, was satisfactory, then one could also, by increasing the pressure, reduce the residence time or energy consumption, without affecting the separation performance. This leads to an even smaller device or to lower operational costs.

Application of the RPS implies the introduction of rotating equipment. Complications involved with rotation, however, are limited. Peripheral speeds of the rotating

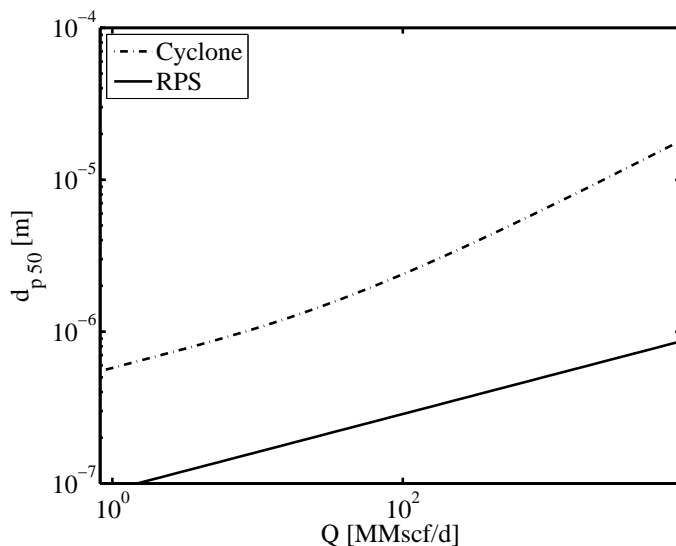


Figure 4.10. d_{p50} as a function of normal (i.e. molar) flow for a 50/50 CH_4/CO_2 separation system at $p = 27$ bar, $T = -47$ °C.

body are limited, typically to 50 m/s which is far below the speeds where structural integrity might become problematic. In fact, the speeds are limited because of constraints on energy consumption (value of ϵ). Sealing problems of shafts penetrating through stationary walls do not exist either. The RPS is internally driven by the swirl of the gas entering the rotating body. External drive by a motor is not necessary. In summary, the complexities involved with rotation are rather modest; they are outweighed by the advantages being the possibility to collect micron-sized particles in a device of limited dimension.

4.6 Conclusions

1. The separation performance of in-line centrifugal separators expressed as the diameter of the particle that has 50% chance of separation, d_{p50} , is a function of three independent process parameters: residence time, specific energy consumption and volume flow. These three parameters can be used as a basis for comparison between different separator configurations.
2. The Rotational Particle Separator (RPS) is able to separate an order of magnitude smaller particles than the axial cyclone is able to, at equal residence time, specific energy consumption and volume flow.
3. At the same droplet diameter, eg. for $d_p = 1\mu\text{m}$ in figure 4.9b, then the energy consumption is an order of magnitude less for the RPS than for the cyclone.

4. If the carrier fluid is a gas then the separation performance of an centrifugal separator as a function of volume flow varies only slightly with pressure. An increase in operating pressure leads at equal mass flow rate to a smaller volume flow rate and thus to a better separation performance or smaller equipment.

Chapter 5

The development of a 60 nm³/h C3-sep prototype

5.1 Loop design

In order to get a proof of concept of the C3-sep-system a laboratory prototype was designed in cooperation with Shell International Exploration and Production. This prototype has been built by Shell in one of their experimental labs in Amsterdam. This section describes the design of the loop system, the following section focusses on the design of the rotational particle separator which is part of this loop system.

In the concept described in chapter 2 it is envisioned that one can use an elevated top hole pressure for the expansion cooling. However there is of course no gas well or gas production facility available in the experimental labs in Amsterdam. Therefore the experimental setup used is a loop-system, which encompasses a gas conditioning section to bring the gas to a temperature and pressure comparable to top hole conditions. A schematic of the C3-sep prototype loop is shown in figure 5.1. The benefit of a loop system is of course that no continuous gas feed is required, but the gas conditioning section, comprising a compressor, cooler and several buffer vessels, adds extra complexity and costs to the system.

A molar gas composition of 50 % CO₂ and 50 % CH₄ is used as design criteria for this loop, it is of course possible to use any CH₄/CO₂ mixture. Also the possible addition and use of higher hydrocarbons and water in the system is desirable. A last design criteria is that the compressor has a maximum pressure of 150 bar. Using the procedures discussed in chapters 2 and 3 the optimal thermodynamic condition for a one stage separation of a 50/50 CH₄/CO₂ mixture is determined. In case of isentropic expansion a gas with $p = 145$ bar and $T = -5^{\circ}\text{C}$ is expanded to $p = 27$ and $T = -55^{\circ}\text{C}$. We will only have isenthalpic expansion available – why is explained further on – resulting in a temperature of only -47°C . The resulting product gas has a composition of 68/32 CH₄/CO₂; the recovery, as is defined in chapter 3, is approximately 95 %.

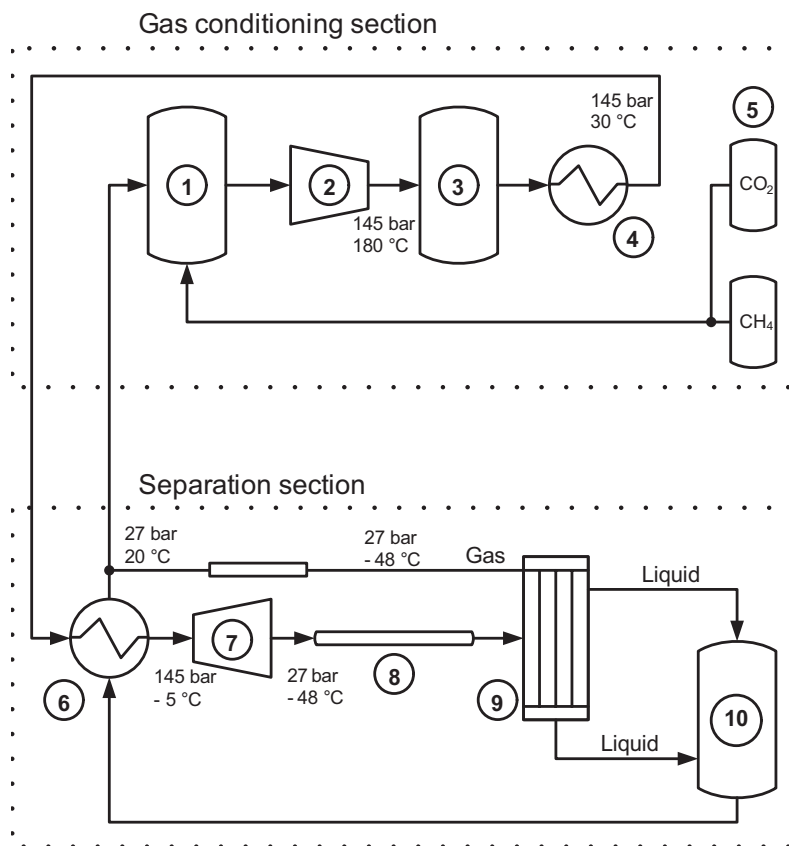


Figure 5.1. Schematic of the 60 nm³/h C3-sep prototype. Devices indicated by numbers are: (1) Buffer vessel (2) Diaphragm compressor (3) Buffer vessel (4) Cooler (5) Gas (feed) vessels (6) Heat exchanger (7) JT-valve (8) Induction loop (9) RPS (10) Liquid collection and storage vessel.

5.1.1 Flow sheet

The schematic in figure 5.1 is divided in two sections: the gas conditioning section and the separation section. This is not only a functional division, but also a physical one: each section is located in a separate lab, they are connected by 25 m of piping. In the gas conditioning section the gas is compressed up to 145 bar, resulting in a temperature of approximately 180 °C after which the gas stream is cooled by a water cooler. Now the gas, having a temperature of approximately 30 °C, is fed to the separation section. Here it enters a heat exchanger, which uses the returning CO₂-rich liquid from later in the process to cool the gas stream further to -5 °C. This heat exchanger has two functions: cooling the gas and evaporating the liquid stream so that it can be mixed with the gas stream coming out of the separator. After the heat

exchanger, the gas is expanded in a Joule-Thompson (JT) valve. The reason a JT-valve is used will be discussed below. The isenthalpic expanded gas has a pressure of 27 bar and a temperature of -47 °C. It enters a part called the induction loop, which is actually a 1.2 m long pipe section. This pipe can have various diameters, thus also various residence times. In the JT-valve and induction loop droplets are formed by homogenous and heterogeneous nucleation. The pipes of the induction loop can be exchanged with pipes of different diameter, making it possible to investigate the influence of residence time on droplet growth/nucleation and coagulation. Directly after the induction loop is the rotational particle separator where the liquid droplets are separated from the gas stream. Liquid is extracted at two points: before and after the filter. These two liquid streams are fed to a liquid collection and storage vessel, which has a system that compensates for the pressure difference before and after the filter. It is also used to store the liquid during the night; the two-phase mixture slowly heats up then, as there is no cooling, resulting in higher pressure. This storage vessel is built such that it can cope with the higher pressures. After the liquid collection and storage vessel the liquid is used to cool the heat exchanger and subsequently mixed with the gas stream from the RPS. The gas coming out of the separator and the evaporated liquid coming out of the heat exchanger are electrically heated in order to get a temperature of 20 °C. Heating is necessary to prevent liquid formation in the compressor. Finally the mixed gas stream is led back to the gas conditioning section.

At several points in this system there are pressure and temperature measurements and safety systems; before and after each device. In case of an emergency the gas stream is led to an incinerator or a venting system. There is of course also a flow rate measurement and control system, in this case a Honeywell system. Between the JT-valve and the induction loop and between the induction loop and the RPS there is optical access in order to use a laser particle sizer. This can either be an laser obscuration device or an rayleigh-scattering based system. The streams coming out of the RPS can be led to a real time gas analyser to measure the composition. An Agilent 5973 mass spectrometer is used for these measurements, or a micro gas chromatograph; both are available.

5.1.2 Compressor and sizing

The flow rate that can be achieved is dependant on the size and capacity of the compressor, which is also the most expensive part of this C3-sep setup. Due to capital and permit limitations it is only possible to buy and use a compressor with a flow of 60 nm³/h, i.e. 0.022 kg/s; the actual volume flow in the separator is approximately 1 m³/h. This compressor is a model D 123 LC 16 Burton Corblin diaphragm compressor. A rotary compressor, which is preferred in an industrial application for its higher efficiency and reliability, can leak lubricant to the process flow, due to the way it is sealed. A ordinary piston compressor suffers from the same drawback. In this laboratory C3-sep unit we want to prevent having even the lowest amount of lubricant or other contaminating components in the system; hence the selection of a diaphragm compressor, a system where the lubricant is fully separated from the process flow.

5.1.3 Expansion

As stated earlier, a Joule-Thompson valve is used for the expansion. Such an expansion is isenthalpic rather than the preferred isentropic expansion. At the same pressure decrease isentropic expansion results in a lower temperature than isenthalpic expansion. This is because with isentropic expansion there is actually heat or work withdrawn from the system, while isenthalpic expansion is an adiabatic process. Isentropic expansion can be performed by a turbine, however at these flow rate and pressures it proved to be impossible to buy an off-the-shelf turbine. Car turbo-chargers are low pressure turbines that have approximately the same flow rate and pressure ratio [27], but it is simply too expensive and time-consuming to produce a new high pressure turbine based on a turbo-charger. Therefore it is decided to use a JT-valve. Using this isenthalpic expander it is still possible to produce a substantial amount of enrichment and CO₂-rich liquid, enabling us to get a good proof of concept for C3-sep. Of course, any future upscaled unit should contain a turbo-expander instead of a JT-valve. An one stage enrichment with a turbo-expander with 100 % isentropic efficiency would result in 75 % CH₄ in the product stream instead of 68 % CH₄ for the JT-valve, using an otherwise same setup. A benefit of the JT-valve for the current experimental setup is that the valve makes it possible to vary the pressures over a larger range than would be possible with a turbo-expander; turbo-expanders are generally not flexible in this area. This makes it possible to test different gas compositions at their (isenthalpic) optimal thermodynamic conditions (see chapter 3). Flowserve supplied the JT-valve used in this setup.

5.1.4 Heat exchangers

The remaining large independent item from the gas conditioning unit that is ordered is the heat exchanger which cools the compressed gas using external cooling water (HX1). There is also a rather more complicated heat exchanger (HX2) that is subsequently required for preliminary cooling of the gas prior to J-T expansion and which also evaporates the waste CO₂ stream before remixing and recompression - and although this is drawn as part of the separator section it can really be considered as integral to the gas conditioning. There are a number of special aspects regarding these units - for example the elevated pressure of the warmer mixed inlet gas (150 bar) and the cold side of the second exchanger which evaporates a ca 90/10 liquid CO₂/CH₄ fluid. The specification and sizing of the heat exchangers were done by Shell Int. Exploration and Production and Shell Global Solutions.

Tables 5.1 and 5.2 summarise the functionality and input and outputs of the streams for the two heat exchangers. Aspen and Pro-II simulations were carried out to establish the heat duties required for the heat transfer surface. In HX1 a controller adjusts the flow of water so that the duty of HX2 is just sufficient to fully evaporate the CO₂ rich waste face which forms the cooling medium in HX2. (The fine tuning subsequently to get the gas streams mixed at the same temperature is done with electric trace heating.)

These heating duties with the phase transfer requirement of the cold side in HX2 were tendered to Geurts International B.V. who recommended two coil in shell type

Side	Material	T_{in} [°C]	T_{out} [°C]	p [bar]	Element
Cold	Water	20	30	3	Shell
Warm	CH ₄ /CO ₂ 50/50	200	40	150	Coil

Table 5.1. Heat exchanger details for HX1 which cools the compressed incoming gas using external cooling water.

Side	Material	T_{in} [°C]	T_{out} [°C]	p [bar]	Element
Cold	CH ₄ /CO ₂ 90/10	-47	-9	30	Shell
Warm	CH ₄ /CO ₂ 50/50	40	-5	150	Coil

Table 5.2. Heat exchanger details for HX2 which evaporates the fluid waste stream using the heat from the incoming gas.

heating exchangers - where in both cases the high pressure side is in the coil. The orientation and liquid filling of HX2 is particularly crucial in order to prevent blocked two phase flow formation. Optimisation of the flow volume during the waste stream boiling in the shell needs to take account of flow round the coil and the possibility of reduced heat transfer due to boiling liquid vapour film formation. To this end, the shell actually is formed from two concentrically located cylinders with the coil winding up between the internal walls. The coil occupies 40 % of the shell volume and windings are chosen to suppress surges by maximising heat contact area. The total free volume on the shell side is 8 l. of which 4l. will be liquid full. This allows for fluctuations both in flow and heat transfer efficiency.

In order to ensure that the heat exchanger does not run "dry" on the cold side, a small parallel tube vessel is constructed which fills to the same level. In this tube a level measurement and control device is used. An Endress and Hauser guided radar level meter was selected since this has been shown to work well with cryogenic systems and the dielectric constants were sufficiently different to provide the necessary contrast measurement ratios. Ideally it would have been desirable to measure the level in the HX2 shell directly, but the closeness of the coil windings do not leave sufficient room for insertion of a level meter - moreover with a radar meter it would lead to undesirable scattering of the signal which confuses interpretation. Accordingly a simpler geometry is required for an unambiguous measurement and a parallel filled tube scheme was chosen. (A similar scheme is used in the waste liquid collection vessel in the separator section - see below.)

One potential problem to be addressed is the risk of blockage in the narrow connecting lines between the evaporator/heat exchanger HX2 and the parallel level measuring tube. Because of the high surface to volume ratio at this point, there could be high heat ingress and a risk of blockages. The main source of blockage would be evaporation or cavitation bubbles so that the level in the parallel tube would not reflect that in the heat exchanger. This can be overcome by sloping the connecting tube from

a higher point connecting to HX2 to a lower point on the measuring parallel tube. Any bubbles formed will then return to the main evaporator HX2 and rise to the top at the liquid/gas interface approximately half way up the exchanger. An alternative blockage would be ice formation - but care has been taken to ensure that no water vapour enters the system. If there is failure of the level control then the whole system is connected to the liquid return system to the liquid storage vessel. If this also fails, then a second level of protection is provided by connection to the venting system via pressure relief control valves.

5.1.5 Induction loop

The induction loop is an essential part of C3-sep. It decouples the expansion from the separation process and it allows us to vary the residence time during the experiments in order to let particle grow or coagulate to a size that is easily separated. The induction loop consists of vacuum insulated pipes of DN15 supplied by Demaco B.V. A 1 m long section can be replaced by pipes of DN10/25/50/80/100, allowing a ranges of residence times for that part from 0.32 s to 32 s at a flow of 1,049 m³/h. Using the monodisperse coagulation theory explained in chapter 3 it is estimated that the droplets will be at least 1.8 μm large.

Vacuum insulation is applied to prevent that the cold mixture in the pipes heats up and that the droplets thus evaporate. The maximal heat influx in the induction loop is estimated by Demaco to be 12 W. This is an acceptable loss as will be shown later. Better insulation is possible and can be done by submerging the pipes in a cold bath, and controlling the temperature, but was decided not to be required.

5.1.6 Liquid collection and storage vessel

We have referred a couple of times to the handling of the liquid waste stream. This is collected from the RPS in a system which provides a liquid seal both at the top and bottom of the housing. The liquid waste is also transported to the heat exchanger/evaporator HX2. A liquid collection (and storage vessel) has ultimately been designed to be placed between the RPS and the insulated return line to the heat exchanger - its location is shown in figure 5.1 and it fulfils a number of important functions in the separating section. These are liquid collection from the separator, ensuring sufficient pressure for waste stream return to the heat exchanger/evaporator and thirdly, as a storage vessel at night when the system is not running.

Liquid collection

Within the RPS itself it is desirable to minimise the amount of liquid - any excess liquid collected would be small and easily susceptible to heating resulting in evaporation and overpressure above the 40 bar design. Accordingly the RPS was designed as discussed later, to have the minimum liquid hold up with just small quantities at the lip of the exit orifices to act as a liquid seal and prevent gas ingress. There are two exits from the RPS: one downstream of the rotating filter element and one just upstream of it. The former is expected to collect much more liquid than the latter.

The problem is that these two streams have to be combined. However they cannot simply be "dumped" in one vessel because the two streams are at slightly different pressures due to the axial pressure drop in the channels of the RPS. The fluid exiting from the downstream top of the RPS will be at a lower pressure (estimated at maximum ca. 0.1 bar pressure difference) than that from the upstream bottom end. If they were both merely to be piped to a single combination collection vessel then this would merely lead to reverse flow from the high pressure to low pressure outlet by the path provided external to the RPS. This is not what is required of course - we need to have outflow from both ends and to correct for the pressure difference.

After consideration of a number of schemes, we settled on one which uses the very siphon principle which was acting against us in the original problem. A long (ca. 1.5 m) collection tube is positioned vertically just underneath the RPS. Within this vessel there is a dip tube leading from the high pressure RPS exit directly to the bottom of the storage vessel. A pipe from the low pressure end of the RPS leads to the top of the collection vessel and determines the operating pressure inside the vessel. During operation, the fluid level in the vessel builds to a sufficiently high level that it counters the excess pressure from the high pressure RPS exit. Thus the pressure drop across the RPS balances the liquid level in the dip tube:

$$\Delta p_{rps} = \rho_w g h \quad (5.1)$$

The liquid level is controlled by a level control meter inside the vessel. (The level control is the same Endress and Hausser radar control stick type that was used to control the level of fluid in the evaporator/heat exchanger identified in section 5.1.4 above.) Thus, by use of the dip tube the pressure difference between the two streams is overcome and liquid can accumulate in one vessel.

Waste stream return

A second purpose of the collection vessel is to provide pressure head for return via the vacuum line to the heat exchanger HX2. Although not shown on the diagram in figure 5.1, the collection vessel will be spatially located above the heat exchanger HX2. Originally we considered a system using a liquid pump where fluid waste would be pumped directly from the separator outlet, via the vacuum insulated line to the evaporator heat exchanger. However there is a problem here in that we do not know what the liquid rates will be - and indeed it is expected that these are dependent on the rate of rotation of the RPS. An active pumping system would be problematic in this regime and when we combine this with the fact that there could be two phase flow due to residual evaporation, then it is much better to have a passive flow system. When this was supplemented by the considerations in the previous section 5.1.6 necessitating a liquid collection vessel, it was recognised that this unified purpose device would be sufficient to provide a head for flow to the evaporator and that this can be driven simply by letting the liquid level in storage vessel rise. This will also be assisted by the continual generation of liquid from the RPS. A level-regulated liquid control flow valve opens the flow from the bottom of the collection vessel to admit waste to flow to the evaporator.

Downtime storage

The third and final reason for using the collection vessel derives from the nature of the experimental program. Although this is a continuous flow unit, it will not be continually operated and will be switched off during nights and weekends. In addition, because of the experimental nature of the unit, there are bound to be a number of unexpected shut-downs and a logic procedure had to be developed for controlled and sequenced valve opening and removal of liquid from the system. The reason for this is that the natural operating condition of the system is such that there are significant quantities of liquid waste residing in the system at various points. (Recall that the waste is a 90/10 CO₂/CH₄ mixture at a temperature of -47°C and 27 bar. For example, it is estimated that there will be typically 4 l of liquid in the evaporator heat exchanger plus up to 1 l. in the collection vessel, during steady-state operation.

The problem then is that during a controlled or uncontrolled shut-down, liquid will warm up and evaporate significantly. The main problem comes from the section where liquid is located i.e. the liquid collection vessel, the vacuum insulated line and the evaporator heat exchanger HX2. The design pressure and temperatures are 50 bar for the evaporator and -50°C. For the RPS the design pressure is only 40 bar. If these systems heat up during down-time, the liquid mixture evaporates and then the pressure reached will be much higher than these design pressures.

The procedure we have followed is that during a shut down, the liquid collection vessel, also functions as a storage vessel for the waste liquid which has been sitting around in the system during steady state operation. Thus when a shut down occurs, all liquid waste residing in the evaporator, the insulated transfer pipe, and the RPS is drained back to vessel V-210 which is then isolated from the rest of the system. The question then is what the design pressure must be for the storage vessel. A total of 5 l of liquid is estimated to be collected. If we were to restrict the size of the storage vessel, then very high pressures would occur during evaporation. If however, we provide some expansion head-room, then the pressures reached are not too excessive. For example, in a 7l. vessel, then at 30°C a pressure of 183 bar would be reached. If this is enlarged to a 10 l vessel, then at 30°C a pressure of 106 bar is reached. There is a critical point for this mixture around 29°C - since it is theoretically possible to exceed this value, then Health and Safety requirements require a vessel which can cope with the elevated pressure. As it turns out, this value is not that excessive - a vessel size of 10 l. is sufficient to keep the pressure within reasonable limits i.e. < 100 bar.

This completes the discussing of the parts of the loop that were developed with Shell International Exploration and Production. The following section concerns the most important design aspect of the process: the rotational particle separator. It performs the task of spatially separating the liquid and gaseous phases and is the only part of C3-sep that is not standard technology for handling cold natural gas.

5.2 Separator Design

5.2.1 Introduction

The rotational particle separator in the C3-sep prototype is by far not the first RPS ever designed. Many variations of RPS are utilised commercially and experimentally [42, 34]. For the design of the C3-sep 60 nm³/h RPS prototype it was therefore possible to use to a great extent the open literature.

Brouwers [14, 15, 16] derived the basic equations required for the determination of the equipment dimensions. A design that was also made for in natural gas processing is the RPS by Mondt [34]. Here, water droplets are removed from natural gas coming out of a well. This RPS separates droplets and other contaminants down to 3 μm of a gas stream of 1500 m³/h at ambient temperature and at surface manifold pressure of 80 bar. The RPS of Mondt is currently still at prototype stage. Although the similarity to C3-sep is of course separation of liquid droplets from methane at high pressure, the differences are that the C3-sep design has to work at low temperatures and low flow rates, separating a high liquid fraction of CO₂ from a very low volume flow. In fact, there is no previous design of RPS that can run under these thermal conditions of can handle such a low volume flow. This makes it impossible to adopt an earlier, working, design and adjust it to suit the current requirements. Using the available knowledge a new sort of RPS is designed that will also form the basis for future higher throughput C3-sep designs.

5.2.2 Design criteria

Thermodynamic and operational requirements

The C3-sep thermodynamic design of the previous sections imposes several requirements on the design of the RPS; other design requirements follow from production and material limitations. This sections explains the effect of the requirements resulting from the overall C3-sep design; the subsequent section discusses the production and material limitations. From the previous sections it follows that the standard operating conditions will be a pressure of 27 bar, a temperature of -48 °C, a flow of 60 nm³/h, and liquid particles of 1.5 μm and/or larger; the design of the RPS has to at least match that.

Further upstream in the system there is a pressure possible up to 150 bar. A sudden failure of the JT-valve could mean that the pressure is not reduced before the separator. However, the separator will be coupled to an upstream pressure safety release valve, so designing for that pressure is not necessary. A pressure of 40 bar is used as design criteria to allow variations in the measurement programs. This is quite useful for doing measurements with different stream compositions and JT-valve settings.

In contrast to most rotating particle separators which are designed to cope with high temperatures, this RPS is designed for low temperatures, although temperatures are not that low that specific cryogenic technology is required. The temperature in the system is nowhere lower than the temperature after the JT-valve and in the separator. Over-designing for failure of up- or downstream components is therefore

not necessary. To allow some flexibility in the measurements a design temperature of -60 °C is used. At lower temperatures CO₂ is for a large range of thermal conditions solid, see chapter 3, and solid CO₂ is something we want to avoid during the prototype measurements. Lower temperatures would also impose higher demands on material selection, since most materials become brittle at these temperatures.

The volume flow entering the separator is approximately 1 m³/h. Even at fairly large residence times this leads to a very small separator. As the two-phase mixture enters the separator it has to be brought in rotation to meet the velocity of the filter element. At this low throughput axial velocity will be low, which, together with the relatively large rotational velocity, brings a risk of unstable flow and possible dissipation (and thus heating up) in the pre-separator. Also, the small dimensions of the separator result in a relatively large internal surface giving rise to dissipation, heating up and heat transfer with the environment.

Since we want the thermodynamics in the RPS to be as constant as possible, i.e. retain the temperature and pressure as delivered from the upstream systems, there are some limitations on pressure drop and heat in flux from the environment. We limit the pressure drop across the RPS to 0.5 bar. This results in the pressure loss being less than 2%. The thermodynamic conditions thus remain approximately constant. A limitation in pressure drop is, as can be seen from chapter 4, a limitation in the maximum rotational speed and filter length. This does affect the maximum separation performance. Nevertheless 0.5 bar is more than enough to meet separation performance requirements.

The maximum heat in-flux from the environment is calculated using the Aspen Plus flow sheet of chapter 3. Here heat is added to the flash calculation representing the separator. Figure 5.2 shows the liquid fraction in the separator as a function of heat added in the separator. At the flow rate used in the C3-sep prototype even a small amount of heat already affects the thermodynamic conditions, although even at a heat in-flux of 1200 W a considerable amount of CO₂ rich liquid can be collected in the RPS. Nevertheless heat in-flux has to be prevented as much as possible in order to acquire experimental results that are representable for the large scale application. There heat in-flux will be less due to the lower specific surface area. To prevent heat in-flux, the RPS is isolated with vacuum isolation where possible or else with Armaflex^{textttTM}.

Exact liquid droplets sizes are, as explained earlier, unknown. Therefore the RPS is over-designed such that it will be highly likely that all particles are collected in or before the filter. A d_{p100} of 0.5 μm is selected - well below the minimum expected droplet size. Due to the high pressure there will be turbulent flow through the RPS channels, which makes 100 % collection impossible. Hence the desired separation performance is expressed in the form of d_{p50} : $d_{p50} \sim d_{p100laminar}/\sqrt{2} = 0,35\mu\text{m}$, as is also done in chapter 4.

The piping leading to and from the RPS are vacuum insulated DN15 (18x1) AISI 316 tubes. In order to connect these tubes to the RPS using Swagelock couplings, the in- and outlet of the RPS should be the same size. The dimensions of the liquid removal pipes are arbitrary.

A last operational requirement is that the angular speed of the filter is free to

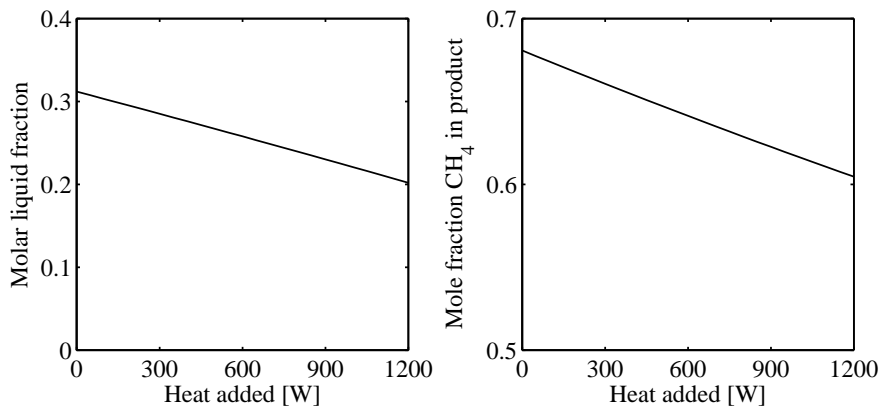


Figure 5.2. Molar liquid fraction and mole fraction CH₄ in product stream as a function of heat added in the RPS.

choose (within a reasonable range) during the experiments. This gives an extra degree of freedom during the experiment. If for some reason the separation performance of the RPS is less than expected, it will then be possible to raise the angular speed of the filter to increase performance. Also, if the separation is as expected, it will be possible to use the RPS as a simple particle sizer, i.e. by lowering the angular speed one can determine the point at which no liquid is separated. This point can then be compared with theory to estimate the particle size. There are currently two methods to rotate the element: passively where the element is brought into rotation by the gas which in turn is brought into rotation by a swirl generator and actively where the filter is connected to a motor. In the first method the rotation can be controlled by adjusting the angle which the swirl generator blades have relative to the flow. However, this is rather difficult to implement in a design, since it would need a rather sophisticated actuation and control scheme. A motor-driven RPS is far more simple to implement and control. It just requires a motor with a variable shaft speed. Commercially available DC-electro motors can do this; they are able to work at a large range of angular speeds, and are very suitable for the size of equipment we are designing for.

Material and production limitations

The separator is constructed from stainless steel, as is standard in gas production. In order to minimise stresses and avoid clearance problems due to the shrinking of the material when cooling from ambient conditions to $-60\text{ }^{\circ}\text{C}$, Duplex stainless steel type 1.4462 is selected. This material has a low expansion coefficient, is highly corrosion resistant and has a high tensile strength at $-60\text{ }^{\circ}\text{C}$ without becoming brittle. An alternative would be AISI 316 stainless steel, which, being an austenitic steel, is even more suited for low temperatures. It has, however, a higher expansion coefficient. The reason that we focus on expansion coefficient is that each measurement with this unit

will probably have a short duration, so there will be a lot of cooling and heating up of equipment. This can give high stresses on bearings and sealings due to expansion and shrinking of the RPS. A lower expansion coefficient minimises these stresses.

The tensile stresses on the material due to centrifugal forces can be neglected. Stainless steel is used as a construction material in many rotational devices such as pumps, compressors and turbines. The tensile stress is related to the square of the tangential speed the material has [30]. In turbines the tangential velocities are close to or even higher than the speed of sound of the gas flowing through the turbine [19]. This means that the tip-speed of the rotor blades is in the range of 300-400 m/s. The tangential velocity of the RPS filter wall is in the range of 20-60 m/s. Higher velocities of the RPS filter results in higher specific energy consumption, see chapter 4. Due to the lower tangential velocity the stresses will be one to two magnitudes smaller than in other rotational devices, therefore material strength is not a limitation for dimensioning an RPS filter element. Extensive Finite-Element-Modelling of the design in order to minimise stresses and maximise strength is therefore not required.

Most of the limitations in the design process come from the available production technology. RPS filter elements are currently fabricated by Duis Engineering B.V. They use an in-house laser welding technique to fabricate the filters in a way that is similar to the fabrication of corrugated paper. There are currently no other companies which can produce RPS filters. The fabrication method of Duis Engineering has some limitations: the length of the filter has to be less than 0.2 m, the minimal inner radius of the filter is at least 40 mm, and the height of the (triangular) channels is 1.5 mm. It is technically possible to deviate from these limitations, but it would then be necessary to do several alterations to the production equipment, which would make the production of this single RPS far more expensive.

5.2.3 Filter design

The filter element is the most important part of the RPS. It performs the main task of the device: the collection of the micron-sized CO₂ droplets. In contrast to a solid particle separating RPS, where the filter is really a particle collection device, the filter of a liquid droplet separating RPS is a coalescencer, i.e. it coalesces droplets so that they can be separated in the pre- and post separator of the RPS. For the design of a RPS filter element one can use the traditional method as is also used by Mondt [34] and described in Brouwers [14, 15, 16]. Another method of dimensioning an RPS filter is that described in chapter 4. We start with the latter.

The residence time required for separating the droplets is calculated using:

$$\tau = \left(\frac{4,57\mu d_c^{\frac{5}{6}} f^{\frac{1}{6}}}{(\rho_l - \rho_g)\pi^{\frac{1}{2}}} \left(\frac{1 + \delta^2}{1 - \delta^2} \right)^{\frac{1}{2}} \epsilon^{-\frac{7}{6}} Q^{\frac{1}{2}} d_{p50}^{-2} \right)^{\frac{6}{5}}, \quad (5.2)$$

which is easily derived by rewriting equation (4.35). This leads to a minimal value for τ of $9.5 \cdot 10^{-4}$ s. Using the derived expressions for the filter dimensions in appendix A this results in a filter length of 0.03 m, radius of 0.002 m, axial velocity of 32.2 m/s, and a tangential velocity of 55 m/s. It is immediately seen that these values are not

very realistic and conflict with the production limitations stated above. Therefore for this filter design it is more useful to design using the traditional method.

Looking at a rewritten version of equation (4.26) and keeping in mind the limitations stated above, we see that there are only two variables left for dimensioning the filter (if we use for L the maximum of 0,2 m):

$$d_{p50}^2 = \frac{9\sqrt{2}\mu d_c Q}{(\rho_l - \rho_g)(R + R_i^2)^{\frac{1}{2}}(R - R_i^2)\pi\Omega^2 L}, \quad (5.3)$$

namely the angular velocity, Ω , and the outer radius of the filter, R . Since the value of d_{p50} is known from the design requirements Ω and R are coupled by equation (5.3), so there is only one degree of freedom left. Figure 5.3 shows the angular velocity Ω , the axial velocity v_{ax} , the axial Reynolds number Re_{ax} , and the rotational Reynolds number Re_Ω as a function of the outer radius R . A channel height of 1.5 mm is used in the calculations for this figure. The axial Reynolds number is defined as [15]:

$$\text{Re}_{ax} = \frac{\rho_f u_f d_c}{\eta_f}, \quad (5.4)$$

and the rotational Reynolds number is defined as [15]:

$$\text{Re}_\Omega = \frac{\rho_f \Omega d_c^2}{\eta_f}, \quad (5.5)$$

As can be seen from this graph, angular velocities are always moderate to low ($\Omega < 300$ rad/s \sim 3000 rpm). Also, the peripheral velocity of the filter element is never higher than 12 m/s, which is low compared to other RPS designs [15, 34]. Although the axial and peripheral velocities are rather low, the associated axial and angular Reynolds numbers are high, due to the high gas density, causing the flow to be turbulent for the smaller radii. This could affect the separation performance slightly, so it would be better to take an outer radius of $R > 0.05$ m.

A problem that arises in practice when using larger outer radii, i.e. multiple radial layers of channels, is the occurrence of flow reversal in the outer channels. This can be explained by looking at figure 5.4. When a gas without rotation, and therefore uniform radial pressure distribution, enters an RPS filter it is tangentially accelerated such that it reaches a solid body rotation. In the channels there is an axial pressure gradient due to wall friction. As the gas leaves the filter at a slightly lower pressure, it is still in solid body rotation. The result is a radial pressure built-up similar to that in a gas centrifuge:

$$p(r) = p(R)e^{A(r^2 - R^2)}, \quad (5.6)$$

where

$$A = \frac{\overline{M}\Omega^2}{2RT}, \quad (5.7)$$

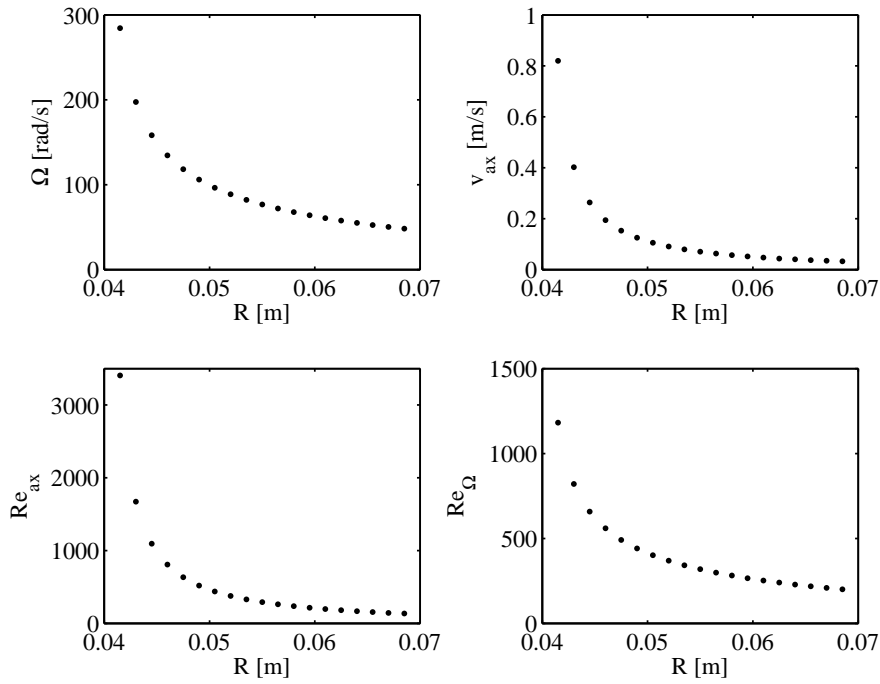


Figure 5.3. Angular velocity Ω , axial velocity v_{ax} , axial Reynolds number Re_{ax} , and rotational Reynolds number Re_{Ω} as a function of outer radius R for the 60 nm³/h C3-sep RPS prototype.

and \bar{M} is the average mole weight of the gas; $p(R)$ is calculated by:

$$p(R) = \frac{p_{feed} A R^2 (1 - \delta^2)}{(1 - e^{A R^2 (\delta^2 - 1)})} \quad (5.8)$$

Although this radial pressure build-up is only minor compared to that in a centrifuge, it is at low axial velocities, such as in this design, substantially larger than the axial pressure drop. The result is the reversal of flow in the outer channels due to the higher pressure in the outer radii of the area downstream of the filter. This is a common problem which can occur in any RPS. Normally in a stationary RPS this reversal of flow is circumvented by generating a certain tangential and axial velocity profile at the inlet, such that it compensates for the pressure built-up near the exit of the filter. The current design is not stationary in the sense that it has to be able to run at different operating points, i.e. at a variable tangential speed. In figure 5.5 the radial pressure difference at the filter exit is shown for several tangential speeds of the filter as a function of outer filter radius; it also shows the axial pressure drop in case of uniformly distributed flow through the filter, as a function of outer filter radius. As can be seen, the radial pressure drop is for the design speed more than an

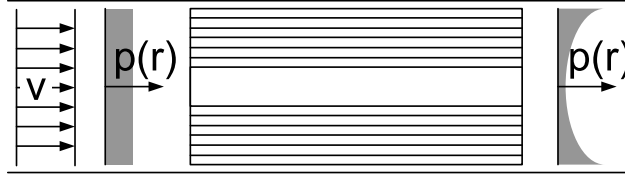


Figure 5.4. Schematic representation of the radial pressure distribution before and after a RPS filter. Gas enters from the left and has no rotation.

order of magnitude larger than the axial pressure drop, i.e. flow reversal is likely to occur, but could maybe be circumvented by adopting a certain inlet profile. However, doubling the tangential speed means that the radial pressure drop becomes four times larger. It is impossible to design a fixed inlet that generates a velocity flow profile that compensates this pressure drop for a large range of operating conditions. Therefore we chose to use a filter which consist of only one row of channels. This essentially makes flow reversal due to the above phenomena impossible. A drawback is that the flow in the channels is turbulent, but this also makes the experiment more realistic. In an upscaled version of the RPS such flow conditions will also occur, i.e. similar thermal conditions and velocities in the order of 1 m/s [34].

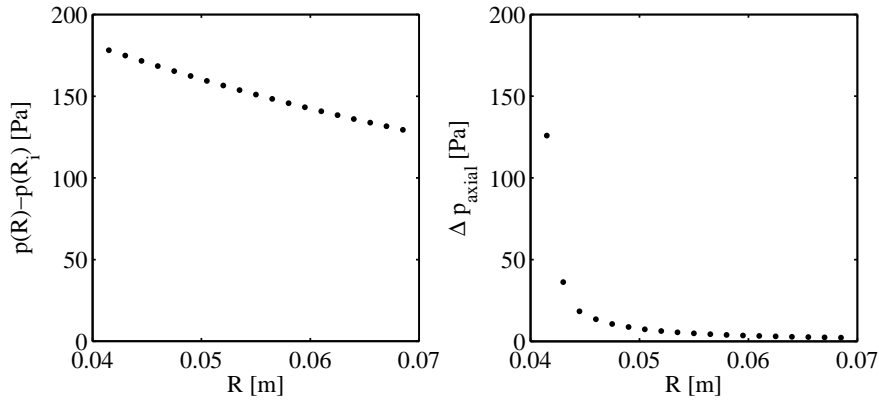


Figure 5.5. Radial pressure difference and axial pressure drop as a function of outer filter radius.

To minimise the leakage flow between the filter and the casing, the gap between these two has to be very small compared to the main throughput area of the filter. With standard production technology we are able to produce an RPS with a gap as

small as 0.1 mm between filter and casing. The axial pressure drop over this gap is equal to that of the pressure drop over the filter channels, which is 126 Pa, so that the flow through this gap is depending on the liquid fraction in the mixture there. Other design possibilities would be spiral grooves in the casing such that the gap between the filter and casing is pumped empty or two labyrinth seals, one near the inlet and one near the outlet of the filter. Such solutions would require elaborate calculations (and therefore time) and since leakage through the small gap is only minimal they will not be used. If wall friction in this gap becomes a problem during the measurements, then the design allows for future alterations of the RPS.

Since the final filter design has only one row of channels, it is not necessary to use the corrugated sheet metal production method of Duis Engineering B.V. The simplest method of producing the current filter design is by milling the 1.5 mm deep channels in an solid axle of 83 mm and welding a wall, consisting of a 85 mm outer radius / 1 mm thickness cylinder, around it. This results in a filter with inner diameter 80 mm and outer diameter 83 mm, which will rotate at a speed of 2700 rpm. The production of this filter (and also the whole RPS!) is carried out by the Thermo Fluids Engineering workshop at Eindhoven University.

5.2.4 Geometric design

Type selection and geometric considerations

There are three types of RPS that can be considered standard, i.e. models that have been built multiple times for multiple conditions. Two types are based on radial cyclone designs and can be mounted in such a cyclone; the so-called type A and B RPS. Here the flow enters the RPS tangentially after which it swirls through a pre-separating cyclone. The filter element is mounted vertically in the top of the cyclone. Both types differ only in the fact that the B-type has a sealing impeller to counter leak flow around the filter. The third type is the axial in-line version as described in chapter 4 and built by for instance Mondt [34]. Since one of the operational requirements is that the filter element is actively driven by a motor, it would be impractical to use the axial design. Also, the piping leading to the RPS is DN15 (18x1) which is considerably smaller than the filter element with a diameter of 85 mm. Getting the flow conditions right in an axial RPS for these dimensions would be very difficult. Therefore the separator is based on the radial RPS designs.

A second consideration is whether to mount the filter element vertically or horizontally. The liquid separating RPS is, as stated earlier, not a real separator, but more a coalescenser. The larger droplets breaking up from the liquid film leaving the RPS channels are separated in a pre- and post separator, similar to a cyclone, where the liquid is collected at the casing wall and where it has to be drained to leave the RPS. For this last step in the separation process it is useful to use gravity as a driving force for the separation mechanism. Putting the element in a vertical position ensures that liquid collected at the walls will flow downwards, so that it can be collected at the bottom of the device. A second benefit of putting the element vertically is that gravity pulls the liquid film in the channels of the filter elements downwards (Mondt [34]). If the gas is flowing upwards, and gravitational forces dom-

inate the force balance of the liquid film in vertical direction, this means that most of the liquid leaves the filter element in the direction of the pre-separator. Here the broken-off droplets are collected by centrifugation to the walls. However, if broken-off droplets are not collected and follow the gas stream, their size ensures that they are recaptured in the filter element. Droplets formed at the other end of the filter have to be collected by the post-separator; if this post-separator fails to collect a droplet, then that droplet will remain in the gas flow, which can be considered as an efficiency loss of the total separator. Therefore liquid film break-off in the direction of the pre-separator is preferred. One way to promote that is by putting the element vertically whereby the gas flows in the upwards direction. This is also the configuration that is used for the current prototype.

Dimensions of in- and outlets

Apart from the obvious gas in- and outlet, there are also two liquid outlets required; one for the pre-separator and one for the post-separator. All these channels are dimensioned such that they can handle the design. Also, the gas inlet has to be dimensioned such that there is not a large mismatch in velocity relative to the tangential velocity of the filter. In the DN15 channel leading to the RPS the axial velocity of the gas is approximately 1,4 m/s, the tangential velocity of the filter at the design speed is 11,8 m/s, and the maximum design velocity of the filter is 26 m/s. This means that the gas flowing tangentially in the RPS has to be accelerated from the velocity in the piping to the filter velocity. In this case, we achieve this by narrowing the inlet; the area through which the gas flows reduces in the inlet from $2,01 \cdot 10^{-4} \text{m}^2$, i.e. equal to that of the gas piping, to $2 \cdot 10^{-5} \text{m}^2$ – a rectangular channel with a height of 10 mm and a width of 2 mm. The resulting inlet gas velocity is approximately 14,2 m/s, which is slightly higher than the filter velocity.

The gas outlet is less sophisticated; it starts as a hole with a diameter of 8 mm ($v \sim 6 \text{ m/s}$), in tangential direction, and expands to the diameter of the gas piping. Flow mismatch is not a problem here since the separation process is done here and a mismatch can only result in a slightly higher pressure drop – pressure is abundant at this stage.

Since beforehand it is unclear what the liquid distribution between the pre- and post-separator will be, it is necessary that both liquid outlets are designed such that they are able to handle the full liquid flow that can be separated in the RPS, i.e. $0,034 \text{ m}^3/\text{h}$, at a relatively low pressure drop. We use 10x1 pipes for the liquid outlets, resulting in a maximum possible axial velocity of 0,19 m/s; pressure drop will be less than 50 Pa.

Pre- and post-separator

The pre- and post-separators are basically axial cyclones that have the function of collecting the droplets exiting the RPS-channels. In this design the axle fills, due to the one-channel design, most of the pre- and post-separator volume; the particles only have to travel a maximal 2,6 mm (channel height + filter wall thickness + gap size) to reach the wall. In chapter 4 simple equations are stated for estimating the

performance of an axial cyclone. Using eq. (4.4) and the geometry data of section 5.2.3 we see that a 10 mm long pre- or post-separator can already collect particles of 1,6 μm with 50 % probability. Also, a droplet of 10 μm would only travel 0,3 mm before reaching the wall. Particles leaving the RPS-channels are generally up to an order of magnitude larger [34], so a rather short pre- and post-separator length of 10 mm is sufficient to collect all liquid exiting the channels.

Casing

The casing of the RPS houses the axle-filter element and incorporates the pre- and post-separators and gas and liquid connections. It also serves as a pressure vessel and thermally isolates the separation process from the environment. It is chosen to use a thick-walled cylinder with flanges with a thickness of 20 mm. Simple Hook-law based stress calculations indicate that this thickness greatly exceeds the requirements for a pressure vessel of this size, but the thickness is useful to make a simple connection of the flanges at the top and bottom end of the cylinder. The flanges are solid discs that are screwed directly in the casing cylinder. The seals are mounted in between. Vacuum insulation around the cylindrical part of the casing prevents heat from entering the RPS. The lower flange is wrapped in 3 cm thick Armaflex™. The upper flange is for now not insulated; if necessary, Armaflex can be added later.

Due to the vertical configuration of the RPS, liquid collected at the walls of the pre- and post-separator will flow downward due to gravity – axial gas velocity is too low to pull the liquid film upward [34]. In the pre-separator the liquid then flows toward the bottom of the RPS where it is drained through a hole in the bottom flange. The liquid collected by the post-separator will flow back towards the filter where it could flow in the gap between filter and casing, where it can cause large friction and thus heat by dissipation. To prevent this, the filter wall is made with a outward protruding edge on the top side, see figure 5.6. Liquid exiting the filter is now centrifuged over this edge towards the wall, where it flows downward. Together with a larger wall diameter and a slot in the casing this prevents liquid from flowing downwards in the gap.

5.2.5 Mechanical drive

The mechanical drive consists of two components; a motor and a coupling or transmission to the axle. For the size of equipment and rotational speeds we are looking at it is normally possible to mount a DC-electro motor directly on the axle. However, in this case the relatively high internal pressure, combined with the presence of liquid CO₂ and the high sliding velocity that would occur in a seal make it impossible to use a conventional sealing design where an axle penetrates the casing (according to ERIKS and SKF). Therefore a magnetic coupling is used; this is currently commercially available –i.e. standard – technology and is therefore easily applicable in the current design. A magnetic coupling enables us to make a design where no dynamic seals are present, only static seals between the various flanges are required. This also ensures more reliable, leakage free, operation of the unit.

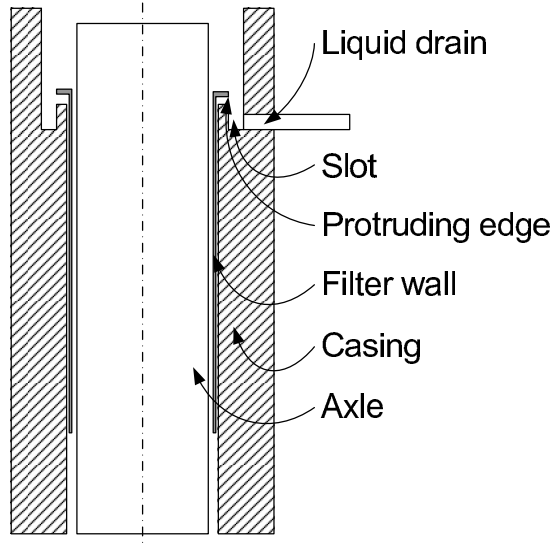


Figure 5.6. Schematic of the liquid drain system of the post-separator, not to scale.

The size and/or type of motor and coupling are fully determined by the power requirements; the rotational speed of 2700 rpm is rather conventional. These power requirements of the motor and coupling are in turn a function of two parameters: the power requirement for steady-state operation and that for start-up of the unit. First we discuss the power requirements during steady-state operation.

Power requirements in steady-state operation

The power requirements during steady-state operation are dominated by turbulent friction losses between the filter and the casing and between the axle and the casing; bearing friction can be neglected. The resulting momentum loss can be calculated by taking the momentum required to turn a cylinder in a static housing [37]:

$$G_{gap} = 0,5\pi C_m \rho_f \Omega^2 R_{cylinder}^4 L_{gap}, \quad (5.9)$$

where G_{gap} is the momentum loss in the gap (Nm), and C_m the torque coefficient, which for turbulent flow ($Ta > 400$) is related to the Taylor number as:

$$C_m = 0,019886 Ta^{-0,2} \quad (5.10)$$

The Taylor number is here defined as:

$$Ta = \frac{\rho_f \Omega}{\mu_f} R_{cylinder}^{\frac{1}{2}} s_g^{\frac{3}{2}}, \quad (5.11)$$

where s_g is the radial spacing between the cylinder and the static housing (m). There are now three possible situations: the gap is filled with liquid, with gas or with a

two-phase gas/liquid mixture. For the last situation it is complicated to compute the filter-torque, but the result will be an intermediate value between the extremes of liquid-filled gap (upper torque limit) and gas-filled gap (lower torque limit). Therefore only the values for the first two situations will be evaluated. Figure 5.7 shows the momentum loss or filter torque for both cases. It can be seen that for the standard situation of $\Omega \simeq 2700$ rpm the filter torque will be 0,025 Nm in the gas-filled case and maximally 0,5 Nm for the liquid-filled case. The power requirements will then respectively be 7 and 140 W, which should be no problem for a small DC-motor. However, since all this power is dissipated in the fluid between the filter and the casing, this also means that when the gap is fully filled with liquid approximately 150 W of dissipative heat is generated. Although this should not be an inevitable problem, see section 5.2.2, it is best to avoid to much heat generation. Later on we will discuss countermeasures that have been taken to avoid liquid filling the gap between filter and housing.

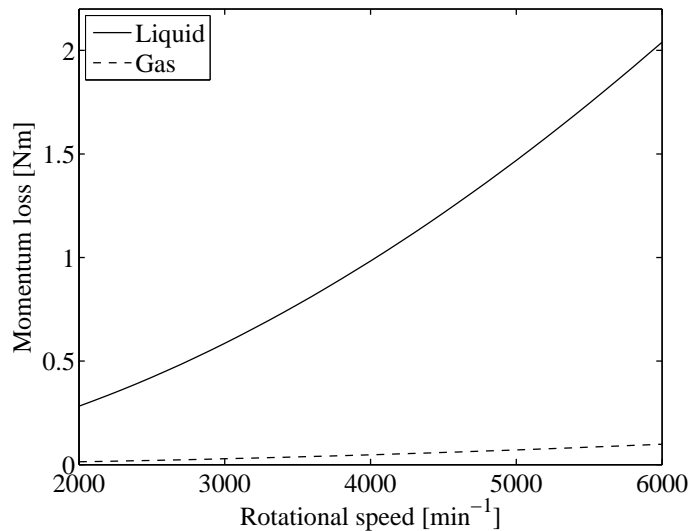


Figure 5.7. Momentum loss due to friction in the gap between the filter and the casing. Gap is fully filled with either liquid or gas.

Power requirements during start-up

The mechanical drive of the RPS prototype is schematically depicted in figure 5.8. The differential equation describing the angular velocity as a function of motor torque, T_M , and the load momentum, T_F is [33]:

$$\frac{\pi}{2} \rho L R^4 \frac{d\Omega}{dt} = (T_M - T_F), \quad (5.12)$$

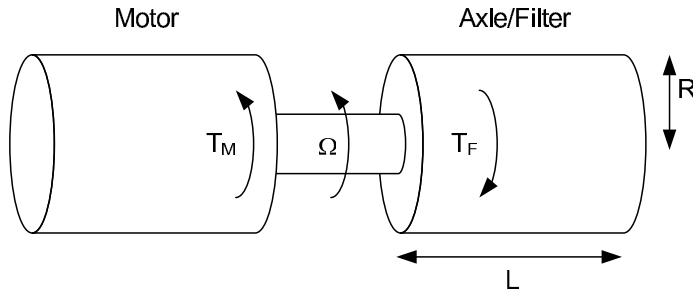


Figure 5.8. Schematic of the mechanical drive of the RPS.

where ρ is the density, R the radius (m) and L the length (m) of the cylindrical load, in this case the axle/filter combination, and Ω the angular velocity (rad/s). The load momentum is equal to the wall friction, which can be calculated using eq. 5.9 and is a function of angular velocity. The continuous torque that an electric motor can deliver is fairly constant over a large range of angular velocities. The power that an electric motor delivers is equal to:

$$P_M = T_M \Omega \quad (5.13)$$

The available power at low angular velocity is thus very low. However, during start-up or short-term operation electric motors can temporarily deliver a torque that is more than ten times higher, and thus 10 times more power, without damaging the motor [33]. This means that a motor with a continuous torque of $T_m \sim 0.5$ Nm spins up the RPS in circa 10 seconds to the operational speed of 2700 rpm, with the gap between filter and casing fully filled with liquid. If the gap is fully filled with gas, then start-up will take even less time; quite acceptable for task the RPS is designed for: experiments. Normally start-up of an RPS takes minutes [34], now quick start-up enables us to alter experimental settings fast.

Motor and magnetic coupling

A Maxon EC45 motor is used to power the RPS. This is a 48 V, 250 W brushless DC motor with a maximal continuous speed of 6000 rpm. This motor is able to power the RPS at design conditions with the gap between the filter and casing fully filled with liquid. In the more desirable case were no liquid is present there, the motor can easily achieve a continuous operation of the RPS at 6000 rpm. The magnetic coupling is a type MAKX-40-2/12-EX of Burgmann Industries. This is a scaled down version of a larger unit, which was custom built for us. It consist of three parts:

1. a small magnet that is mounted on the filter axle,
2. a can that is mounted on the casing, enclosing the inner magnet and sealing the casing, and surrounding this can,

3. a outer magnet that is coupled to a motor and which tows the inner magnet and thus the filter as it is rotated.

The can is made from polyetheretherketone (PEEK) to prevent a hysteresis current, which could lead to heat generation. The magnetic coupling can transfer a torque of 30 Nm, which is an order of magnitude more than required.

Bearings

Conventional roller-bearings are suitable in terms of load and rotational speed. However, they also require lubrication, which requires internal sealing to prevent lubricant from entering the system. In order to prevent this situation, full ceramic ball bearings are applied; they can run more than 100 hours without any lubrication. Since this RPS is part of an experimental unit with typically short runs, long lifetime of bearings is not a requirement – bearings can simple be replaced between experiments. The bearings are also supplied by Burgmann Industries.

Sealing

As stated above, only stationary seals are required in this RPS. A conventional o-ring design is used at the flanges. However the common NBR o-ring type is not applicable, because it is not suitable for temperatures below $T = -25^{\circ}\text{C}$. Just as most other types of o-rings NBR becomes brittle at low temperatures. Therefore a silicon based o-ring is used; a TEFLEX-silicon o-ring supplied by ERIKS BV. This is a silicon o-ring with a PTFE outer layer. The silicon stays elastic down to $T \sim -70^{\circ}\text{C}$, the teflon gives the o-ring chemical resistance to the methane gas and CO₂-rich liquid.

5.2.6 Final design

Figures 5.9 and 5.10 show the final result of this design effort; figure 5.9 shows a three dimensional exploded assembly drawing and figure 5.10 shows the unexploded assembly. The axle/filter is figure 5.9 the rather large cyan part and the filter wall is the dark red part directly above it. The casing consists of the partially transparent white parts in figure 5.9. Above that the coupling magnets (orange), coupling casing / can (yellow), and the motor (gray/black) are displayed.

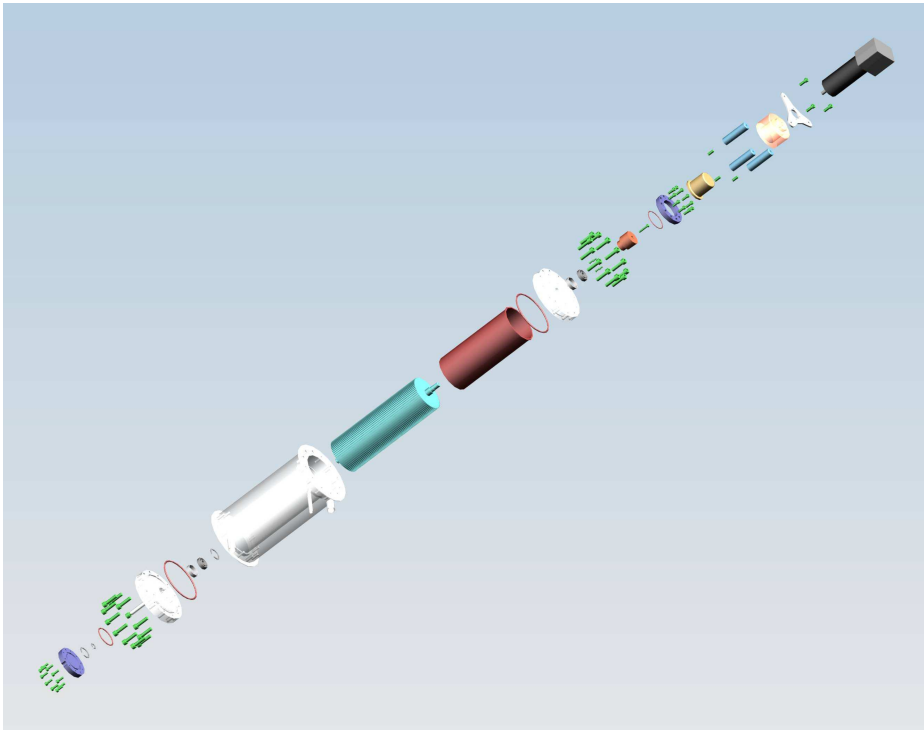


Figure 5.9. Exploded view construction drawing of the 60 nm³/h RPS prototype.

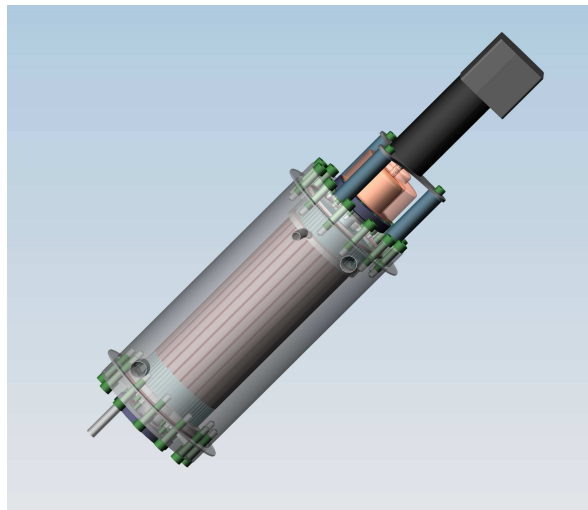


Figure 5.10. 3D construction drawing of the 60 nm³/h RPS prototype.

Chapter 6

Discussion

6.1 Concept development

The objective of this study was to develop a centrifugal separation method for removing CO₂ and/or H₂S from natural gas streams. Initially attention was focussed on the concept of gas centrifugation. A counter-current gas centrifuge can clean up a contaminated natural gas stream in a single production step. However, the production rates of such a gas centrifuge are extremely low. At lower enrichment levels, which also requires multiple separation stages, production rates are higher, but still very low – millions of centrifuges are required to handle a large gas well.

The process of gas centrifugation is accelerated by operating at a pressure such that during operation condensation occurs at the wall. This works in two ways: during start-up, pressure increases in the outer radii of the centrifuge until the dewpoint is reached and CO₂ starts to condense. Secondly, the concentration gradient across the centrifuge radius is larger (compared to a conventional gas centrifuge), resulting in a faster diffusion process. The first process is actually pure compression work, which can be done more efficiently with a conventional compressor and heat-exchanger. The second process only occurs in a gas centrifuge. The latter process is examined in this work, and it is shown that it leads to a doubling of the production rate. However, the production rates are still far too low.

So although a contaminated gas stream can be cleaned by gas centrifugation, the required capital investment to manufacture the equipment is simply too high – or the value of the gas too low. Gas centrifugation is a technology that is only interesting for application in the separation of materials with very high economic value, such as in the case of uranium enrichment.

A much faster process is Condensed Contaminant Centrifugal Separation (C3-sep). Here a contaminated well gas stream is compressed and cooled to high pressure (> 100 bar) and ambient temperature (or lower). This gas is then integrally cooled down by expansion in a turbine such that the contaminants condense in the form of droplets. These droplets are removed using the new technology of the rotational particle separator (RPS). In this thesis, the thermodynamics and droplet formation

and separation of the C3-sep process are discussed, as well as the design of a small scale prototype of the C3-sep process.

6.2 Optimal operation

From the thermodynamic evaluation we learn that (in theory) C3-sep is a bulk separation method. Removal of the contaminants up to ppm level is not possible with this method. Separation is based on liquid phase formation, and there will always be a part of the contaminants that remains gaseous. Nevertheless, the enrichment that can be achieved in one operation step, i.e. one C3-sep system, is very high. With a single C3-sep system it is possible to enrich a 50/50 CH₄/CO₂ gas stream to a 78/22 product stream. Also, the flow rates of full scale production are not a problem for implementation of C3-sep. So although it will not be able to fully replace the existing technology, it can be used to access gas fields that are currently too contaminated for production. It can remove the bulk of the contaminants in these fields in a very energy and thus cost efficient way.

The current state of RPS technology only enables removal of liquid droplets from the cold stream coming out of the turbine. Solid particle removal has been the traditional operational field of the RPS [15], but in this case the amount of solids that is to be separated, i.e. the solid 'flow rate', is much higher. Normally the captured solid particles remain in the filter element until this element is periodically cleaned (with a nozzle). In the C3-sep case that would mean that the channels fill up with solid waste in a very short time – the mass flow rate of contaminants is typically larger than 10 kg/s. So until the RPS is enhanced such that it can handle large amount of solids, it is best to operate C3-sep in the liquid regime.

Although the majority of this work is focussed on the separation of CO₂ from CH₄, for initial industrial application it is better to focus on gas fields that are contaminated with H₂S or a combination of CO₂ and H₂S. About half of the heavily contaminated fields known today fall in this category. The enrichment of a CH₄/CO₂ stream above 88/12 CH₄/CO₂ in the product stream is very difficult, since it would require going into the solid separation regime. With H₂S present this can be avoided and enrichment can be such that the product stream contains more than 95 % CH₄; high enough to further purify the gas stream with conventional technology. For the experimental 'proof-of-concept' of C3-sep it is still sufficient to work with CH₄/CO₂ mixtures, as this is less hazardous than operation with the poisonous H₂S.

An item that has not been investigated in this work is the influence of other components in the gas stream on the separation process. Apart from CH₄, CO₂, and H₂S, natural gas also contains water and higher hydrocarbons (C2+). The dewpoint and freezing point temperatures of these components are usually higher than that of CO₂; they condense or freeze out early in the expansion and droplet formation process. The amount of water vapour that natural gas contains is 3 % or lower. This water forms hydrates when in contact with methane at low temperatures. A quick estimate using the homogeneous heterogeneous nucleation theory (see chapter 3) indicates that this hydrate formation can clog up the separator channels in a matter of seconds. It is therefore essential that all water in the natural gas is removed prior to the C3-sep

process. The effect of the presence of higher hydrocarbons, though not investigated, is probably similar. Therefore it is best to remove these components from the gas stream as well.

A C3-sep prototype is designed and built that can handle a 50/50 CH₄/CO₂ flow of 60 nm³/h (=0.022 kg/s). Due to delays in the construction process it is unfortunately not possible to report results from experiments with this prototype in this thesis.

Bibliography

- [1] 'BP annual report 2005'.
- [2] 'EDIN-GIS database'. <http://energy.ihs.com/Products/Edin-Gis/index.htm>.
- [3] 'ExxonMobil summary annual report 2005'.
- [4] 'Royal Dutch / Shell Group annual report 2005'.
- [5] Astarita, G., D. W. Savage, and A. Bisio: 1983, *Gas Treating with Chemical Solvents*. Wiley, Network.
- [6] Auvil, G. and B. W. Wilkinson: 1976, 'The steady and unsteady state analysis of a simple gas centrifuge'. *A.I.Ch.E. Journal* **22**(3), 564–568.
- [7] Beams, J. W. and C. Skarstrom: 1939, 'The concentration of isotopes by the evaporative centrifuge method'. *Physical Review* **266**, 56.
- [8] Bird, R. B., W. E. Stewart, and E. N. Lightfoot: 1960, *Transport phenomena*. Wiley, New York.
- [9] Brouwers, J. J. H.: 1976, 'On the motion of a compressible fluid in a rotating cylinder'. Ph.D. thesis, Twente University of Technology.
- [10] Brouwers, J. J. H.: 1978a, 'On compressible flow in a gas centrifuge and its effect on the maximum separative power'. *Nuclear Technology* **39**, 311–322.
- [11] Brouwers, J. J. H.: 1978b, 'On compressible flow in a rotating cylinder'. *Journal of Engineering Mathematics* **12**(3), 265–285.
- [12] Brouwers, J. J. H.: 1990, 'Rotational particle separator'. *Europ. patent 0.286.160*.
- [13] Brouwers, J. J. H.: 1991, 'Rotational particle separator'. *US Patents 4.994.097 and 5.073.177*.
- [14] Brouwers, J. J. H.: 1996, 'A new method for separating fine particles and mists from gases'. *Chemical Engineering Technology* **19**, 1.
- [15] Brouwers, J. J. H.: 1997, 'Collection efficiency of the rotational particle separator'. *Powder Technology* **92**(5), 89.

- [16] Brouwers, J. J. H.: 2002, 'Phase separation in centrifugal fields with emphasis on the rotational particle separator'. *Experimental Thermal and Fluid Science* **26**(2-4), 325.
- [17] Brouwers, J. J. H., R. J. E. van Wissen, and M. Golombok, 'Novel centrifugal process to access contaminated gas reserves'. accepted for publication in *Oil & Gas Journal*.
- [18] Brunner, T., I. Obernberger, J. J. H. Brouwers, and Z. Preveden: 1998, 'Efficient and economic dust separation from flue gas by the rotational particle separator as an innovative technology for biomass combustions and gasification plants'. In: *Proc. of the 10th European Bioenergy Conference*.
- [19] Cohen, H., G. F. C. Rogers, and H. I. H. Saravanamuttoo: 1996, *Gas turbine theory*. Pearson education, Essex.
- [20] Cohen, K. P.: 1951, *The Theory of Isotope Separation as Applied to the Large-Scale Production of U-235*. McGraw-Hill, New York.
- [21] Cracknell, R. and M. Golombok: 2004, 'Monte Carlo simulations of centrifugal gas separation'. *Molecular Simulations* **30**(8), 501.
- [22] Friedlander, S. K.: 2000, *Smoke, dust, and haze: fundamentals of aerosol dynamics*. Oxford University Press, New York, 2nd edition.
- [23] Golombok, M. and K. Bil: 2005, 'Removal of CO₂ from a gas stream using an experimental centrifuge'. *Industrial and Engineering Chemistry Research Design* **44**(13), 4721.
- [24] Golombok, M. and L. Chewter: 2004, 'Centrifugal separation for cleaning well gas streams'. *Industrial and Engineering Chemistry Research Design* **43**(7), 1734.
- [25] Golombok, M. and C. Morley: 2004, 'Thermodynamic factors governing centrifugal separation of natural gas'. *Chemical and Engineering Research Design* **82**(A4), 513.
- [26] Groth, W. and K. Beyerle: 1961, *Separation of Isotopes*. George Newnes, London.
- [27] Heywood, J. B.: 1997, *Internal combustion engine fundamentals*. McGraw Hill, London.
- [28] Hinds, W. C.: 1982, *Aerosol technology*. Wiley, New York.
- [29] Kohl, A. L. and R. B. Nielsen: 1997, *Gas Purification*. Gulf, Houston.
- [30] Los, J.: 1963, 'De scheiding van zware isotopen in een centrifugaal veld'. Ph.D. thesis, Leiden University.
- [31] Luijten, C. C. M.: 1998, 'Nucleation and droplet growth at high pressure'. Ph.D. thesis, Eindhoven University of Technology.

-
- [32] Maddox, R. N. and D. J. Morgan: 1998, *Gas conditioning and processing. Vol. 4: Gas Treating and Sulfur Recovery.*, Campbell Petroleum Series. Norman, USA.
- [33] Mohan, N.: 2003, *Electric drives 'an integrative approach'*. MNPERE, Minneapolis.
- [34] Mondt, E.: 2005, 'Compact centrifugal separator of dispersed phases'. Ph.D. thesis, Eindhoven University of Technology.
- [35] Olander, D. R.: 1981, 'The theory of uranium enrichment by the gas centrifuge'. *Progress in Nuclear Energy* **8**(1), 1.
- [36] Pratt, H. R. C.: 1967, *Countercurrent Separation Processes*. Elsevier, Amsterdam.
- [37] Schlichting, H.: 1979, *Boundary-layer theory*. McGraw-Hill, New York.
- [38] Seader, J. D. and E. J. Henley: 1998, *Separation process principles*. Wiley, New York.
- [39] Shavit, A. and C. Gutfinger: 1995, *Thermodynamics: from concepts to applications*. Prentice Hall, London.
- [40] Steenberg, W.: 1995, 'Turbulent pipe flow with swirl'. Ph.D. thesis, Eindhoven University of Technology.
- [41] Svarovsky, L.: 1984, *Hydrocyclones*. Holt, London.
- [42] van Kemenade, H. P., E. Mondt, A. J. A. M. Hendriks, and P. H. J. Verbeek: 2003, 'Liquid-phase separation with the rotational particle separator'. *Chemical Engineering Technology* **26**(11), 1176.
- [43] van Wissen, R. J. E., J. J. H. Brouwers, and M. Golombok, 'In-line separation of dispersed phases'. submitted to A.I.Ch.E. Journal.
- [44] van Wissen, R. J. E., M. Golombok, and J. J. H. Brouwers: 2005, 'Separation of carbon dioxide and methane in continuous countercurrent gas centrifuges'. *Chemical Engineering Science* **60**, 4397–4407.
- [45] Williams, L. O.: 1980, 'Application of centrifugal separation to the production of hydrogen from coal'. *Applied Energy* **6**, 63.

Appendix A

Formulas for equipment dimensions

A.1 Cyclone

Volume:

$$V = Q\tau = \pi R^2 L \quad (\text{A.1})$$

Length:

$$L = \frac{1}{2} \varepsilon^{\frac{1}{2}} \tau \quad (\text{A.2})$$

Radius:

$$R = 2^{\frac{1}{2}} \pi^{-\frac{1}{2}} Q^{\frac{1}{2}} \varepsilon^{-\frac{1}{4}} \quad (\text{A.3})$$

Tangential velocity:

$$v_{t0} = \varepsilon^{\frac{1}{2}} \quad (\text{A.4})$$

Axial velocity:

$$v_{ax} = \frac{1}{2} v_{t0} = \frac{1}{2} \varepsilon^{\frac{1}{2}} \quad (\text{A.5})$$

A.2 RPS

Volume:

$$V = Q\tau = \pi R^2 (1 - \delta^2) L \quad (\text{A.6})$$

Length:

$$L = \left(\frac{2d_c \tau^2 \varepsilon}{7f} \right)^{\frac{1}{3}} \quad (\text{A.7})$$

Radius:

$$R = \left(\frac{7}{2} \right)^{\frac{1}{6}} \pi^{-\frac{1}{2}} (1 - \delta^2)^{-\frac{1}{2}} f^{\frac{1}{6}} d_c^{-\frac{1}{6}} Q^{\frac{1}{2}} \varepsilon^{-\frac{1}{6}} \tau^{\frac{1}{6}} \quad (\text{A.8})$$

Tangential velocity:

$$v_{t0} = \left(\frac{24\varepsilon}{7(1 + \delta^2)} \right)^{\frac{1}{2}} \quad (\text{A.9})$$

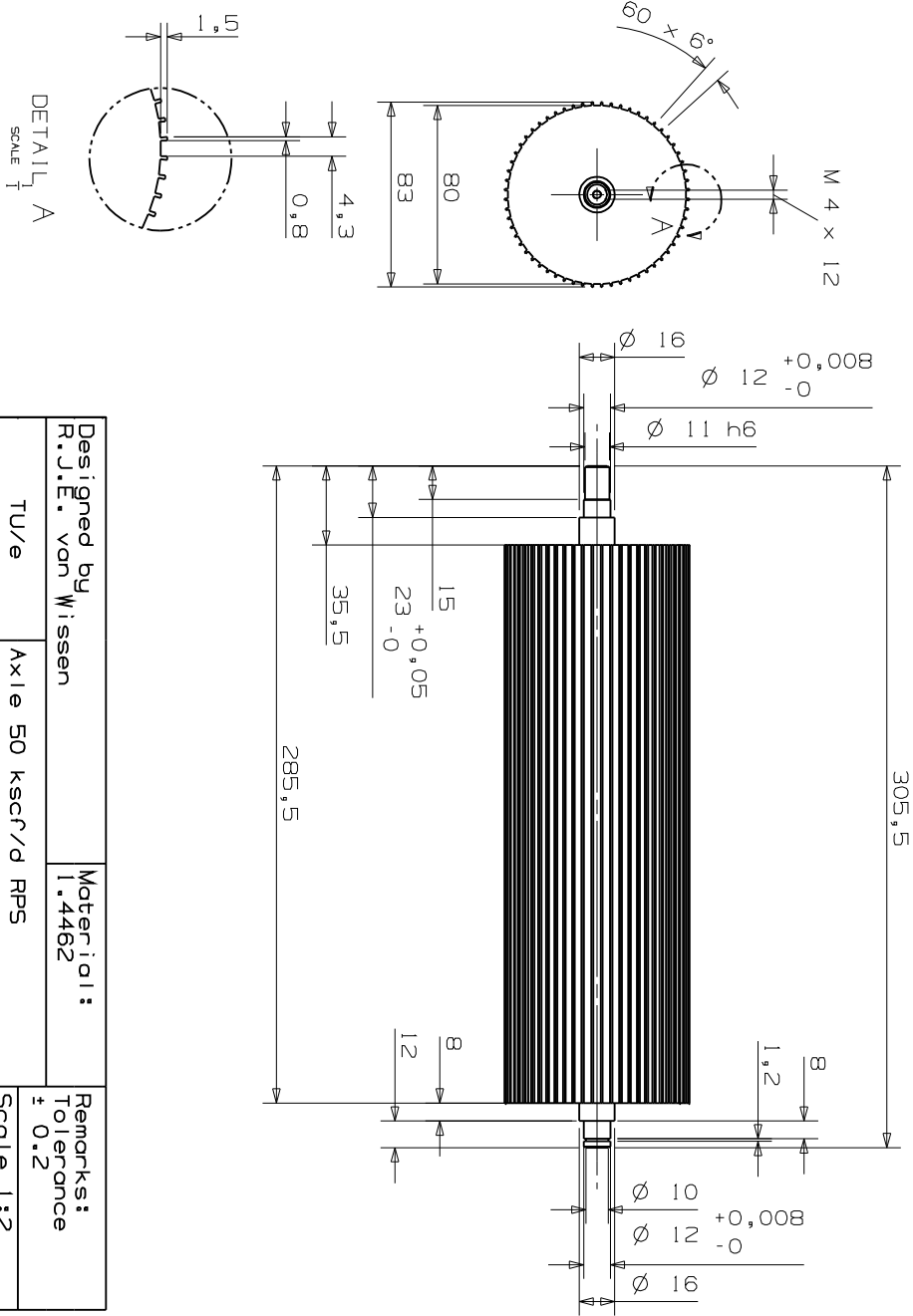
Axial velocity:

$$v_{ax} = \left(\frac{2d_c \varepsilon}{7f\tau} \right)^{\frac{1}{3}} \quad (\text{A.10})$$

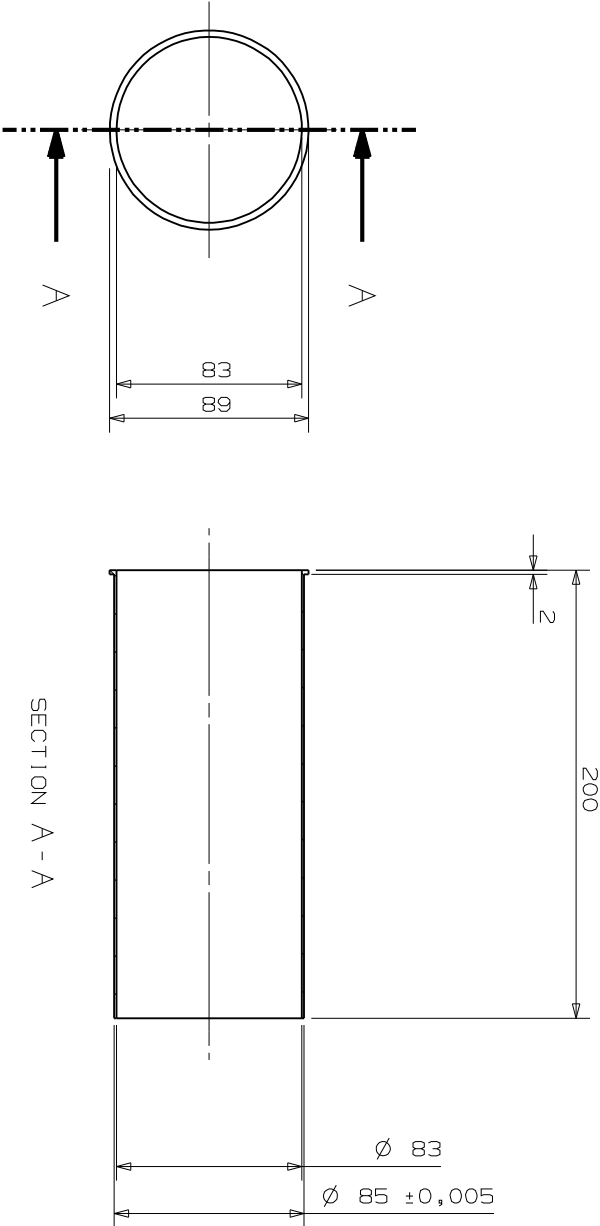
Appendix B

Construction drawings of the 60 nm³/h RPS prototype

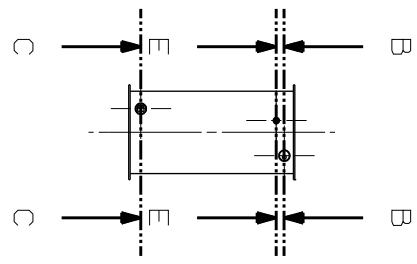
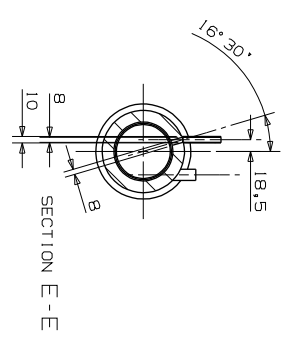
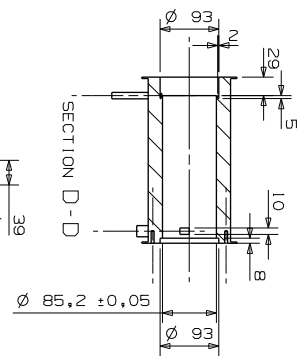
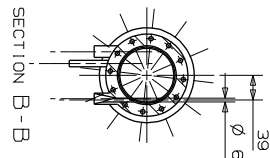
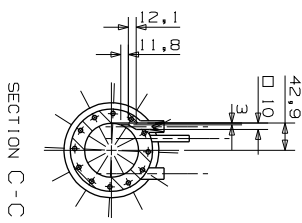
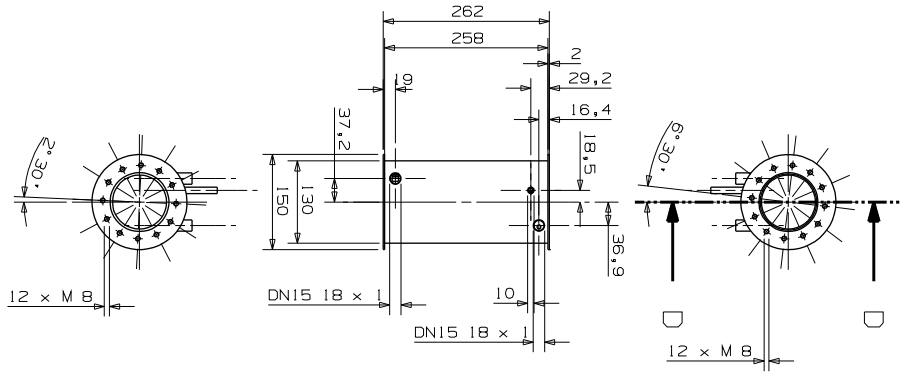
B.1 Part drawings



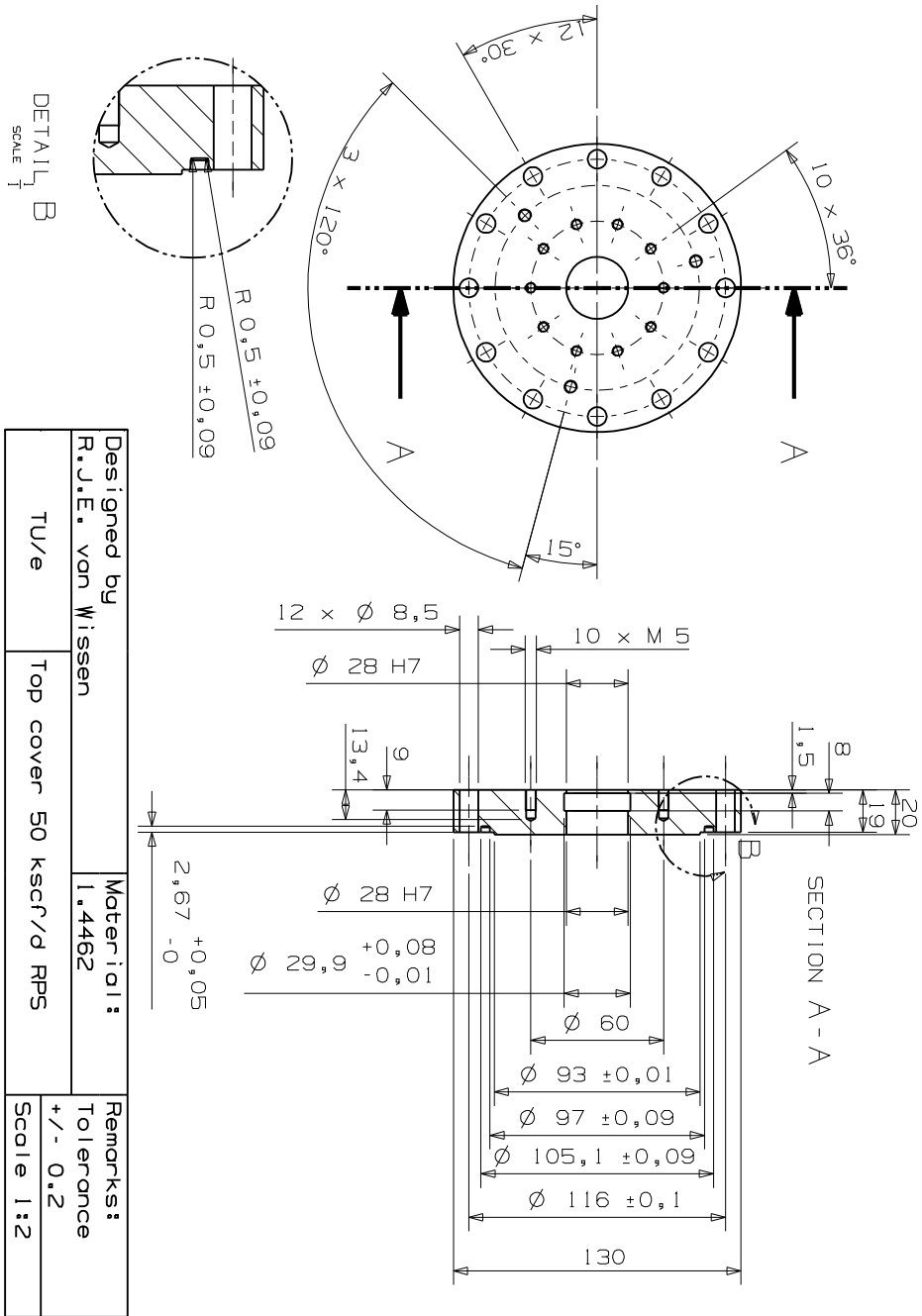
Designed by R.J.E. von Wissen		Material: 1.4462	
TU/e		Axle 50 kscr/d RPS	
		Remarks: Tolerance ± 0.2	
		Scale 1:2	



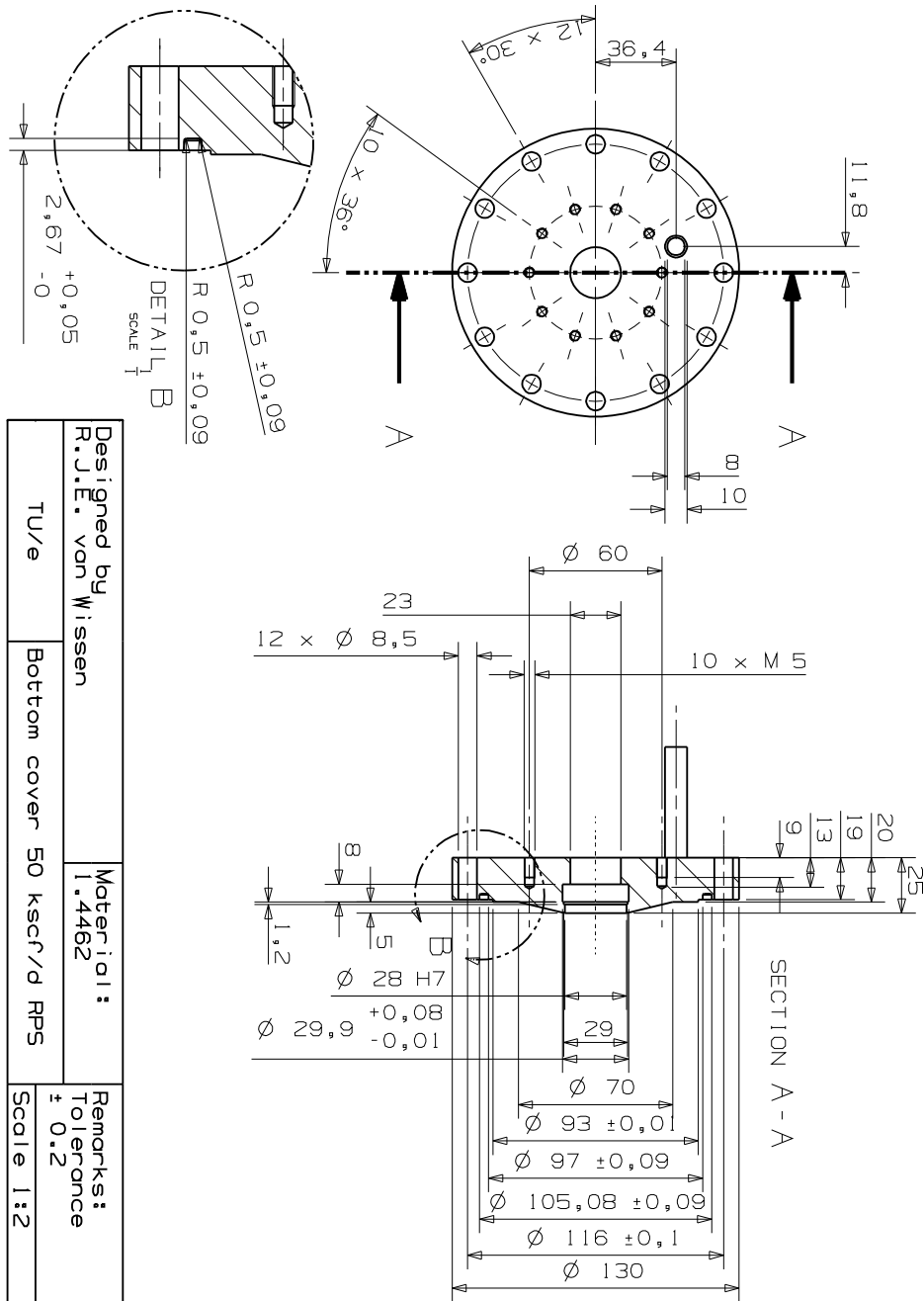
Designed by R.J.E. van Wissen	Material: 1.4462	Remarks: Tolerance ± 0.2
TU/e	Filter wall 50 kscr/d RPS	Scale 1:2



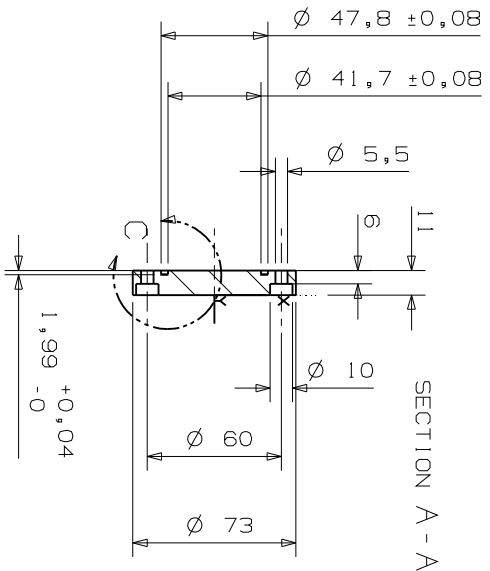
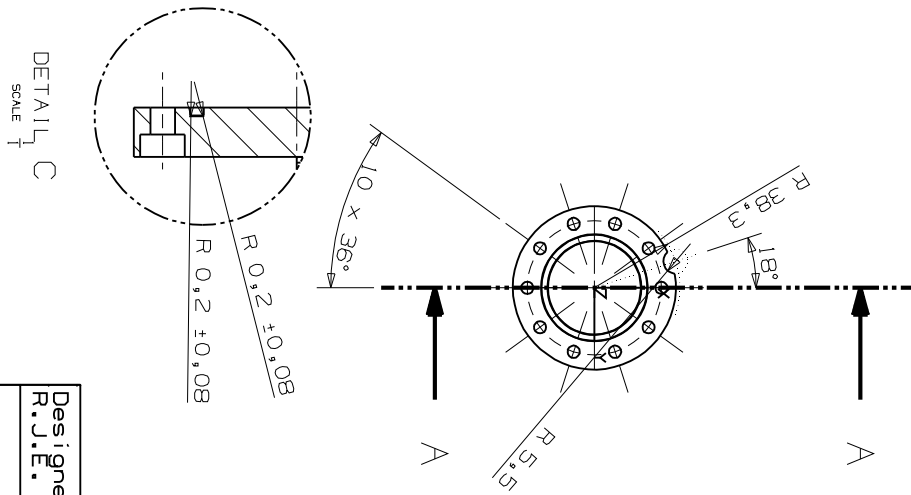
Designed by R.J.E. von Wissen	Material: 1.4462	Remarks: Tolerance ± 0.2
TU/e	Casing 50 kscf/d RPS	Scale 1:5



Designed by R.J.E. van Wissen	Material: 1.4462	Remarks: Tolerance +/- 0.2
TU/e	Top cover 50 kscr/d RPS	Scale 1:2

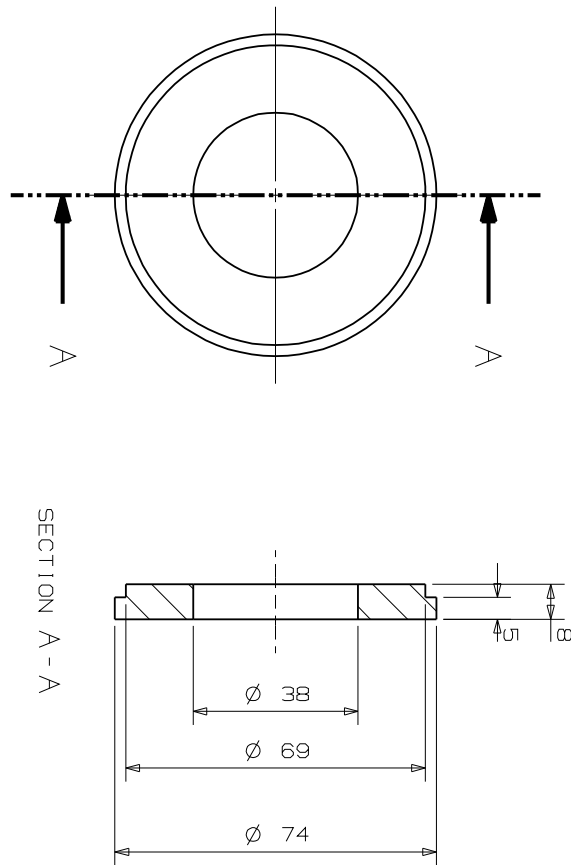


Designed by R.J.E. van Wissen	Material: 1.4462	Remarks: Tolerance ± 0.2
TU/e	Bottom cover 50 kscrf/d RPS	Scale 1:2

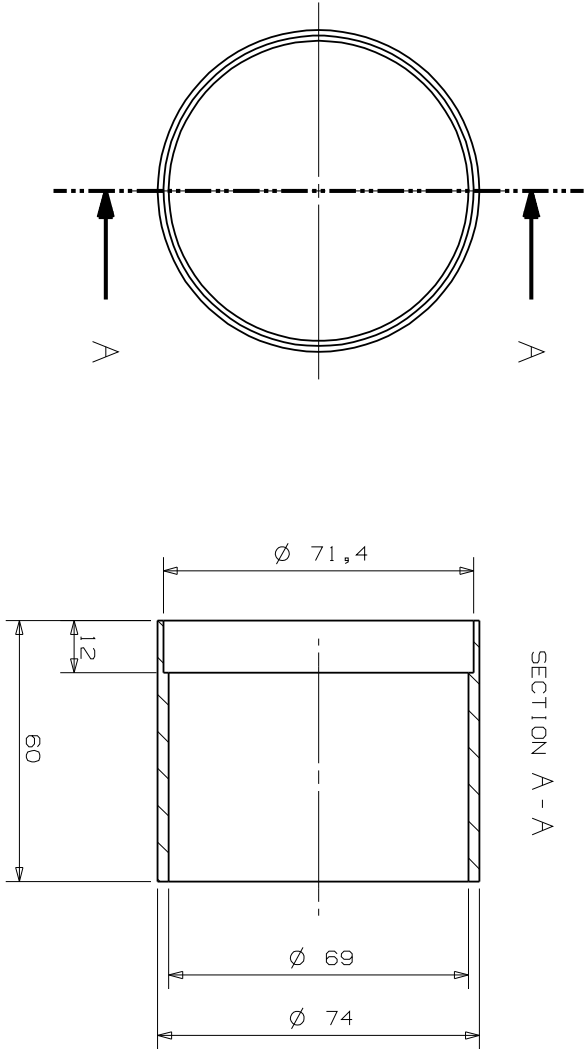


DETAIL C
SCALE 1:1

Designed by R.J.E. von Wissen	Material: 1.4462	Remarks: Tolerance $\pm 0,2$
TU/e	Bearing cover 50 kscr/d RPS	Scale 1:2

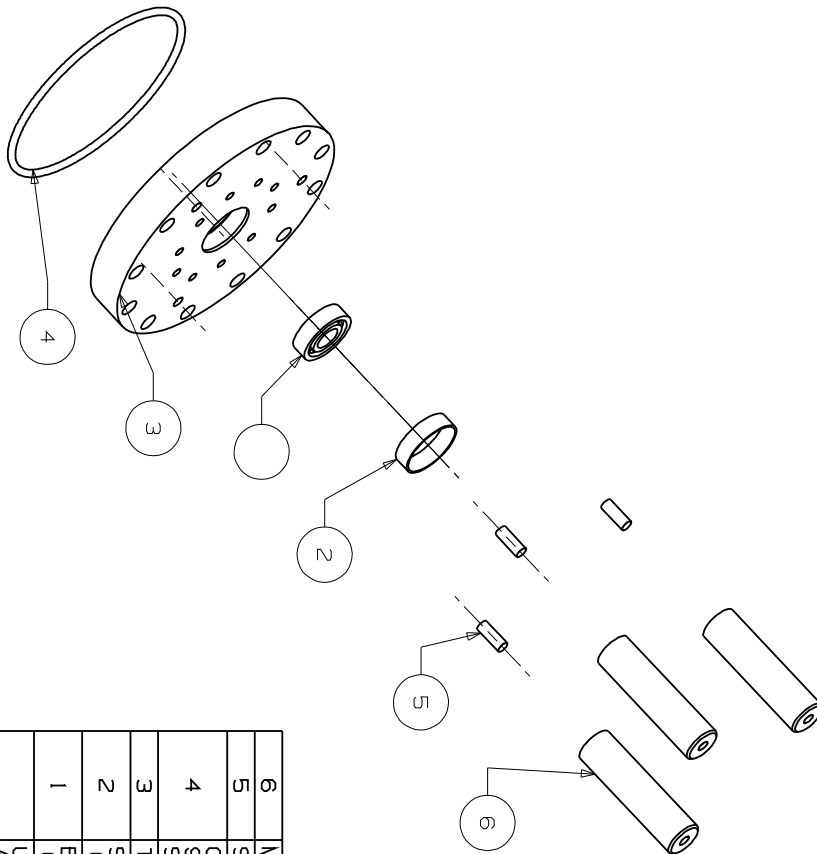


Designed by R.J.E. van Wissen	Material: PMMA	Remarks: Tolerance ± 0.2
TU/e	COUPLING COVER PLATE 50 Kscr/d RPS	Scale 1:2

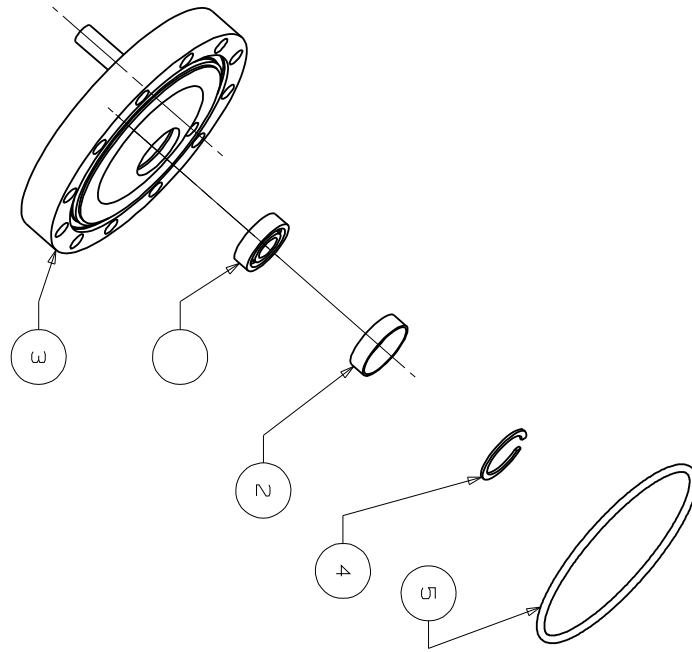


Designed by R.J.E. van Wissen	Material: PMMA	Remarks: Tolerance ± 0.2
TU/e	COUPLING COVER 50 kscr/d RPS	Scale 1:2

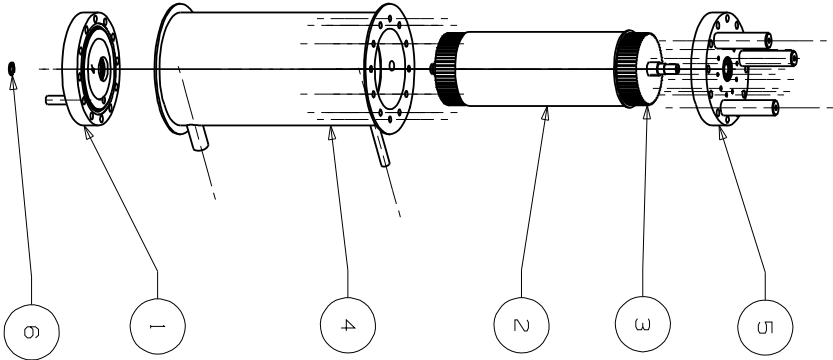
B.2 Assembly drawings



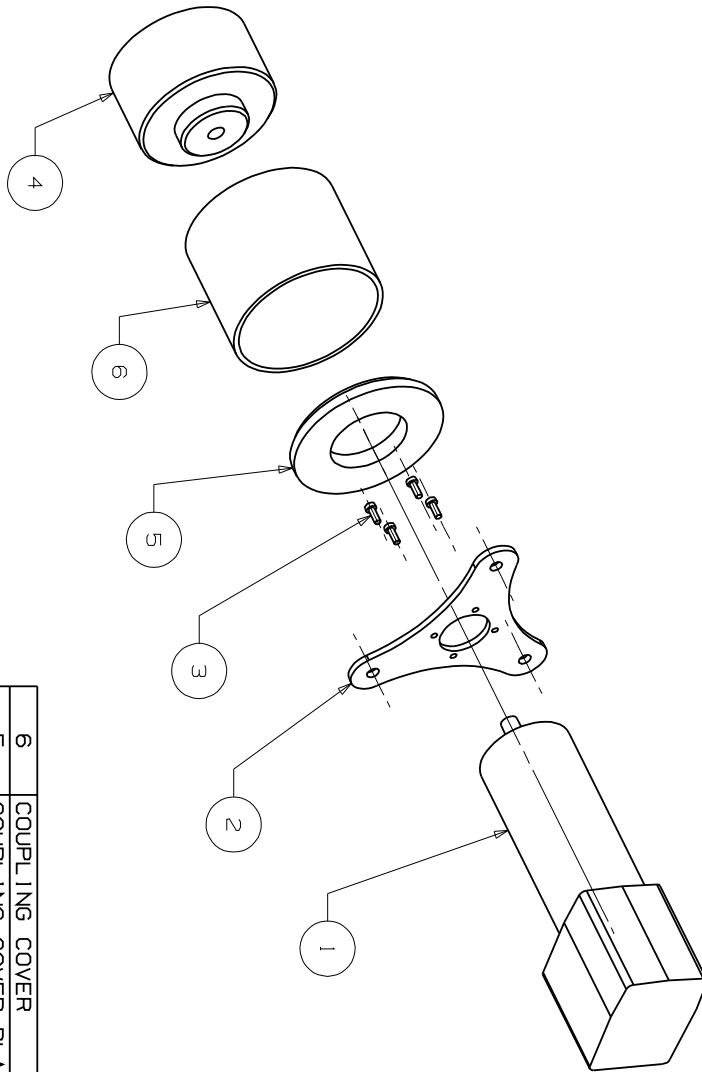
PC NO	PART NAME	QTY
6	MOTOR SUPPORT	3
5	STUD M6 x 15	3
4	O-RING 98.02x3.53 S:1/TEFLEX	1
3	TOP COVER	1
2	SPOOL PIECE (BURGMANN)	1
1	BALL BEARING (BURGMANN)	1
	UPPER BEARING ASSEMBLY	



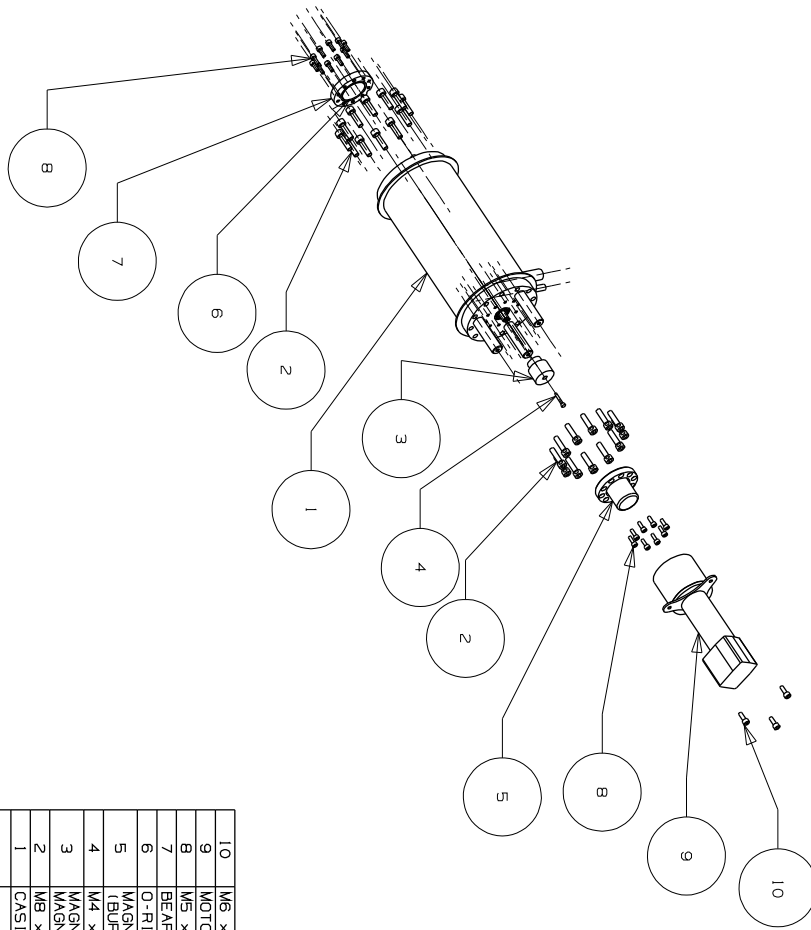
5	O-RING 98.02x3.53 SIL/TEFLEX	1
4	LOCK WASHER D_OUT = 29	1
3	BOTTOM COVER	1
2	SPOOL PIECE (BURGMANNI)	1
1	BALL BEARING (BURGMANNI)	1
	LOWER BEARING ASSEMBLY	
PC NO	PART NAME	QTY



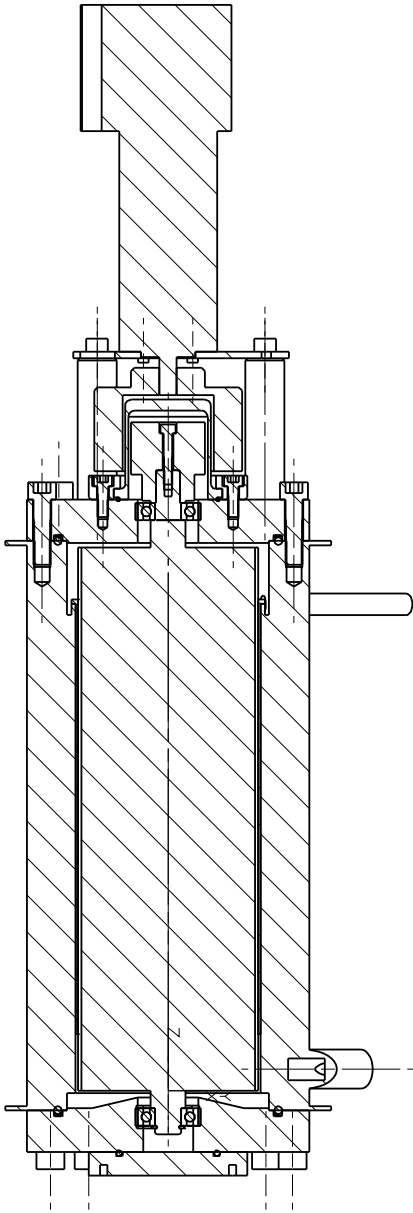
PC NO	PART NAME	QTY
6	LOCK WASHER D_IN = 10	1
5	UPPER-BEARING-ASSEMBLY	1
4	CASING	1
3	AXLE	1
2	FILTER WALL	1
1	LOWER-BEARING-ASSEMBLY	1
	CASING-AXLE-BEARINGS ASSEMBLY	



6	COUPLING COVER	1
5	COUPLING COVER PLATE	1
4	MAGNETIC COUPLING OUTER MAGNET (BURGMANN)	1
3	M3 X 7	4
2	MOTOR SUPPORT PLATE	1
1	MAXON EC45 48 V DC	1
PC NO	PART NAME	QTY



10	M6 x 12 A4/80	3
9	MOTOR_ASSEMBLY	1
8	M5 x 19 A4/80	20
7	BEARING_COVER	1
6	O-RING_42.52x2.62 SIL/TEFLX	1
5	MAGNETIC COUPLING TOP COVER (BURGMANN) 3 PARTS	1
4	M4 x 24 A4	1
3	MAGNETIC COUPLING INNER MAGNET (BURGMANN)	1
2	M8 x 31 A4/80	24
1	CASING-AXLE-BEARING_ASSEMBLY	1
PC NO	PART NAME	QTY



Dankwoord

Geen enkel proefschrift kan zonder dankwoord, en ook dit proefschrift zou niet tot stand zijn gekomen zonder de hulp van een aantal mensen, waarvoor ik ze hier wil bedanken.

Wat voor mij begon als een eenjarig onderzoek naar de toepasbaarheid van gas centrifugatie voor CH_4/CO_2 scheiding evolueerde naar een veel groter project waar mijn promotie en dit proefschrift nu deel van uit maken. De tot nu toe behaalde resultaten in dit project, dus ook dit proefschrift, zouden niet mogelijk zijn geweest zonder de inzet en vastberadenheid van Bert Brouwers en Michael Golombok. Als begeleiders waren ze vrijwel dagelijks betrokken bij mijn vorderingen, maar ook als teamleden werkten we de afgelopen 4 jaar goed en op een prettige manier samen. Bert zijn analytische kennis en sterke intuïtie staan vaak in scherp contrast met Mike zijn experimentele vaardigheden en de vaak onorthodoxe methodes die hij gebruikt om dingen voor elkaar te krijgen. Van beiden heb ik veel geleerd en daarvoor wil ik jullie van harte bedanken.

Het vervaardigen van de fase diagrammen die te zien zijn in hoofdstuk 3 ging niet van een leien dakje, en zou nooit gelukt zijn zonder de hulp van Miranda Mooijer. Bij het ontwerpen van het prototype zijn de resultaten van de stage van Rob van Benthum goed van pas gekomen. Bij dezen wil ik jullie allebei bedanken.

De realisatie van het prototype zou niet mogelijk zijn geweest zonder de vakkundige hulp van Geert-Jan. Vele uren hebben we in de werkplaats doorgebracht; aan het werk aan het prototype, overlegend over de te volgen productie of ontwerpstrategie, en pratend over van alles en nog wat. Geert-Jan, bedankt voor de fijne samenwerking en de gezellige tijd!

Deze promotie was dus niet alleen een leerzame tijd, maar ook een leuke tijd. Dit laatste is vooral te danken aan mijn kamergenoot Carlo, die altijd en voor iedereen klaar staat om te helpen, al dan niet met koffie. Ook Raymond, Niels en Guy zorgden voor veel gezelligheid en waren waarschijnlijk meer op onze kamer te vinden dan op hun eigen. Mijn grote dank gaat naar jullie uit alsook naar alle andere mensen waar ik de afgelopen 4 jaar mee heb samengewerkt!

Ralph

Maastricht, oktober 2006

Curriculum Vitae

Ralph van Wissen was born in Heerlen, The Netherlands, on the 11th October 1978. From 1991 to 1997 he followed secondary education (VWO) at the Jeanne d'Arc College in Maastricht. In 1997 he started to study Mechanical Engineering at Eindhoven University of Technology. During this study he did a traineeship at DSM, where he worked on models of extraction and absorption columns, and the implementation of these models in plant flow sheets models.

Ralph started his graduation project in 2002 in the Process Technology Group of prof.dr.ir. J.J.H. Brouwers at Eindhoven University of Technology. This project involved an experimental investigation of direct steam injection for food production. The work was done in cooperation with Unilever Research and Development and led to publications in *Int. J. Heat Fluid Flow* (**25**(2), 2004, pp 173-179), and *J. Fluid Mech.* (**530**, 2005, pp 353-368). After finishing his graduation project, Ralph graduated Cum Laude in February 2003.

Thereafter, he started to work on his Ph.D. project in the Process Technology Group. Supervisors: prof.dr.ir. J.J.H. Brouwers and prof.dr. M. Golombok. The Ph.D. project was funded by Shell International Exploration and Production. It concerned the development of a new centrifugal separation technology for removing CO₂ and/or H₂S from natural gas. The results of this study as well as the design of a prototype are described in this thesis. Parts of this work are published in: *Chem. Eng. Sci.* (**60**, 2005, pp 4397-4407), *AIChE J.* (**52**(3), 2006, pp 1271-1274), *Oil & Gas J.* (2006, accepted for publication), *AIChE J.* (2006, submitted for publication).